MODELISATION DU PROCEDE DE SOUDAGE PAR POINT

Sommaire

Synopsis

In this chapter, decoupling and coupling procedures are implemented to simulate the RSW process. In the case of using flat face electrode, it is found that it is possible to obtain a final nugget size in good agreement with the experience by the use of the decoupling procedure. However, the coupling procedure is necessary in the case of welding with curved face electrode, and especially for the stackup-sheet configuration modeling. This is to simulate the electrothermal contact size variation manifesting during welding process. The findings presented in this chapter are :

- *Role of an optimum contact size imposed at faying surface with the use of electrothermal-mechanical decoupling model*
- *Post-heat treatment study using pulsed current schedule and its influence on the weld characteristics of high strength steel joining*
- *Influence of electrothermal physical properties in the RSW modeling with the use of coupling procedure. Validation of kinetics weld development is conducted in case of two- as well as three-sheet joining*
- *Importance of electrode hold time for thermal history and weld quality is studied with a removed-electrode model. Both electrothermal and thermomechanical boundary conditions are modified in this case.*

3.1 Introduction :

A continuous effort has been devoted to RSW process modeling since 1960. This is justified by the advantages of the process in the automobile industry, such as the robustness, the rapidity, the flexibility, and relative low cost involving weld quality and fabrication. RSW numerical simulation is conducted and documented in the literature-[DIC90, TSA91, VOG92-2, etc…], for the nugget development, the thermal history, and the residual stress prediction in the weld. The common goals of these researches are not only to evaluate the weld property of single spot weld point, but also to simulate the presence of multi-spots in the global vehicle structure for other virtual dynamic tests,-[FAU03]. This kind of application has already been approached with an example of global distortion study. The 2D local results of a spot welding model (i.e. residual deformations, residual stresses and/or resulting metallurgical state) have to be transferred to 3D or shell elements. This transfer usually includes a simplification to reduce the number of elements and nodes representing the weld. However this full procedure, which allows a coupling between welding parameters and the weld behavior inside the global structure, is not yet frequently applied.

However, this kind of transfer procedure was already applied to model the behavior of normalized testing coupons-[KOP00]. These attempts are to improve the production quality and process performance.

However, the simulation of single point spot is still essential to understand the internal physics of process when parameters and assembly configurations change. The presence of novel steel grades/coatings and that of aluminium sheet in car structure enlarge significantly the existing domains of numerical application and material databases needed.

A general presentation of the resistance spot welding and the experimental study for the nugget development and the influence of welding parameters are presented in chapters 1 and 2. The welding parameters found are useful for the process inputs in this chapter.

An overview of the numerical techniques for RSW process simulation can be underlined from the simplest numerical techniques to the recent advanced computation procedures as the follows :

i) Thermal conduction model using finite difference technique,
ii) Electro-thermal model using finite element analysis technique,
iii) Decoupling between electro-thermal and thermo-mechanical models using finite element analysis technique,
iv) Coupling between electro-thermal and thermo-mechanical models using finite element analysis technique.

Different coupling scales can be implemented for electro-thermal and thermo-mechanical modules. It can be varied from a decoupled electro-thermal model to a coupled micro-time step scale model.

Decoupling procedure can be described by transferring the nodal thermal history, resulting from the electro-thermal module once the electro-thermal computation terminated, to the thermo-mechanical computation to calculate the thermal induced stresses and deformations in the workpiece. Regarding this transfer sequence, one can understand that there is no updated workpiece geometry or the deformation of the workpiece in the electro-thermal model, since the nodal deformation and stress history calculated in the thermo-mechanical module are not transferred back to the electro-thermal module to update electro-thermal contact characteristics. Other advantages of decoupled procedure are the low computation cost and the simplicity of the implemented computation scheme.

The importance of the coupling between electro-thermal/thermo-mechanical modules has been recognized in RSW simulation and this procedure has been widely implemented to capture the contact size variation. Furthermore, the coupling allows the simulation possible for the use of curved electrodes in welding.

It is noted that the metallurgical phase transformation properties can be included in the electro-thermal module. Computed thermal history in the structure are used as the input for phase transformation predictions. In this case, a continuous cooling transformation-(CCT) diagram must be established to describe the phase transformation characteristics of steels.

In this chapter, the mathematic formulation and the boundary conditions imposed to the meshing structure will be detailed. The thermal/mechanical properties of sheet will be briefly presented.

Conclusion of our findings and the simulation results documented in the proceedings of international conference on weld phenomena simulation will be made in the last section.

3.2 General Methodology for Weld Simulation :

A generalized principle and methodology of weld simulation is proposed by Ferrase *et al.*,[FER98-1], to study the thermal characteristics in mash seam process modeling. Different stages to establish a model can be highlighted in Fig. 3.1. A basic knowledge on the process characteristics, especially on the practical parameters and the initial hypotheses is necessary at the beginning. Second, the model construction with a consideration of a complete/sectioned structure associated with boundary conditions. If it is possible, a planar- or an axis-symmetrical structured mesh model is preferred to the extended complete structure in order to minimize time/cost of the computation. The optimization of the number of elements and element types could be an advantage for a frequent used model. A solid background experience of user is required on how thermal/mechanical loads and boundary conditions can be imposed to those axis-symmetric structures. In the third step, a selection of the commercial code adapted to the application is needed for simulate the problem. This step concerns mainly the existence of analysis modules in the code and the user interface facility.

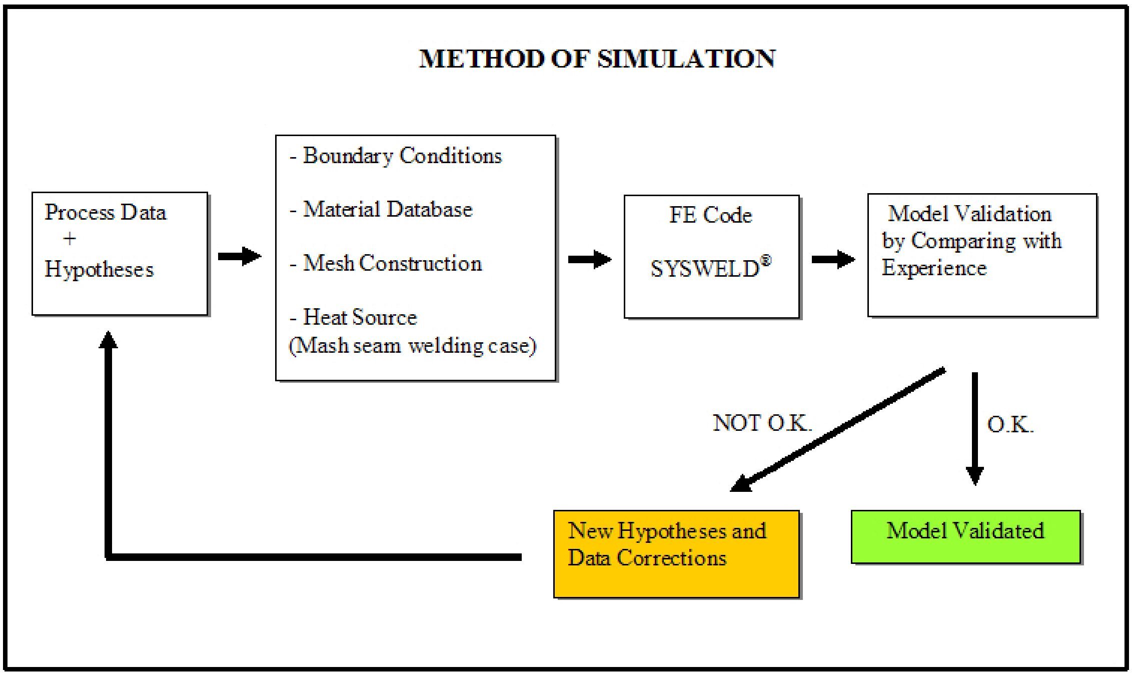

Fig. 3.1: *Generalized methodology for mathematical modeling of resistance welding-[FER98-1].*

In this study, Sysweld™ code is chosen for the simulation purpose due to its features concerning weld simulation. Prior to the exploitation of a model, the validated results are essential for the application assurance. For RSW process, the validation scopes can go beyond the weld size and geometry validation. Other quantitative validation aspects, such as the thermal history validation, signal of electrode displacement, or voltage drop across the electrodes can be also conducted-[SRI03-2]. The validation process leads to the verification of initial hypotheses and the adaptation of the input parameters.

The final stage is to correct/accept the model and/or hypotheses, (§Fig. 3.1).

3.3 Physical Coupling and Governing Equations :

Physical phenomena involved in welding are complex. The physical interaction phenomena are the fluid flow in the molten pool of the weld, heat transfer, phase transformations induced by thermal history, stresses and strains in the weld. For the RSW, the general physics, schematized in Fig. 3.2, demonstrates the brief relationship among different aspects such as heat transfer, mechanics, metallurgy, and electro-magnetokinetics.

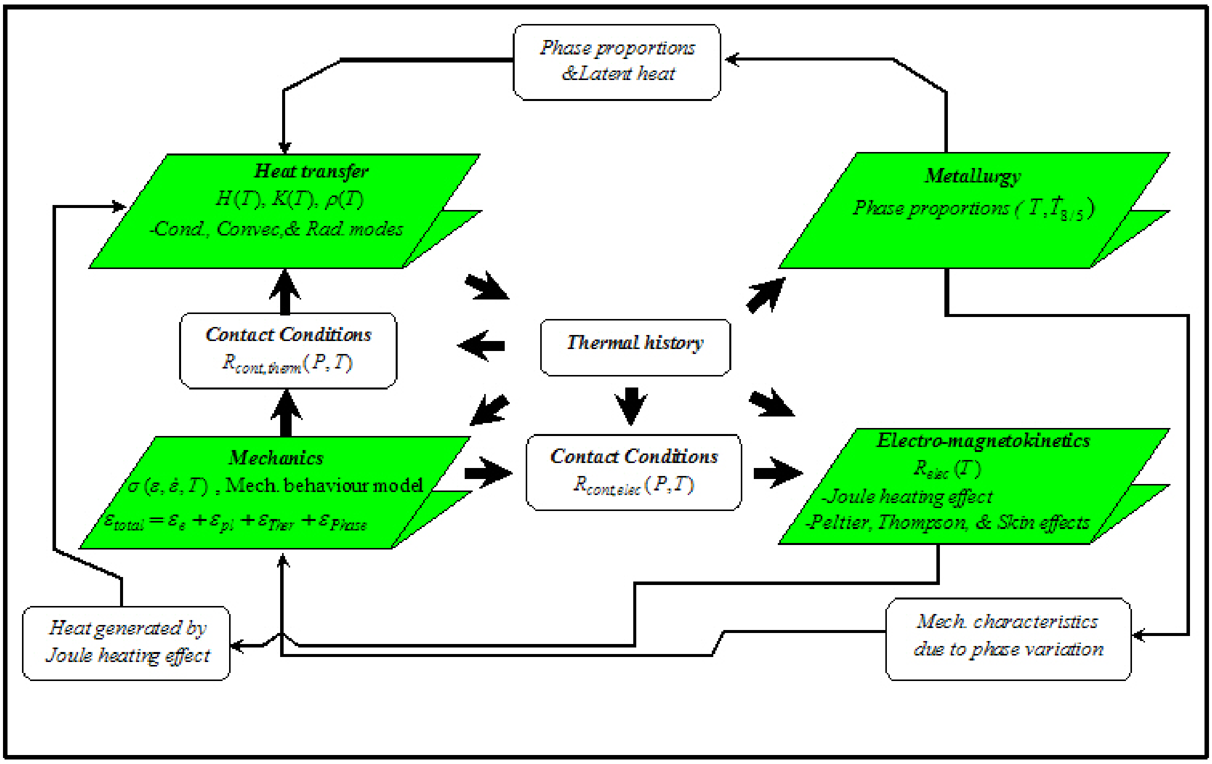

Fig. 3.2: *Relationship among different aspects concerning the RSW process simulation-[DUP04].*

Basically for the weld simulation, thermal history can be considered as a linking input for the other phenomena and that of the material properties in order to take into account for temperature dependence, (§Fig.3.2). According to the documentation [VOG92, THI92, LE MUR02], the temperature has an influence not only on characteristics of thermal contact, but also on that of electrical contact.

For the coupling computational procedure, several different levels of coupling procedure can be highlighted, regarding time-step for the assembly updating :

❖ Geometry updating each macro time-step (§Fig. 3.3a); the macro time steps are defined equivalently in both electro-thermal and thermo-mechanical analyses. However, micro-time step scale for both modules may be different. In our study, the macro time step coupling programmed by user are defined for each 1/10 of welding cycle or 0,02 seconds. The coupling closed loop procedure is to perform a sequenced coupled computation or the case of modified boundary conditions, e.g. the influence of time-length of electrode maintaining stage on the thermal history experiencing in the weld.

❖ Geometry updating for each micro-time step as depicted in Fig. 3.3b; the time-step have to be equal in both macro and micro scale for both electro-thermal and thermo-mechanical analyses.

❖ Fully coupling for each micro time-step between two analyses as shown in Fig. 3.3c; In this case convergence must be reached simultaneously for both analyses at each micro time step.

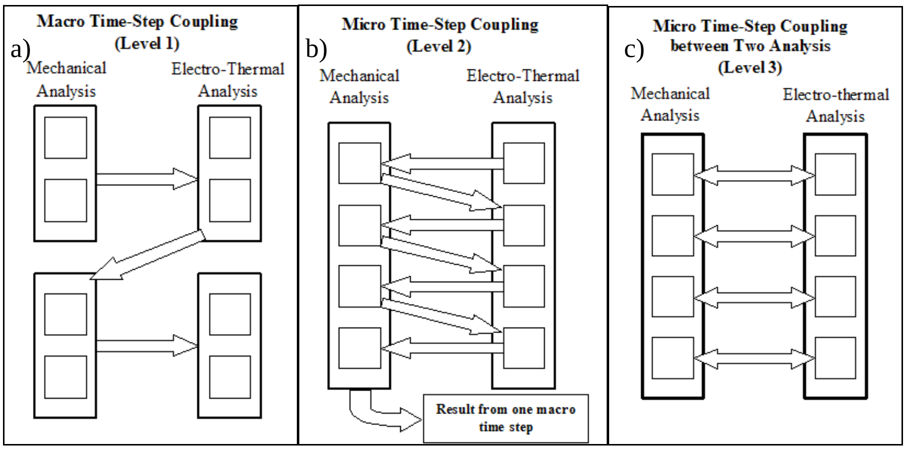

Fig. 3.3: *Illustration of the coupling procedure used in the spot welding simulation-[DUP04].*

3.4 Governing Equations :

Electrical Phenomena Formulation :

According to the electrical formulation, the electrical phenomenon in RSW is individual treated to the *steady state electro-kinetic* problem. Ohm's law in vector form, which is described a steady flow for the current flux can be stated as follows :

$$\vec{J} = -\sigma.\vec{E} \ \text{,where} \ \vec{E} = -\overrightarrow{gradV} \qquad [3.1]$$

where ' $\vec{J}$ ' and ' $\vec{E}$ ' are current flux flowing across a section area (Amp/m^2) and electrical field density (V/m), respectively. ' σ ' is the electric conductivity of the conductor (1/(Ohm.m)). ' V ' is scalar electrical potential (V).

To calculate current, ' $\vec{I}$ ' , as the result of current density flux, ' $\vec{J}$ ', at any point of a cross section, ' s ' :

$$\vec{I} = \iint_s \vec{J}.ds \qquad [3.2]$$

These conditions are associated with the conservation of the current flux, ' $\vec{J}$ ', flowing along a conductor :

$$div\vec{J} = 0 \ \text{ or according to (3.1);} \quad div(\sigma\overrightarrow{gradV}) = 0 \qquad [3.3]$$

Coupled Electro-Thermal Formulation :

RSW is a *non-linear* and *unsteady state* problem with full coupling between electrical and thermal modules. The generalized formulation of governing equation with the internal heat generation can be established as follows :

$$\rho\frac{\partial H}{\partial t} - div\,(\lambda.\overrightarrow{gradT}\,) - \overrightarrow{gradV}\,.(\sigma.\overrightarrow{gradV}\,) - Q = 0 \qquad [3.4]$$

In this expression, ' $\rho(T)$ ' is the mass density, ' $H(T)$ ' is the enthalpy, ' $\lambda(T)$ ' is thermal conductivity, and ' $\sigma(T)$ ' is the electrical conductivity. Temperature-dependent characteristics of sheet and that of electrode can be included in the model. The full coupling between the electrical and thermal phenomena can be governed by term ' $\overrightarrow{gradV}\,.(\sigma.\overrightarrow{gradV}\,)$ ' in the heat equation, which includes the Joule effect as a heat source.

For RSW process, there are also other thermo-electrical involved effects, for example Thomson or Peltier effect-[VIC01], which can be considered as internal heat sources. To account these physical phenomena, Thomson or Peltier coefficient is necessary to be included in the model. However using code Sysweld^{TM}, other thermo-electric effects cannot be integrated. It is assumed that internal heat term ‘ Q ’ may be less significant and therefore neglected in the analysis, for instance. Details of finite element formulation for electro-thermal analysis is described and documented in the dissertation,-[THI92].

Generally, there are two possible methods for thermal computation; the specific heat, (‘ C_p ’), and the enthalpy model, (‘ H ’). However to effectively take into account the latent heat of phase transformations (especially, latent heat of transformation ‘ $\gamma \to \alpha$ ’ and that of the fusion state from solid to liquid phase), the enthalpy model is more convenient than ‘ C_p ’ model. In addition, the integration of the metallurgy phase database associating with a phase transformation model to thermal computation, it is only possible with the use of enthalpy model-[FOR04], due to the relationship between thermal and metallurgical aspects. These relationships are :

- metallurgical phase transformations depend directly on the thermal history experiencing in the weld,
- thermal properties are phase-independent characteristics,
- and metallurgical transformations are accompanied by the latent heat effects, which modify the temperature distribution.

Essentially, the enthalpy model is employed in our analysis basing on its unique model features mentioned above.

Mechanical Formulation :

The elasto-plastic behaviour is non-linear with temperature and thermal induced stresses and deformations. Three governing equations, namely, the compatibility condition, the constitutive relation, and the equilibrium equation in cylindrical co-ordinate can be established as follows-[MUR97] :

Compatibility conditions :

$$\varepsilon_r = \frac{\partial u_r}{\partial r} \; ; \; \varepsilon_\theta = \frac{\partial u_\theta}{\partial \theta} \; ; \; \varepsilon_z = \frac{\partial u_z}{\partial z} \qquad [3.5]$$

and

$$\gamma_{rz} = \frac{\partial u_r}{\partial z} + \frac{\partial u_z}{\partial r} \qquad [3.6]$$

where ‘ ε_r ’, ‘ ε_θ ’, ‘ ε_z ’, and ‘ γ_{rz} ’ are strain components. ‘ u_r ’, ‘ u_θ ’ and ‘ u_z ’ are the displacements in radial, tangential and axial direction, respectively.

Constitutive relations :

$$\{\Delta\sigma\} = [\mathbf{D}]\{\Delta\varepsilon\} + [\mathbf{C}]\Delta T \qquad [3.7]$$

with $\{\Delta\sigma\} = \{\Delta\sigma_r, \Delta\sigma_\theta, \Delta\sigma_z, \Delta\tau_{rz}\}$ [3.7.1]

$\{\Delta\varepsilon\} = \{\Delta\varepsilon_r, \Delta\varepsilon_\theta, \Delta\varepsilon_z, \Delta\varepsilon_{rz}\}$ [3.7.2]

where ‘ $[\mathbf{D}]$ ’ and ‘ $[\mathbf{C}]$ ’ are defined for elastic and thermoelastic/plastic state, respectively. The stress increment described in (3.7.1) is given in terms of strain and temperature increment.

Equilibrium equation (Virtual work theorem)

$$\delta U = \iint \left\{ \begin{array}{l} (\sigma_r + \Delta\sigma_r)\delta\varepsilon_r + (\sigma_\theta + \Delta\sigma_\theta)\delta\varepsilon_\theta \\ + (\sigma_z + \Delta\sigma_z)\delta\varepsilon_z + (\tau_{rz} + \Delta\tau_{rz})\delta\gamma_{rz} \end{array} \right\} 2\pi r dr dz$$

$$= \int \{ n_r (t_r + \Delta t_r)\delta u_r + n_z (t_z + \Delta t_z)\delta u_z \} 2\pi r ds$$

$$\delta U = \delta V \qquad [3.8]$$

where ‘ δU ’ is the internal virtual work done by stress, ‘ $\{\sigma+\Delta\sigma\}$ ’ through the virtual strain ‘ $\{\delta\varepsilon\}$ ’, ‘ δV ’ is the external virtual work done by traction ‘ $\{t+\Delta t\}$ ’ through the virtual displacement. ‘ $\{\sigma_r,\sigma_\theta,\sigma_z,\gamma_{rz}\}$ ’ are the stresses at previous time step and ‘ $\{\Delta\sigma_r,...\}$ ’ are the stress increment at the next time step. ‘ $\{\delta\varepsilon_r,...\}$ ’ are the virtual strain. ‘ $\{n_r,...\}$ ’ are outward unit normal vectors of surface. ‘ $\{\delta u_r,...\}$ ’ are the virtual displacements.

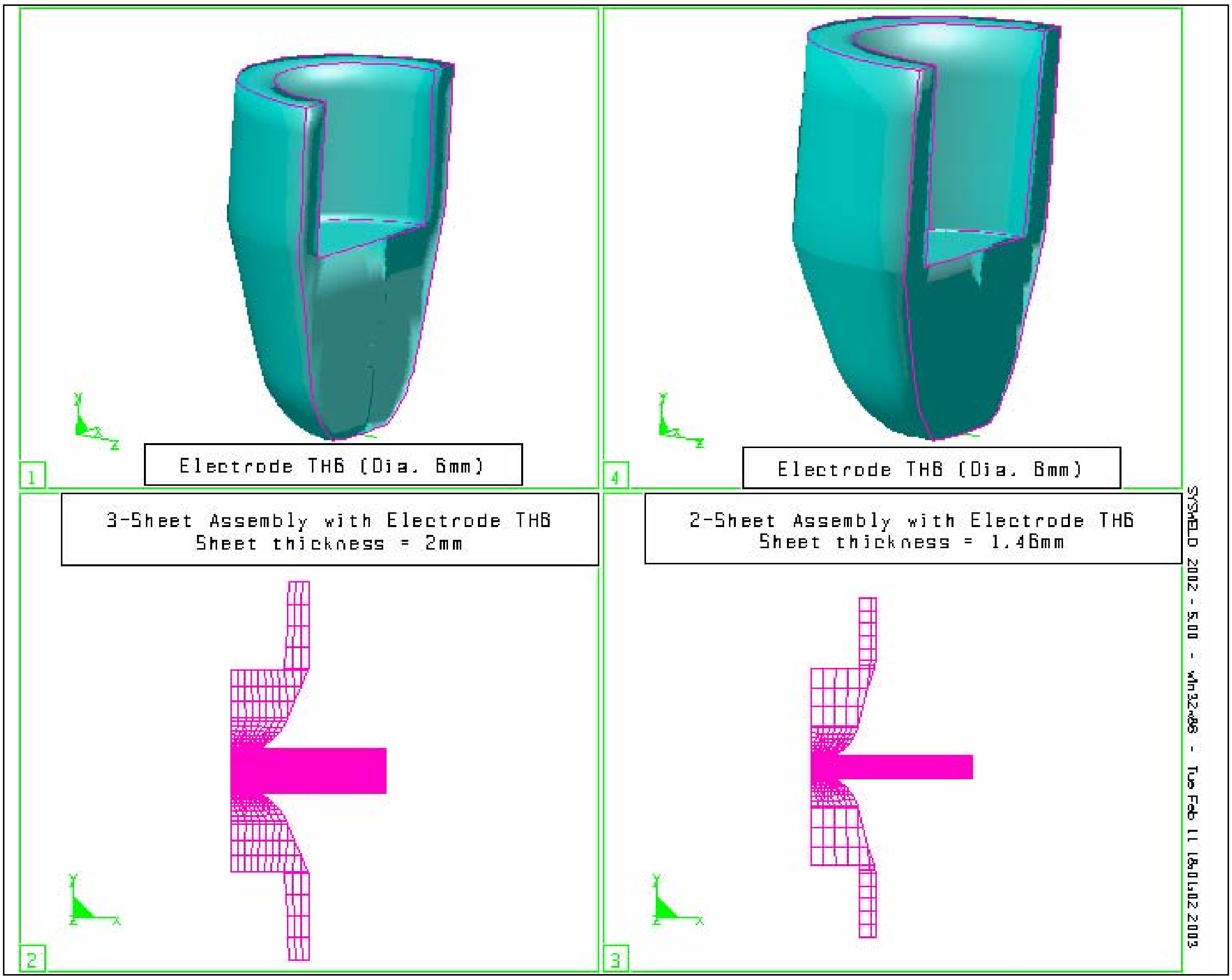

Fig 3.4: *Illustration of the different electrode type and the meshed structure used in simulation; a) Truncated cone electrode with curved face profile of 6-mm dia., namely TH6, b) Truncated cone electrode with curved face profile of 8-mm dia., namely TH8 c) Mesh construction for three-sheet assembly using electrodes TH6, and d) Mesh construction for two-sheet assembly using electrodes TH8.*

3.5 Geometry and Mesh Construction :

The structure of both electrode and workpiece is constructed in the ‘ $x-y$ ’ plane, in cartesian coordinate system as shown in Fig. 3.4. It is noted that the calculation is performed in the ‘ $r-\theta-z$ ’ coordinate system by a definition defined in the main analysis program.

3.6 Boundary Conditions :

Concerning an *electro-thermal axisymmetric model*, there are two types of the boundary conditions imposed to the structure :

- ❖ Electrical boundary condition,
- ❖Thermal boundary condition.

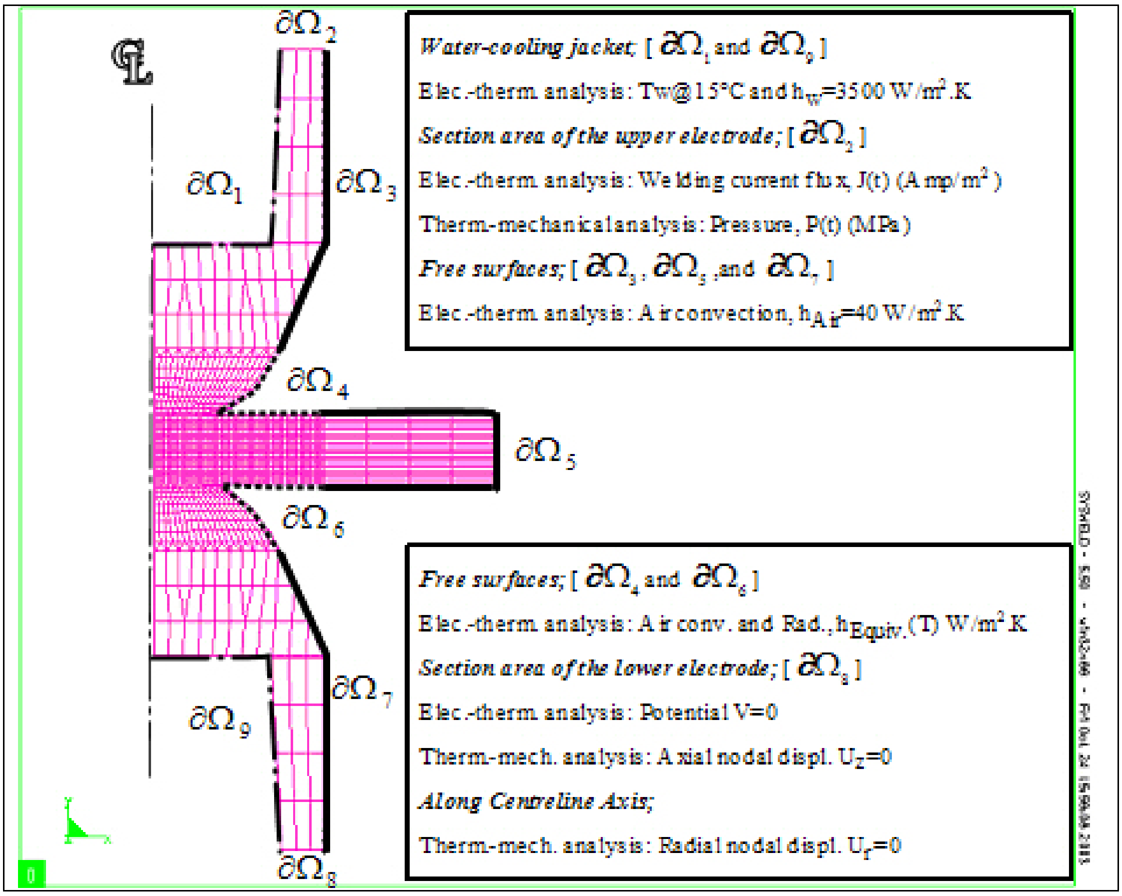

***Fig. 3.5:** Imposed electro-thermal and mechanical boundary conditions to the structure*

Electrical Boundary Condition :

There are two techniques for the current applied in the structure :

-Potential imposed boundary condition: (Neumann condition). To generate the flow of current, the potentials ‘V_1’ and ‘V_2’ are imposed at the upper and the lower sections of the electrodes and the condition on the free boundaries is : $\frac{\partial V}{\partial \hat{n}} = 0$

-Combined boundary conditions : Welding current can be directly conversed to the flux, (i.e., applied flux in the 2-D axis-symmetric model :

$$\vec{J}(t) = -\frac{I}{S}.\hat{j}.f(t)$$

where ‘ $f(t)$ ’ is the current wave form described as a function of time. The *flux* is applied at the upper section of the electrode and *zero potential* is imposed at the lower section of the electrode.

The applied flux boundary condition has been employed in our model, because it is similar to the practical welding operation.

Thermal Boundary Conditions :

Generally, there are three kinds of boundary condition in the thermal analysis :

❖*Potential imposed boundary condition* (Dirichet condition) to specify the temperature on the surface : $T = T_s$.

❖*Flux imposed boundary condition* (Neumann condition) to impose the heat flux on the surface :

$-k\dfrac{\partial T}{\partial \hat{n}} = \Phi_0$ for adiabatic surface or for the line of symmetry as in our case, $-k\left.\dfrac{\partial T}{\partial \hat{n}}\right|_{\Gamma 0} = 0$, where ‘ $\hat{n}$ ’ denotes the normal direction of the boundary.

❖*Heat transfer* (Fourier condition) occurring at the structure surface :

$-k\dfrac{\partial T}{\partial \hat{n}} = h(T_\infty - T)$, where $h(T)$ is heat transfer coefficient as a function of temperature :

❖ the convection heat transfer coefficient : $h_c(T)$,

❖ the radiation heat transfer coefficient : $h_r(T) = \varepsilon\sigma(T_\infty + T)(T_\infty^2 + T^2)$,

❖ or combined heat transfer coefficient : $h(T) = h_c(T) + h_r(T)$.

where ‘ ε ’ is the emissivity of surface, and $\sigma = 5{,}67 \times 10^{-8} W/m^2/K^4$ is the Stefan-Boltzmann constant in the case of the radiation in an infinite medium at temperature ‘ T_∞ ’.
The electrical and thermal boundary conditions, (§Fig. 3.5), can be summarized as follows :

1) ‘ $\partial\Omega_1$ ’ and ‘ $\partial\Omega_9$ ’ : Water-cooling sink surface
2) ‘ $\partial\Omega_2$ ’ : Section of the upper electrode subject to current flux
3) ‘ $\partial\Omega_3$ ’, ‘ $\partial\Omega_5$ ’,and ‘ $\partial\Omega_7$ ’ : Free surfaces of air convection
4) ‘ $\partial\Omega_4$ ’,and ‘ $\partial\Omega_6$ ’ : Combination of radiation and air convection using an equivalent heat transfer coefficient imposed to free surface
5) ‘ $\partial\Omega_8$ ’ : Section area of the lower electrode subject to the zero potential

Before the beginning of welding, the electrical initial conditions are set equal to zero and the temperature of the entire structure is specified to 20°C. The cooling water temperature is 15°C, (constant through the process simulation).
Mechanical boundaries corresponding to the practical welding operation imposed to the structure are :

1) ‘ $\partial\Omega_2$ ’ : Pressure modeled from the welding force signal divided by the section area of the upper electrode is applied at the section of the upper electrode
2) ‘ $\partial\Omega_8$ ’ : Vertical nodal displacement of the lower section of the electrode is constrained
3) ‘ $\partial\Omega$ - $\sum\partial\Omega_i$ ’ : Nodal radial displacement of line of symmetry is constrained
4) *Contact condition* : Slide-line contact without friction is defined for the electrode-to-sheet and sheet-to-sheet interfaces

According to the electrical boundary conditions, the welding current is applied at the top of the upper electrode and zero potential is specified at the bottom surface of the lower electrode. Consequently, the current flux flows from the section of the upper electrode, passes through the workpiece, and terminates at the bottom annular end of the lower electrode. Both current and force are obtained from the welding operation as illustrated in Fig. 3.6.

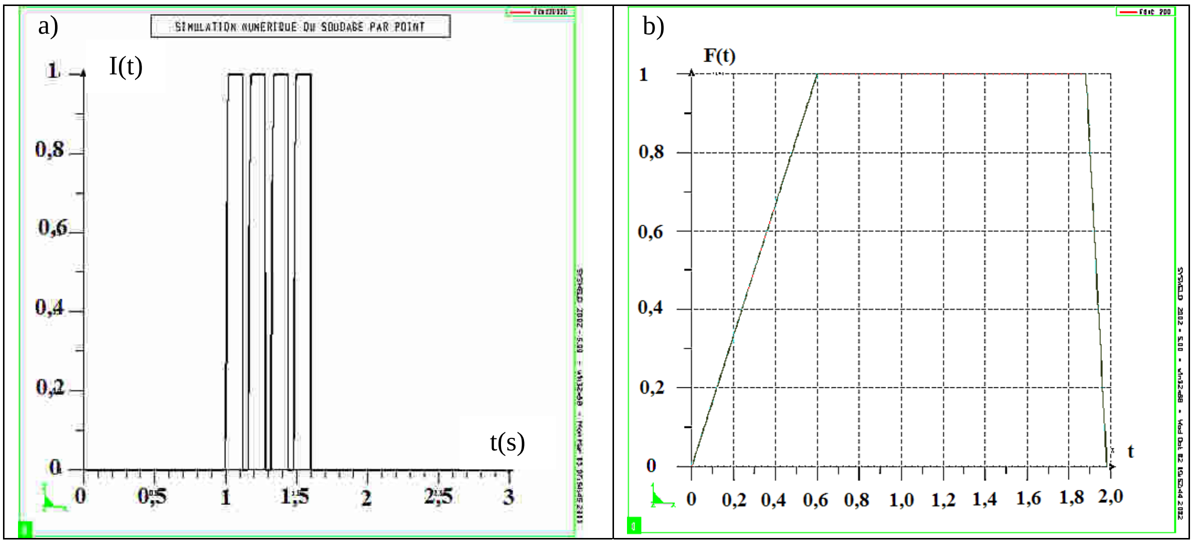

***Fig. 3.6:** Welding signals as a unit time-dependent function used in electro-thermal and thermo-mechanical analyses, a) Modeled pulsed-current waveform, and b) Modeled welding force as a function of time including the squeezing, welding, and electrode holding stages.*

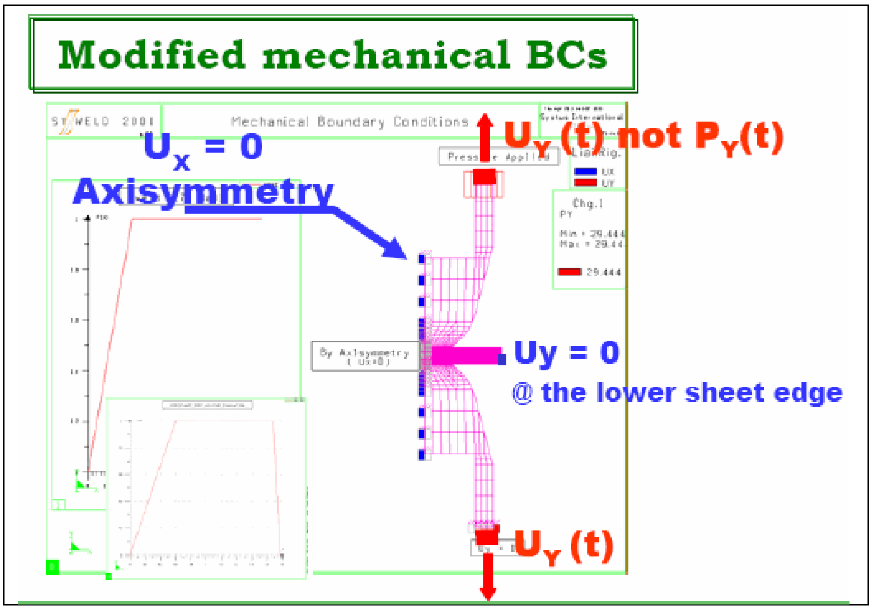

***Fig. 3.7**: Modified mechanical boundary conditions to remove both electrodes from the assembly to study the influence of electrode hold time.*

<u>Modified Boundary Conditions for Electrode Removing Case :</u>

To study the influence of the electrode holding time on the thermal history of assembly after the end of hold stage, the boundary conditions in both thermal and mechanical analysis are modified. The second coupling analysis program is implemented for this simulation purpose. The thermal history and stresses computed at the end of the maintaining, becomes therefore the *initial conditions* for the next computation step with removed electrodes. Modified boundary conditions are as follows :

<u>Modified Thermal Boundary Conditions :</u>

1) ‘ $\partial\Omega_1$ ’, and ‘ $\partial\Omega_9$ ’ : Water-cooling sink surfaces
2) ‘ $\partial\Omega_3$ ’, ‘ $\partial\Omega_4$ ’,’ $\partial\Omega_5$ ’,’ $\partial\Omega_6$ ’, and ‘ $\partial\Omega_7$ ’ : Free surfaces of air convection
3) ‘ $\partial\Omega_3$ ’, and ‘ $\partial\Omega_8$ ’ : No electrical loads imposed to the upper and lower sections of electrodes

Modified Mechanical Boundary Conditions :

1) ‘ $\partial\Omega_2$ ’ : Section of the upper electrode subject to vertical nodal displacement

2) ‘ $\partial\Omega_8$ ’ : Section of the lower electrode subject to vertical nodal displacement, i.e. nodal displacement of 3-mm is assumed to remove both electrodes. The duration of the electrode lifting can be obtained from the electrode displacement signal. Note that the pressure or force cannot be applied to remove the electrodes. This leads to an infinite distance for the electrode displacement, and thus non-convergent.

3) *Fixing the assembly* : to maintain the assembly after electrode removed, a node or a group of nodes is constrained for their vertical displacements. We have performed many tests to verify the most appropriate boundary condition.

To maintain the assembly after removing electrode, the vertical and radial nodal displacements of weld centre is selected and constrained. However, after the verification of the residual stresses, a stress concentration is found at the centre of the weld because of a node fixed at the centre.

To avoid the stress concentration associated with constrained nodes, a group of nodes along the edge of the lower sheet is selected and their vertical displacements are fixed. As a result, it is found that there is no effect of the constrained conditions on the residual stress distribution in the assembly. Therefore, these constrained conditions are chosen to study the influence of removing electrode on the thermal and mechanical characteristics in the workpiece.

The idea concerning where to be fixed in the assembly after the electrode removing is to minimize or to eliminate the residual stresses produced by the constrained boundary conditions. The residual stress comparison between the case of non-removing and that of removing electrode conditions is essential in order to verify the influence of the constrain condition on the stress results.

4) *Contact condition* : After removing electrodes, the sticking contact condition is defined for fusion zone or nugget where temperature is greater than fusion temperature of sheet.

3.7 Electrothermal Contact Mathematical Formulation :

As mentioned in the previous sections, the most important database in RSW welding process is the contact properties. In this paragraph, the electro-thermal contact model of Sysweld^{TM} is presented :

Definition : *Let ‘ ε ’ be the threshold value of a separating distance or a gap between two surfaces. When interface separating distance, ‘h’, is less than the defined value of ‘ ε ’ or ($h \le \varepsilon$), the interface is* <u>*perfect contact*</u>*. Contrary to this condition, the interface characteristics are assumed to be* <u>*non-perfect contact*</u> *condition.*

Actually, the threshold value, ‘*h*’, can be defined in the program by user. The contact contact, the heat transfer coefficient and the electrical contact resistance are directly defined in user’s FORTRAN functions. In this study, the electrical and thermal contact resistances are a function of temperature.

For the **non-perfect condition**, the heat transfer coefficients and the electrical contact resistance are defined as follows;

Let us examine any subdivided *macro contact elements* of an interface, (§Fig. 3.8), namely surfaces ‘ S_1 ’ and ‘ S_2 ’, respectively.

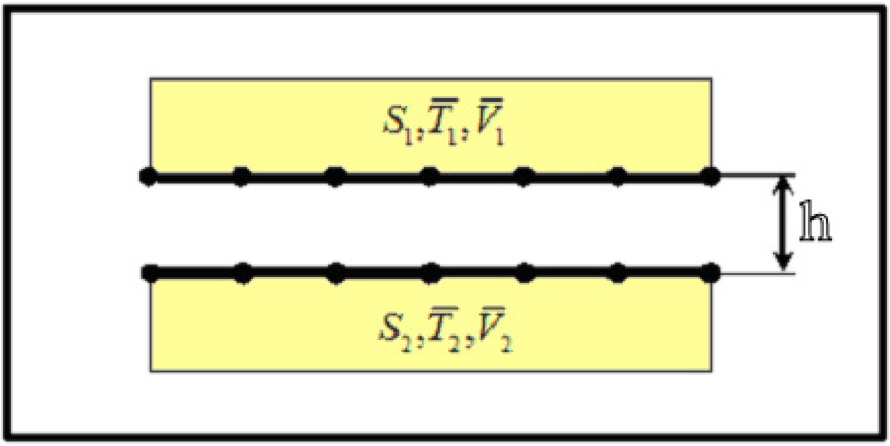

Fig. 3.8: *Equivalent size of a group of slide-line contact elements with a separated distance between two surfaces ' h '.*

' A^S ', ' $\overline{T}^S$ ', and ' V^S ' are the area, the mean temperature, and the mean electrical potential of the surface ' S '. Heat transfer occurring at the interface is the combination of heat convection and radiation modes which can be simplified to an equivalent resistance model. Heat transfer coefficient model, (' H_{gap} '), described in [SYS01, ROB01] is :

$$H_{gap} = \frac{\lambda_{air}}{h} + \frac{\varepsilon^1 \varepsilon^2}{\varepsilon^1 + \varepsilon^2 - \varepsilon^1 \varepsilon^2} \sigma(\overline{T}_1^{\,2} + \overline{T}_2^{\,2})(\overline{T}_1 + \overline{T}_2) \qquad [3.9]$$

where ' λ_{air} ', ' ε^S ', ' σ ' and ' $\overline{T}_m = \frac{\overline{T}_1 + \overline{T}_2}{2}$ ' are the thermal conductivity of the air, the emissivity of the surface ' S ', the Stefan-Boltzman constant and the mean temperature at interface, respectively. Based on the small relative displacement of contact elements, the gap distance, (' h ') is defined for the conduction heat transfer of any coupled contact elements. During the coupling computation, if ' h ' is greater than a threshold value, (' ε '), or *non-perfect contact*, the heat transfer is assumed to be the radiation and convection modes as indicated in [3.9].

Similarly to equivalent heat transfer coefficient formulation, the expression of the non-perfect electrical contact resistance, ' R_{gap} ', is :

$$\frac{1}{R_{gap}} = \frac{1}{\rho_{air}.h} + \frac{1}{r_{contact}} \qquad [3.10]$$

Where ' ρ_{air} ' is the air-gap resistance and ' $r_{contact}$ ' is the additional electrical contact resistance.

To prevent the current flowing across the *non-perfect* elements, a high resistance value of ' 10^6 ' Ohms is assumed for ' $r_{contact}$ '.

Electro-Thermal Contact Formulation:

In this study, the linked-nodes sliding line contact element approach is considered as shown in Fig. 3.8. This is the case of small relative displacement between two contact elements. Number of interface elements has to be the same.

The energy or the amount of heat received by the surface ' S ' can be decomposed into the power density due to heat flux density exchanged, namely ' φ^S ', and heat flux due to the Joule heating effect dissipation, namely ' p^S ', received by surface ' S '. The power density is :

$$Q^S = \varphi^S + p^S \qquad [3.11]$$

The conservation of heat energy and electrical current leads to :

$$S_1\varphi^1 + S_2\varphi^2 = 0 \quad \text{[3.12.1], and } S_1 J^1 + S_2 J^2 = 0 \qquad [3.12.2]$$

The total power density dissipated by the Joule heating effect, namely ‘ P ’, at the interface is :

$$S_1 p^1 + S_2 p^2 = P \qquad [3.13]$$

Let us introduce the mean heat flux (‘ $\overline{\varphi}$ ’) and electrical current (‘ $\overline{J}$ ’) densities exchange between two surfaces :

$$\overline{\varphi} = \frac{S_1\varphi^1 + S_2\varphi^2}{S_1 + S_2} = K(\overline{T}_2 - \overline{T}_1) \qquad [3.14]$$

$$\overline{J} = \frac{S_1 J^1 + S_2 J^2}{S_1 + S_2} = \frac{1}{R}(\overline{V}_2 - \overline{V}_1) \qquad [3.15]$$

Total power dissipated at the interface can be written :

$$P = \frac{S_1 + S_2}{2R}(\overline{V}_2 - \overline{V}_1)^2 \qquad [3.16]$$

A partial fraction of the electrical power, ‘P’, received by surface ‘ S ’ is :

$$p^S = \frac{f^S}{S} P \quad \text{and} \quad f^{S1} + f^{S2} = 1.0 \qquad [3.17]$$

where ‘ $f^{S1} = \dfrac{b_{S1}}{b_{S1} + b_{S2}}$ ’ and similarly for ‘ $f^{S2} = \dfrac{b_{S2}}{b_{S1} + b_{S2}}$ ’. ‘ b_S ’ is represented the effusivity of the body with the surface ‘ S ’ and it is defined by ‘ $b = \sqrt{\lambda\rho Cp}$ ’. ‘ λ ’ is the thermal conductivity, ‘ ρ ’ is the density and ‘ Cp ’ is the specific heat of that material. Developing equations [3.11], [3.12], [3.14], [3.16] and [3.17], we obtain :

$$Q^{S1} = \frac{1}{2}\left[1 + \frac{S_2}{S_1}\right]\left[K(\overline{T}_2 - \overline{T}_1) + \frac{f^{S1}}{R}(\overline{V}_2 - \overline{V}_1)^2\right] \qquad [3.18]$$

$$Q^{S2} = \frac{1}{2}\left[1 + \frac{S_1}{S_2}\right]\left[K(\overline{T}_1 - \overline{T}_2) + \frac{f^{S2}}{R}(\overline{V}_2 - \overline{V}_1)^2\right] \qquad [3.19]$$

Similar manner for the electrical current density, equations [3.12.2] and [3.15] provides :

$$J^{S2} = \frac{1}{2R}\left[1 + \frac{S_2}{S_1}\right]\left[\overline{V}_2 - \overline{V}_1\right] \qquad [3.20]$$

$$J^{S2} = \frac{1}{2R}\left[1 + \frac{S_1}{S_2}\right]\left[\overline{V}_1 - \overline{V}_2\right] \qquad [3.21]$$

The finite element formulation for the mean temperature and electrical potential of surface ‘ S ’, having ‘ n^S ’ nodes and ‘ n_k^S ’ being the shape function of the node ‘ k ’ of surface ‘ S ’ are :

$$\overline{T}^S = \frac{1}{S}\sum_{k=1}^{n^S}\int_S N_k^S T_k^S \, ds \qquad [3.22]$$

$$\overline{V}^S = \frac{1}{S}\sum_{k=1}^{n^S}\int_S N_k^S V_k^S \, ds \qquad [3.23]$$

Where ' T_k^S ' and ' V_k^S ' are the temperature and electrical potential of node ' k ', respectively.
The power and electrical current received by node ' k ' of surface ' S ' to be assembled with the residual vector of the electrokinetic and thermal stiffness matrix are :

$$q_k^s = \int_S N_k^S Q^S ds \qquad [3.24]$$

$$j_k^s = \int_S N_k^S J^S ds \qquad [3.25]$$

Stiffness matrix associating with a macro-contact element can be presented by :

$$[K] = \begin{bmatrix} [K_{TT}] & [K_{TV}] \\ [K_{VT}] & [K_{VV}] \end{bmatrix} \qquad [3.26]$$

For each sub-matrix, we have four terms to compute :

$$[K_{TT}] = \begin{bmatrix} \left[-\frac{\partial q_i^{S1}}{\partial T_j}\right] & \left[-\frac{\partial q_i^{S1}}{\partial T_k}\right] \\ \left[-\frac{\partial q_k^{S2}}{\partial T_i}\right] & \left[-\frac{\partial q_k^{S2}}{\partial T_l}\right] \end{bmatrix} [3.27];\ [K_{TV}] = \begin{bmatrix} \left[-\frac{\partial q_i^{S1}}{\partial V_j}\right] & \left[-\frac{\partial q_i^{S1}}{\partial V_k}\right] \\ \left[-\frac{\partial q_k^{S2}}{\partial V_i}\right] & \left[-\frac{\partial q_k^{S2}}{\partial VT_l}\right] \end{bmatrix} \qquad [3.28]$$

$$[K_{TV}] = \begin{bmatrix} \left[-\frac{\partial j_i^{S1}}{\partial T_j}\right] & \left[-\frac{\partial j_i^{S1}}{\partial T_k}\right] \\ \left[-\frac{\partial j_k^{S2}}{\partial T_i}\right] & \left[-\frac{\partial j_k^{S2}}{\partial T_l}\right] \end{bmatrix} [3.29];\ [K_{VV}] = \begin{bmatrix} \left[-\frac{\partial j_i^{S1}}{\partial V_j}\right] & \left[-\frac{\partial j_i^{S1}}{\partial V_k}\right] \\ \left[-\frac{\partial j_k^{S2}}{\partial V_i}\right] & \left[-\frac{\partial j_k^{S2}}{\partial V_l}\right] \end{bmatrix} \qquad [3.30]$$

where i and j represent the nodes of the contact element of surface, ' S_1 '. 'k' and 'l' represent the nodes of the contact element of surface ' S_2 '.

Electrical-Thermal Contact Verification :

To verify the electrical-thermal contact, a half axisymetric model of two discs is constructed. The upper and the lower discs are separated by the three different gap distances of 5.0, 1.0, and 0.1 mm., (Gaps locating from right to left as illustrated in Fig. 3.9), respectively.

The imposed boundary conditions are similar to the RSW simulation. To produce a current flow, the current flux is imposed at the section of the upper disc and the zero potential is defined to the bottom section of lower disc. Electro-thermal contact resistance properties are taken from our RSW model.

This model is constructed in order to verify whether current flux flowing across the interface or not respecting to a permissible threshold value. For example, the current flux can transverse all three interface, if the permissible distance defined in the program is greater than 5.1-mm. The heating generated by the contact resistance can be seen at three interfaces.

This contact formulation, (§eqs. 3.9 and 3.10), can be described for the non-perfect contact condition when two deformable solids in contact, while passing current and the heat transfer at interface.

Results and Intermediate Discussion :

The assumed interface condition allows us to examine not only the flow of the current, but also the heat generation at the interface corresponding to several contact conditions. In the first case of the threshold value of 5.1-mm., the current flux can transverse three gaps (§Fig. 3.10a), and consequently the heat generation at the interface as depicted in Fig. 3.10b.

In the second case, the threshold value is 1.5-mm, therefore the flux can transverse across only two interfaces with the gap distance of 1.0, and 0.1-mm. The heat generation can be observed at those interfaces.

In the last contact condition with threshold value of 0.15-mm, the heat zone can be found at the interface locating at the centre of disc because the current can pass only this interface.

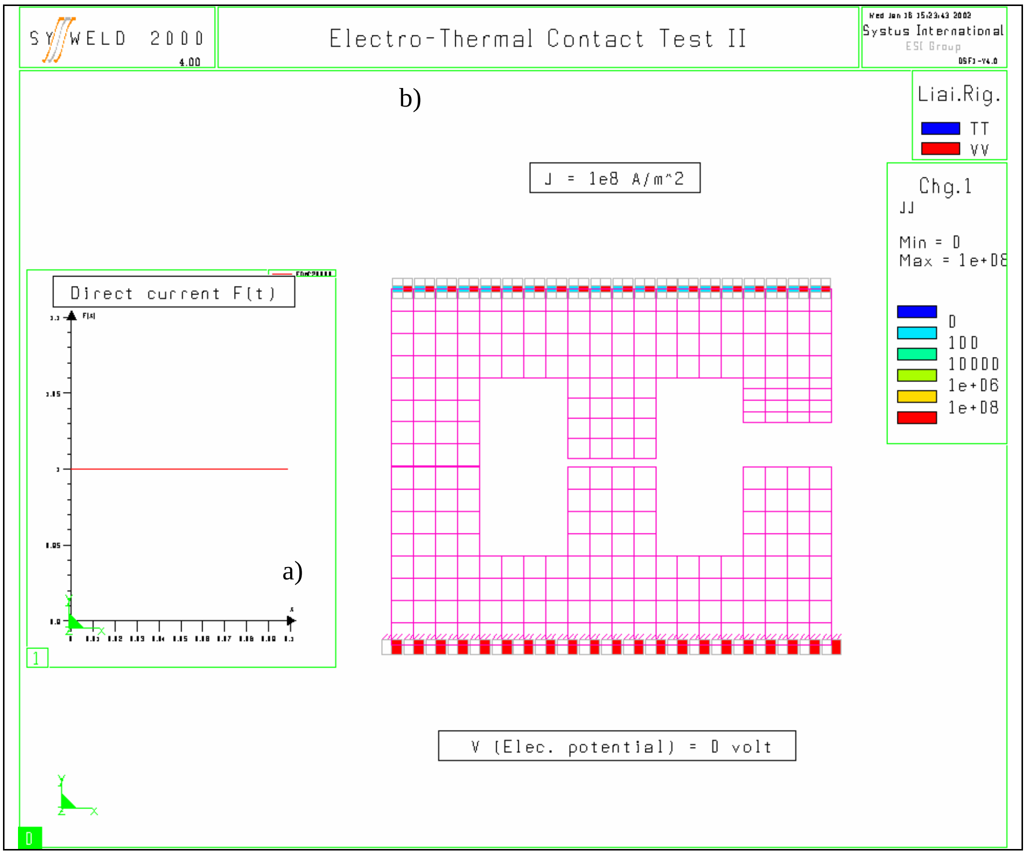

Fig. 3.9: *Modeled electrical flux load and meshed structure of two discs used to verify the heat generation at the interface with the consideration of several gap distances (from right to left of the structure); ε = 5.0-mm, 1.0-mm, and 0.1-mm, respectively.*

As mentioned earlier, the interface threshold value is used defining the contact condition; a perfect or non-perfect contact. It is noted that this threshold value can be adapted or modified in the RSW model. Actually, this threshold value should be defined as small as possible in the case of the two deformable solids in firmly contact, which indicates that there is no separating distance at the interface.

The threshold value of 30 micrometers is defined in our models for non-coated sheet joining. Non-convergence is found at the beginning of the welding, because of strong temperature gradient and current flux concentration at the interface. It is noted that such strong gradient is also associated with the small contact size at the beginning of welding.

For joining non-coated sheet with *flat face electrode*, relative small threshold value can be defined for the electrode-to-sheet contact condition, e.g. 5-10 micrometers. This is because the contact size varies little.

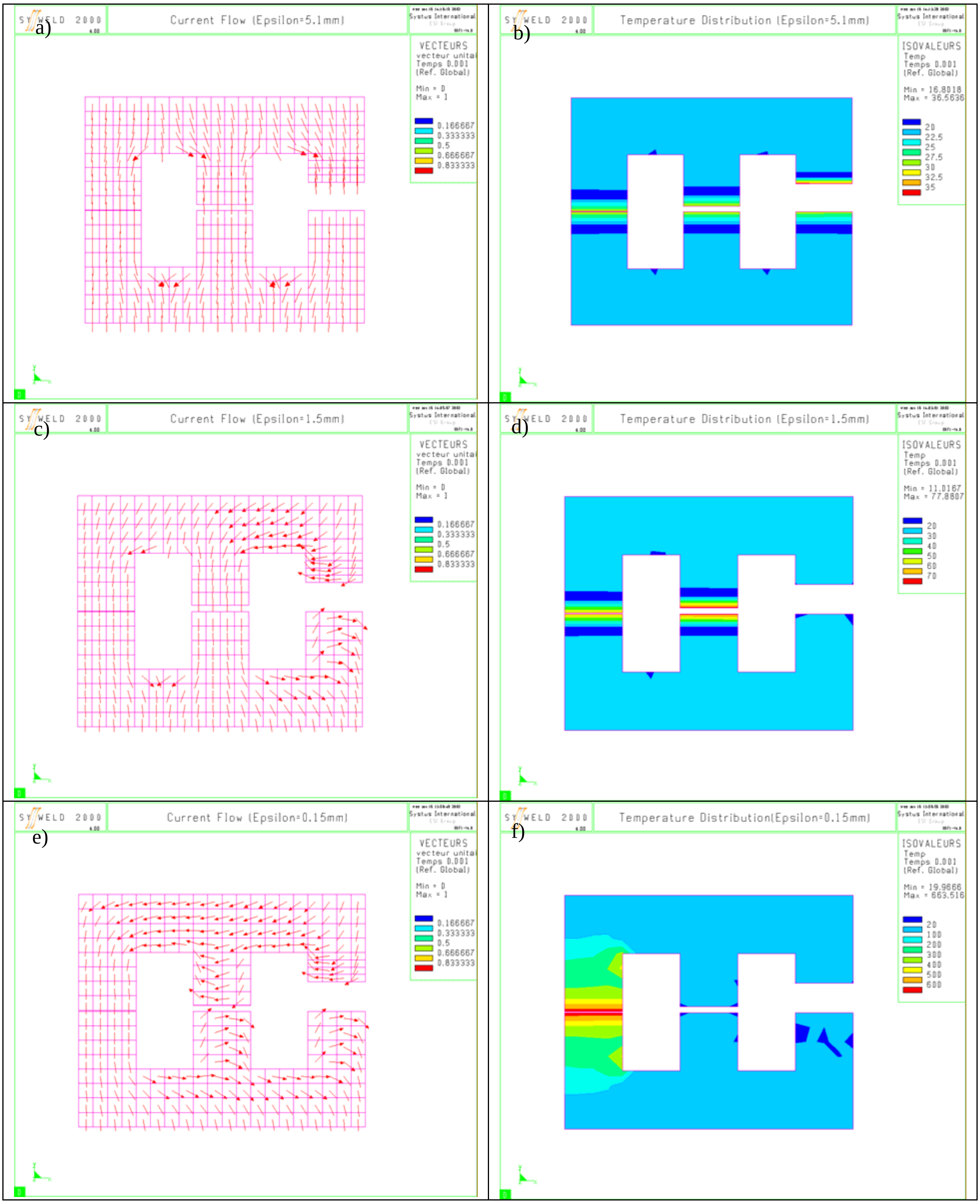

Fig. 3.10: *Demonstration of the current flux flowing across the gap, and as a result heat generation at the interfaces between two discs; a) Current flux flowing across three gaps with permissible value ε =5,1-mm., b) Simultaneous heat found at three interfaces, c) Current flux flowing across only two interfaces with permissible value ε =1,5-mm, (1,0-mm and 0,1-mm, are distances of both gaps, respectively) d) Heat occurs at two interfaces, where their gap distances are less than 1,5-mm., e) Current flowing across the centre disc when ε = 0,15-mm, f) Heat generation is observed the centre interface.*

For finite element analysis before the use of any model, it is still necessary to construct a simple model to verify the model variables every times. In this study, the contact model is verified with the use of a simple model. It is found that if the distance between the opposite meshes is greater than the interface permissible value, the current flux cannot transverse across the interface and there is no heat produced by contact resistance. This is a *non-perfect contact condition*. On the other hand, if the gap distance is less than or equals the threshold value, the current can flow across the interface, and thus the heat generation by Joule heating effect at the interface.

3.8 Results and Discussion:

Our papers are devoted to two principal modeling techniques; the decoupled, and the coupled analysis. Decoupled analysis presented is to study the influence of the electrothermal contact size on the thermal history, the nugget size, and the residual stresses in the assembly. The contact stress distribution and the thermal history occurring in the workpiece are reviewed in the first paper.

The second paper is devoted to a study on the influence of the supplementary pulsed schedule in high-strength steel joining. TRansformation Induced Plasticity steel grade 800, (TRIP800), is the steel used in the study. The influence of the pulse schedule is studied for thermal history in the nugget and the HAZ regions.

For the welding process simulation, material properties as a function of temperature are necessary to be included in the material database. In the third paper, the influence of electrical-thermal properties on the weld characteristics and the weld morphology validation are studied. The evaluation technique for the property at elevated temperature is presented. Moreover, the physical phenomena and the significant of the contact property in RSW are reported in this paper.

In the last section, the determination of the heating and cooling rates resulting from the simulation in order to provide the approximated heating and cooling rates for the Gleeble® machine test. This approximated cooling rates could be useful for characterize the residual microstructures in the HAZ.

❖ C. Srikunwong, T. Dupuy, and Y. Bienvenu: "A Decoupled Electrical-Thermal and Mechanical Model for Resistance Spot Welding", *Proc. 15th Seminar of Mechanical Engineering Network of Thailand*, Nov. 2001, Bangkok, Vol.2, pp. 76-84. (§prepared in manuscript format)

❖ C. Srikunwong, T. Dupuy, and Y. Bienvenu: "Numerical Simulation of Resistance Spot Welding Process using FEA Technique", *Proc. 13th International Conference on Computer Technology in Welding*, Siewert, T.A., ed., NIST and AWS, June 2003, Orlando, FL., pp. 53-64. (§prepared in manuscript format)

❖ C. Srikunwong, T. Dupuy and Y. Bienvenu: "Influence of Electrical-Thermal Physical Properties in Resistance Spot Welding Modelling", *Proc. 7th International Seminar on Numerical Analysis of Weldability*, H. Cerjak and H.K.D.H. Bhadeshia, eds., Oct. 2003, The Institute of Materials London. (§prepared in manuscript format)

A Decoupled Electrical – Thermal and Mechanical Model for Resistance Spot Welding

Chainarong SRIKUNWONG[1,2], Thomas DUPUY[2] and Yves BIENVENU[1]
[1]Centre des Matériaux P-M. Fourt, Ecole des Mines de Paris, F-91003, Evry cedex, France
E-mail: *DK.SRIKUNWO@ARCELOR.COM, Yves.Bienvenu@mat.ensmp.fr*
[2]CRDM, Arcelor Group, F-59381, Dunkerque cedex 1, France
E-mail: *thomas.dupuy@arcelor.com*

Abstract *Resistance spot welding is one of the major joining methods used in automotive body fabrication and assembly. It is well known that resistance spot welding is a very complex process. In order to profoundly understand the interactions among the electrical-thermal and mechanical aspects and simulate the physical phenomena of resistance spot welding, a 2-D axisymmetric finite element model with the decoupled electro-thermal and mechanical analyses for resistance spot welding was developed by employing a commercial finite element code, namely, Sysweld^{TM}. The assumptions introduced to the model : the Joule heating at the workpiece and the electrode interface, the latent heat of phase change due to melting was taken into account by utilizing the electro-thermal enthalpy model. The interfaces between the electrode-to-sheet and sheet-to-sheet contact were specially treated with artificial interface elements. Force and current were considered as principal welding parameters. A parametric study is carried out for the nugget growth with specific consideration of resistance spot welding of a similar non-coating sheet assembly.*

In addition, the electro-thermal contact resistances, mechanical contact models as well as material properties and characteristics were described as temperature-dependent functions throughout the study. During nugget formation stages, it was evidently disclosed that Joule heating at long welding times governs the nugget growth and heat generation at the faying surface dominates the nugget formation.

The influence of thermal contact model definition and size on nugget formation, thermal history and thermal-caused stress distributions in the assembly was determined. The mechanical - thermal analysis for the squeeze and weld stages were also investigated for each case of welding forces imposed to the model. Therefore, the influence of welding force on the stress distributions can be determined, especially for the squeeze phase of resistance spot welding.

Introduction

Resistance spot welding is widely applied in manufacturing industries for joining similar as well as dissimilar metal sheets. The major advantages of resistance spot welding are the followings :

1) High productivity : the time for one cycle of total RSW phases is less than one second.
2) Low cost : the conventional copper electrode can be easily utilized and replaced.
3) Wide range of applications for complex geometry and material combinations, especially for the automotive industry.
4) No mass added : suitable for light-weight structure.
5) Compatibility to automatic welding, controlling and monitoring processes.
6) Clean process : no slag occurring at the welding joint.

In resistance spot welding, the high current intensity flow and heat generation are localized at the weld point which is predetermined by the design of the electrode. In many applications of the automotive industries, the flat tip electrode is used as well as the curved tip electrode. Resistance spot welding process involves the interactions of electrical, thermal, mechanical and metallurgical phenomena. Concerning any assembly of sheets and electrode used, the principal parameters of resistance spot welding are welding current, force and duration of welding cycle. All parameters of resistance spot welding are strongly interrelated and lead to the determination of the weld lobe, which is a diagram used to determine the welding range for a certain type of sheet assembly. In order to determine the process parameters, to design electrodes or to choose the type and capacity of the welding machine while developing a new process in industry, a great number of running-in experiments have often to be undertaken. These increase the cost of products, time and in many cases delay the onset of production. For the above reasons, the application of computer simulation using numerical methods may save time and decrease cost-spent on the development of product or process, and reveal a more detailed information of the internal phenomena and thus facilitating a better understanding of the processes. In the present study, the numerical simulation modelling of the resistance spot welding process is carried out by using the commercial finite element code Sysweld^{TM}.

After the first remarkable work in finite element method for resistance spot welding of Nied [Ref.1] in 1984, FEM has been recognized as a powerful tool and effectively used to obtain a better understanding in RSW process. One of the chief features of the finite element techniques is the way curved boundaries can be realistically treated by using higher order isoparametric elements. Accurate solutions can be obtained in the region where the gradients are steep by refining the mesh.

Nied utilized commercial finite element code ANSYS and introduced a quarter axisymmetric model that accounted for the geometry of electrode and workpiece, the temperature-dependent properties and characteristics of materials. The melting and Joule heating effect were also included in the model. Predictions of the electrode and the workpiece deformations as well as the stress distributions along the interface were illustrated. The thermal analysis results showed that the isotherm forms in an elliptic nugget.

In 1990, Dickinson *et al.*, [Ref. 2], modeled the RSW process by using the ANSYS finite element code. The mechanical behavior of the welding process was coupled with transient thermal response during the entire welding cycle. The weld nugget formations in 347 stainless steel of equal and unequal sheet thickness and also joining 347 stainless steel to AISI 1045 steel workpiece were studied. The FEM analysis showed that the initial heat affected zone forms as a toroid shape and spreads rapidly toward the nugget center. This phenomena had also been reported in the work of Nied. For dissimilar material, the nugget forms in the low conductivity workpiece more than in the workpiece with higher thermal conductivity. For the unequal thickness sheet, the nugget forms mostly in the thicker workpiece due to longer current path. This study provided a comprehensive information about a coupled model for analyzing the interactions of various physical phenomena in resistance spot welding.

In 1991, Tsai *et al.*, [Ref. 3], studied the nugget formation and corresponding electrode displacement during the welding cycle. They proposed that the electrode displacement and its velocity can be used as the controlling parameters in a feedback control process monitoring. Tsai reported that the heat zone initiates at the periphery of the contact area and is in a toroid shape. In a very short time during the welding cycles, the molten nugget spreads rapidly inward toward the weld center.

In 1992, Vogler *et al.*, [Ref.4], studied the temperature history in RSW from the electrical-thermal-mechanical finite element models. The electrical contact size at the faying interface was predetermined by the mechanical analysis at the end of squeeze stage and maintained throughout the electro-thermal analysis. It revealed that the presence of electrical contact resistance affects the thermal history experienced in the assembly and the final nugget diameter. However, the influence of the electrical contact size variation on the thermal history and the nugget development was not addressed in their study.

Recently, Xu *et al.*, [Refs. 5-6], modeled and simulated the resistance spot welding process using ABAQUS code. An axisymmetric finite element model employing coupled mechanical-electrical-thermal model was presented. The latent heat of phase transformation was accounted for. A flat tip electrode and sinusoidal alternating current were utilized in the analysis. An electro-thermal element was introduced to the electrode-to-sheet interface. It revealed that heat transfer coefficient of the interface has a great influence on the nugget formation and thermal distribution in the workpiece. They also reported that the contact pressure distribution at the interface during the welding process depends on the temperature history, applied force, electrode shape, friction coefficient of the interface and most importantly on the temperature-dependent material properties.

In the aforementioned documentation, it is evident that the electro-thermal and mechanical decoupling of resistance spot welding has not been well addressed yet. In order to obtain a better understanding in the influence of RSW parameters, the decoupling of electro-thermal and mechanical aspects is introduced in the present study. A fully coupled electro-thermal model results the electrical current density, electrical field, temperature history, and nugget size and geometry. The thermal history obtained from the electro-thermal model will be used as thermal input data for the mechanical analysis at each considered time-step. The contact resistances of both electrode-to-sheet and sheet-to-sheet interfaces are treated with the artificial contact elements [Ref. 7] and the temperature-dependent properties and characteristics are given from various sources [Refs. 8-9]. Electrical and thermal resistances at the electrode-to-sheet and faying interfaces are described as functions of temperature based on the experimental work of [Ref. 8]. The influence of electro-thermal contact size at the faying interface on the thermal and stress results will be investigated by the variation of the faying interface diameter. The mechanical analysis provides the stress fields as well as the deformations, thus the contact stresses at the interface of both sheet-to-sheet and electrode-to-sheet can be determined.

Formulation for Modelling

A representative assembly of electrode and sheet utilized for analysis is shown in fig. 1. Fig. 2 illustrates a half axisymmetric finite element model for electrode and sheet assembly, which is considered for both electro-thermal and mechanical analyses.

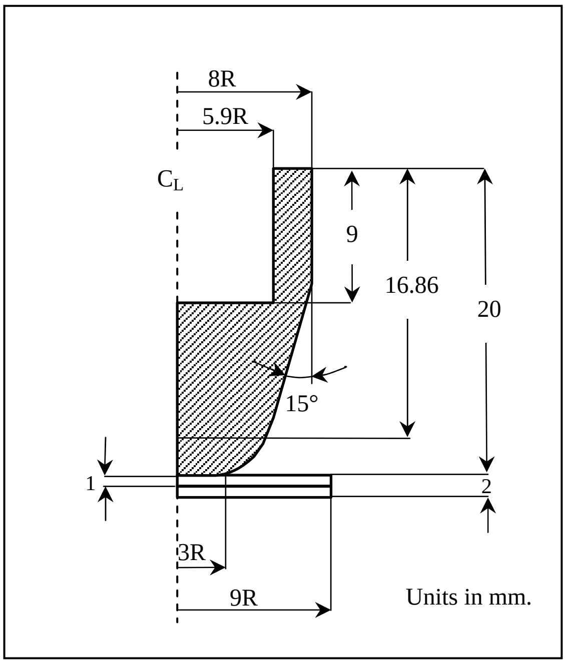

Fig. 1 *Schematic diagram of RSW assembly*

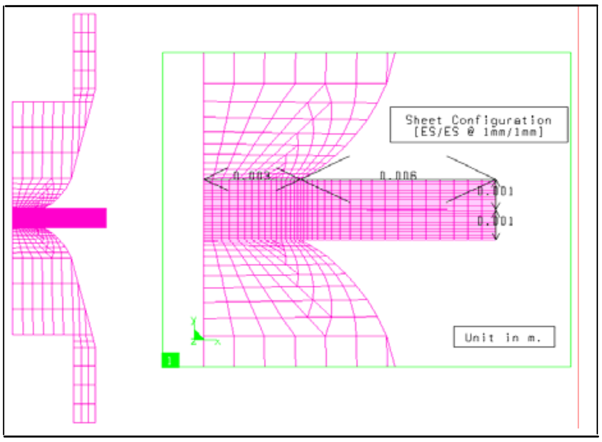

Fig. *2 Finite element mesh model*

Electro-Thermal Modelling

The thermal model includes the electrode geometry, applied current, Joule heating effect at the interface, interface heat transfer coefficient and enthalpy associated with phase transformation of sheet material. Temperature-dependent thermal and electrical properties are employed in the present study. Some examples of these properties are presented in fig. 3.

Before the beginning of welding cycle, the electrical initial conditions are set equal to zero, while the temperature of entire structure is specified as the room temperature. During the welding cycle, the AC current is applied at the top of the upper electrode and zero potential is specified at the bottom surface of the lower electrode. Consequently, the current flows from the upper electrode, passes through workpiece and terminates at the bottom annular section of the lower electrode. The electro-thermal boundary conditions imposed at the outer surfaces of both electrode and workpiece are air convection for where the surface temperature being equivalent to that of the ambient and radiation heat transfer mechanism for the considerable elevated surface-temperature. Fig. 4 illustrates the imposed electro-thermal boundary conditions.

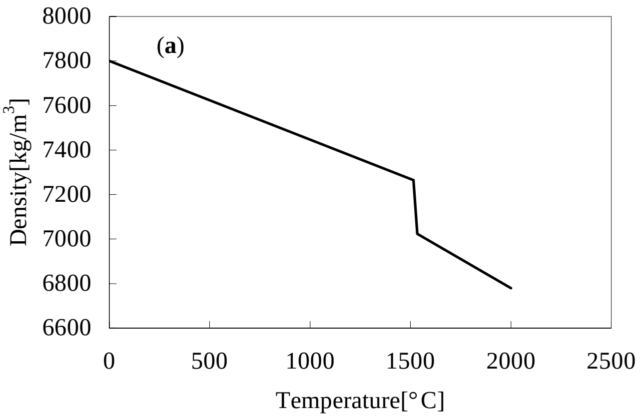

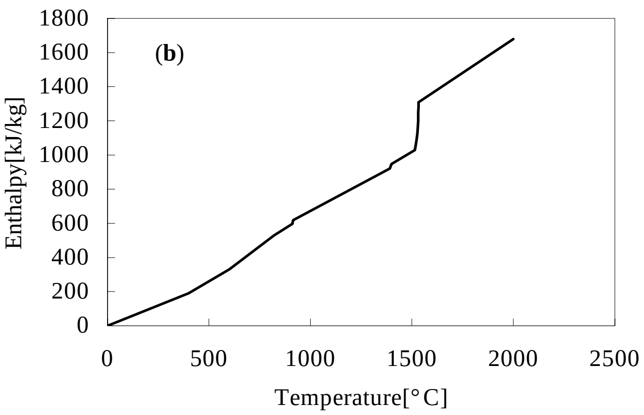

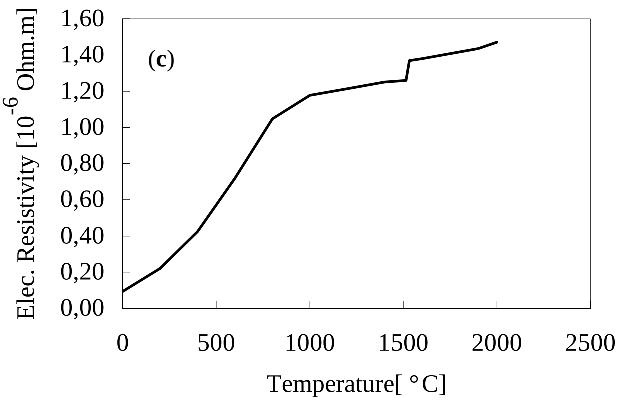

Fig. 3 *Properties and characteristics of steel sheet described as a function of temperature*

(a) Density

(b) Enthalpy

(c) Electrical resistivity

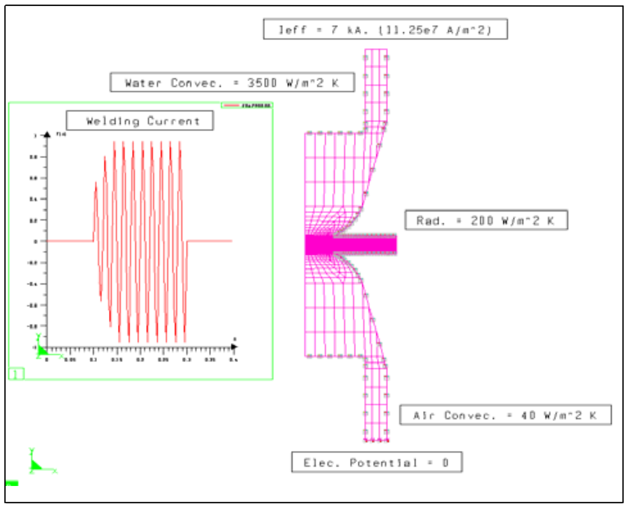

Fig. 4 *Electro-thermal boundary conditions*

Mechanical Modelling

The electrode force is applied since the beginning of the squeeze cycle until the end of the welding cycle. The mechanical boundary conditions imposed are the electrode force applied at the top surface of upper electrode by assuming a pressure distribution across the annular end, and the lower electrode annular section experienced the constrained condition by fixing the axial nodal displacement in y-direction. The radial nodal displacement of both workpiece and electrode are restricted along the entire axial axis corresponding to an axisymmetric boundary condition. The mechanical boundary conditions introduced to the model simulate the restrained boundary conditions experienced from producing a welding point by the pedestal welding machine.

The mechanical properties of electrode and sheet are described as the temperature-dependent functions. Some mechanical characteristics of sheet are presented in fig. 5. Fig. 6 illustrates the mechanical boundary conditions imposed to the structure.

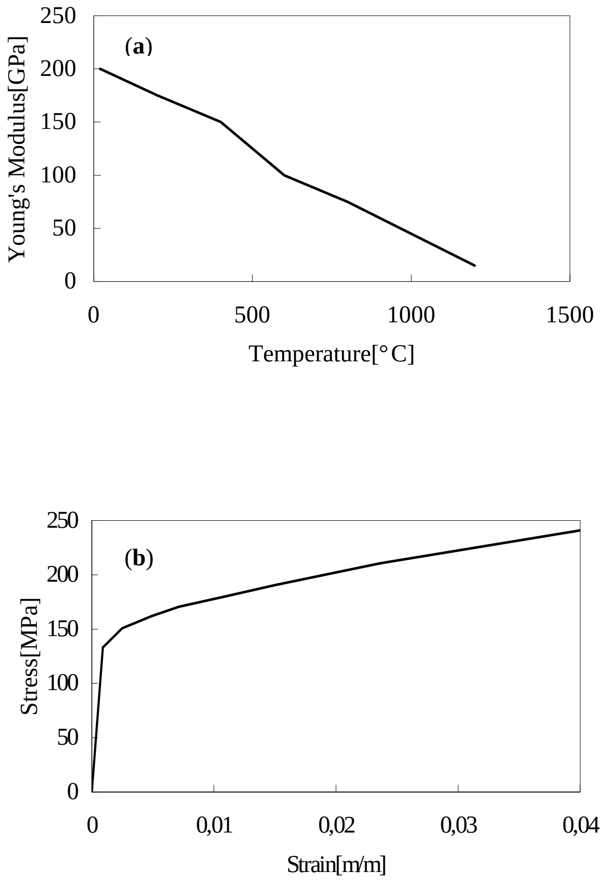

Fig. 5 *Temperature-dependent mechanical characteristics of sheet material*

(a) Young's modulus

(b) Stress-strain relationship at room temperature

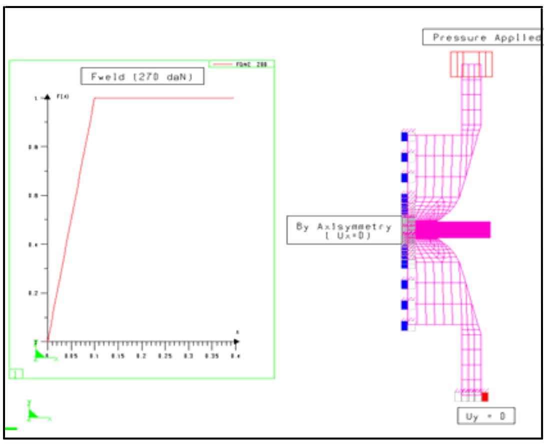

Fig. 6 *Mechanical boundary conditions*

Material Properties and Welding Schedule

Sheet material used in the analysis is drawing quality non-coating sheet, which is one of USINOR sheet products. Both sheets have the same thickness. Isotropic temperature-dependent properties and characteristics are specified for the electro-thermal as well as mechanical analyses. These properties are considered over a temperature ranging from room temperature to that above melting point. Material characteristics and properties introduced to the model can be concluded as the followings :

-Isotropic sheet material characteristics and properties.

-Temperature-dependent function described for both properties and mechanical characteristics of sheet, electrode as well as contact element.

A conventional copper electrode is employed and the welding schedule considered in present study is provided from [Ref. 10] corresponding to the practice. Welding conditions for non-coating sheet assembly are summarized as the followings :

Current	7.0-10.2 kA. [~AC. 50 Hz]
Welding force	250-320 daN.
Squeezing time	5 cycles. [0.1 second]
Welding time	10 cycles. [0.2 second]

According to process simulation, only the squeezing and welding phases are presented, since they are vital for the determination of the contact pressure distribution and the predicted nugget geometry.

Results and Discussion

Electro-Thermal Modelling

For this investigation, a welding cycle analysis is conducted to determine the current density and the temperature history experienced in the assembly and the nugget size and shape.

In order to determine the welding range from the simulation, the acceptable nugget diameter considered from the practice ranging from 4.0 to 6.0 mm. is taken into account as the weldability reference. The isotherms defined the nugget and HAZ sizes correspond to the fusion and the austenitic temperatures, respectively.

The welding range and the variation of weld nugget geometry with current at the end of the 10^{th} cycle resulted from simulation are shown in fig. 7. It shows that the effective current should be used is 9.35 kA. with 10 welding cycles in order to obtain the nugget diameter equal to 6 mm. In addition, the current range varied from 7.25 to 9.35 kA. provides an acceptable nugget size ranging from 4.0 to 6.0 mm.

The electro-thermal analysis reveals that the characteristic isothermal of an elliptic-shape weld nugget is always obtained at the end of welding phase as shown in fig. 7(a). Fig. 7(b) illustrates the nugget diameter size as a function of welding current. Increasing in the welding current will also increase the nugget diameter. The weld nugget is generated by the Joule heating effect occurring at the faying interface and this generation dominates the nugget formation development.

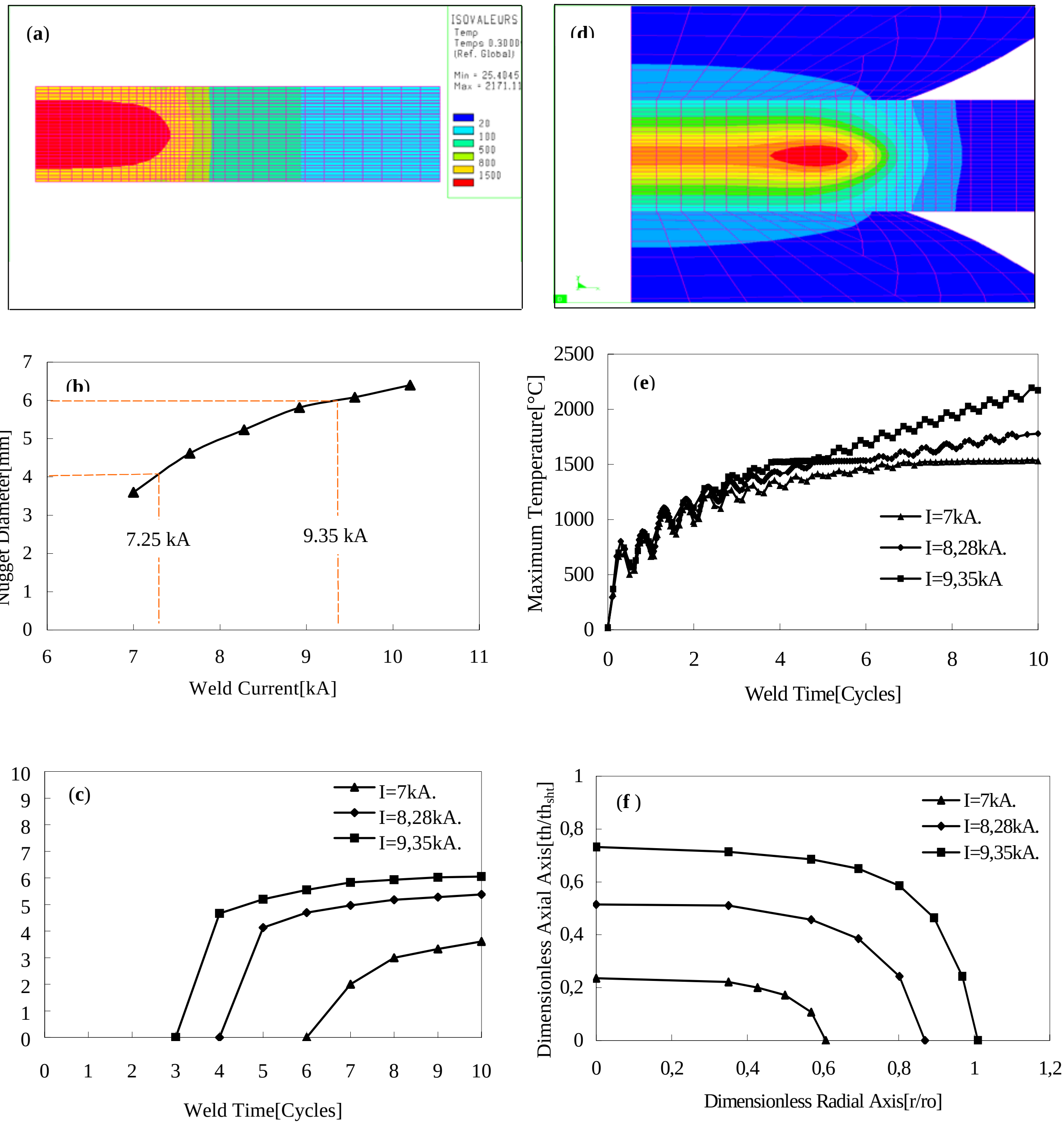

Fig. 7 *Effect of welding current on nugget size and thermal history experienced in the workpiece*

(a) Elliptic nugget geometry at the end of welding cycle.
(case I=9.35kA)

(b) Predicted nugget diameters as a function of welding current at the end of the 10^{th} cycle and the welding range resulted from simulation.

(c) Predicted nugget diameter evolutions as function of welding time.

(d) Early heat zone as a toroid shape occurs at the faying interface.
(case I=9.35kA@ the end of the 2^{nd} cycle)

(e) Maximum temperatures occurring at the nugget center as function of welding time for considered welding currents.

(f) Dimensionless nugget geometry variation with the welding current at the end of welding.

It is well known that only the electro-thermal model can provide an elliptic geometry of nugget. This nugget formation has been observed since the first RSW thermal analysis of Greenwood [Ref. 11]. Comparison of nugget diameter prediction and welding time is presented in fig. 7(c) for welding currents varied from 7 to 9.35 kA. It reveals that the higher welding current is applied, the earlier nugget forms in the shorter welding cycles. The nugget diameter development almost saturates after the 7^{th} cycle and the 8^{th} cycle for the welding currents equal to 9.35 and 8.28 kA., respectively. It is noted that the nugget starts forming about the fourth cycle for the welding current equal to 9.35 kA.

Fig. 7(d) shows the an early toroid heat zone initiates at the periphery of sheet-to-sheet interface at the end of the second welding cycle. According to the flat tip electrode used in simulation, the singularity of current occurs at this interface of contact and this generates the heat affected zone at the periphery of the contact during the welding stage. Shortly after that, the heat affected zone becomes the molten nugget, which spreads rapidly inward toward the nugget center. There is very little nugget growth in the outward radial direction. Fig. 8(b) supports this discussion after the fourth cycle in case of 9.35 kA. applied.

The maximum temperature of the weld center experienced in the workpiece for each case of welding current is illustrated in fig.7(e). It is obvious that the increase in welding current will result in higher maximum temperature reached at the weld center. It can be observed that there are slightly differences in maximum temperature history reached at the nugget center for the early welding stages and these differences in temperature increase significantly after the nugget center thermal cycle reaches the fusion state. In case of the welding current 9.35 kA., the maximum temperature cycle reaches the fusion temperature of sheet material at the end of the fourth cycle and increases markedly after the fifth cycle. The higher current applied, the more rapidly increases in the maximum temperature at the nugget center. However, these are strongly dependent on the electrode tip shape used in the simulation as described elsewhere [Ref. 12].

Fig. 7(f) depicts the dimensionless nugget geometry for the different cases of welding current. As expected, the increase in current also increases both height and diameter of nugget. Therefore, the current is considered as one of the important parameters in RSW process.

Temperature distribution along the faying surface as function of welding time is illustrated in fig. 8(a). It can be seen that the maximum temperature occurs near the periphery of sheet-to-sheet interface at the second welding cycle due to the fact that the current singularity induces the first heat affected zone at this region. In addition, the temperature distribution can be characterized as bell shape. The considerable drop in temperature can be also observed near the outer rim of the contact during the welding cycle. Fig. 8(b) reveals that the nugget develops more rapidly in the axial direction than that in the radial direction as the welding cycle increases concerning the flat tip electrode used in the simulation. In the case of current equal to 9.35 kA, the molten nugget forms firstly at the 4^{th} cycle and increases in both diameter and height during latter welding stages.

Fig. 9 shows the influence of electro-thermal contact size at the sheet-to-sheet interface on the thermal history and the nugget size. As expected, the increase in the contact size results in the decrease of the maximum temperature reached at the end of welding as well as the final nugget size. The difference in temperature at the end of welding phase comparing the thermal contact size equal to electrode diameter to that equal to one hundred and forty percents of electrode diameter is 196 °C as shown in fig. 9(a). The temperatures are slightly higher for the larger thermal contact size in the early stages of welding, in contrast to the end of welding phase, the maximum temperature profile is higher in case of smaller contact size. It has been shown that the thermal contact size influences the final nugget size as illustrated in fig. 9(b). The increase in electro-thermal contact size at sheet-to-sheet will directly reduce the nugget size.

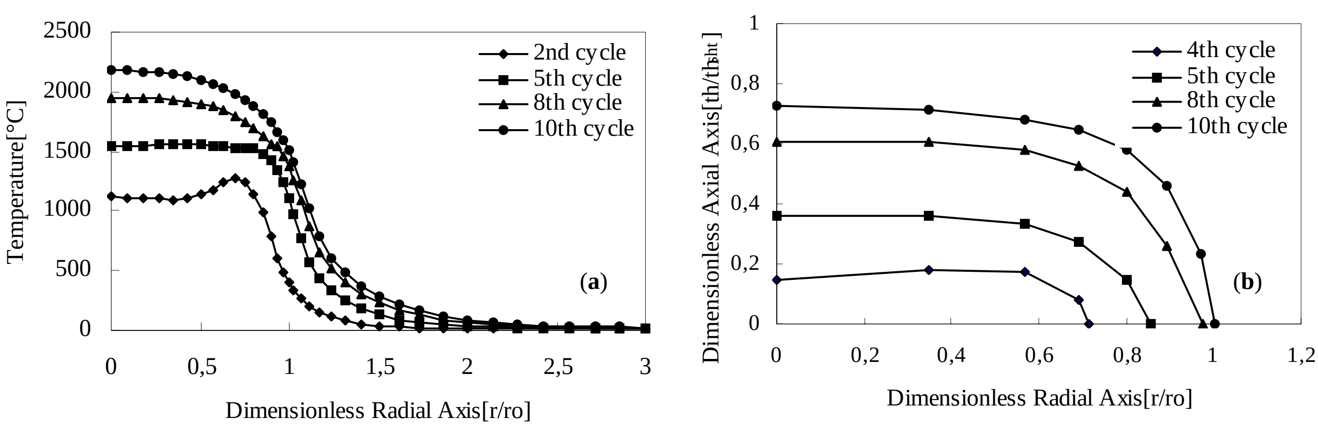

Fig. 8 *Effect of welding time on thermal history and nugget size in the assembly (I=9.35 kA.)*
(a) Thermal history experienced along the faying surface. (b) Dimensionless nugget geometry vs. welding time.

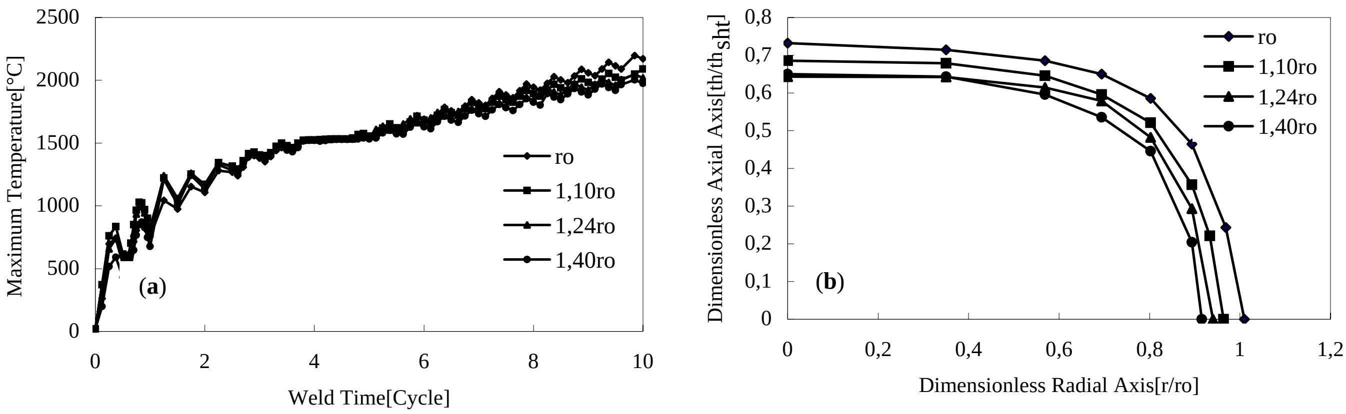

Fig. 9 *Effect of thermal contact size on thermal history at nugget center and final nugget size (I=9.35 kA.)*
(a) Thermal history evolution at nugget center.
(b) Dimensionless nugget geometry for different size of thermal contact at the end of welding.

Mechanical Modelling

The mechanical analysis determines the contact stress occurring at both sheet-to-sheet and electrode-to-sheet interfaces as well as the assembly deformation for the squeeze phase. The contact pressure distributions along the electrode-to-sheet and sheet-to-sheet interfaces are illustrated in fig. 10 for the squeeze phase with the various welding forces. The results indicate that once the squeeze force increases, the contact pressure also increases for both electrode-to-sheet and sheet-to-sheet interfaces. As expected, maximum contact stresses are found at the outer rim of the electrode-to-sheet interface while maximum normal stress of workpiece faying surface occurs near the periphery of contact region. The comparison of contact pressure at the end of squeeze phase reveals that the interface stress is not uniformly distributed for each case of squeeze force applied, it starts from a lower value at the axial axis and increases gradually in the radial direction of the assembly for the faying interface. The considerable drop in contact pressure can be seen at the periphery region for the faying interface. These stress concentrations at the periphery, especially for the faying interface, have a pitching effect, which can prevent molten metal of the nugget volume from the splashing.

Fig. 11 shows the predicted electrode-to-sheet contact pressure distributions for the applied force equal to 270 daN associated with various welding cycles. The results indicate that maximum pressure concentration occurs initially at the outer rim of the electrode face after the squeeze phase. When the welding current is switched on, the pressure for the center portion of electrode-to-sheet interface is noticeably shifted from 50 to 150 MPa. during the first three cycles. This instantaneous increase in the interface contact stress only occurs in the early welding stages. In the latter welding stages, in contrast to the beginning of weld, contact pressure decreases gradually for the inner-center portion of electrode-to-sheet interface while the stress concentration can be observed at the outer rim of electrode-to-sheet interface. This contact stress concentration varies during the welding cycle and its maximum appears at the fifth cycle.

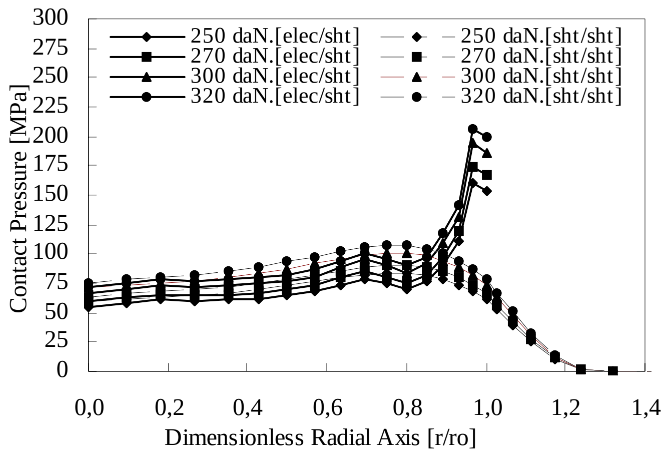

Fig. 10 *Comparison of contact pressure at the end of squeezing phase for various welding forces applied*

Although their model employed the coupled electrical-thermal-mechanical analysis, [Ref. 13] also reported the similar contact pressure distribution to that obtained from the present study. The combined effects of the plastic deformation due to the stress concentration at the electrode face periphery and the thermal deformation can probably cause the pitting effect at the electrode face, thus establishing the electrode degradation in the applications.

The comparison of Von-Mises stresses on electrode-to-sheet interface at the end of squeeze phase in case of different welding forces is illustrated in fig. 12. The Von-Mises stress distributions at the electrode-to-sheet interface exhibit the same manner as that of axial contact stress. Maximum Von-Mises stress occurs at the periphery of the interface and drops drastically for the region, which is no contact interface between electrode-to-sheet. During the welding cycle, the Von-Mises stress at the end of the third cycle for the inner portion of the interface due to the thermal expansion of the assembly

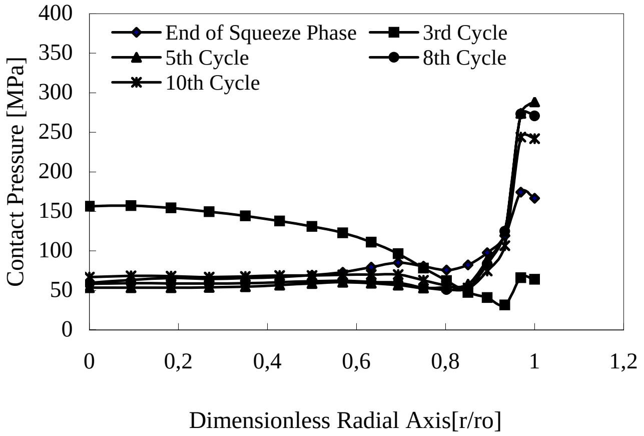

Fig. 11 *Pressure distribution at electrode/sheet interface (I=9.35 kA. and F=270 daN)*

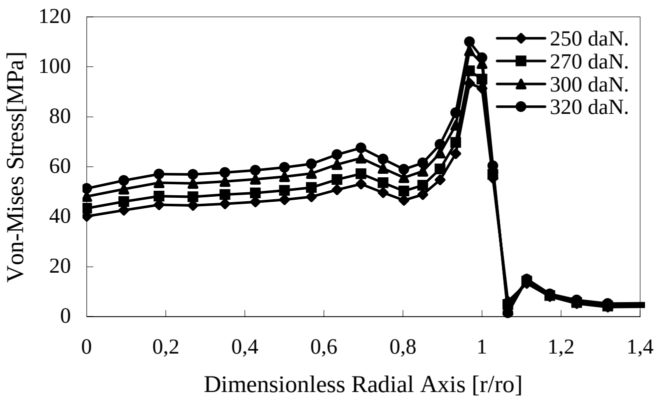

Fig. 12 *Comparison of Von-Mises stress at electrode/sheet interface for the end of squeeze phase*

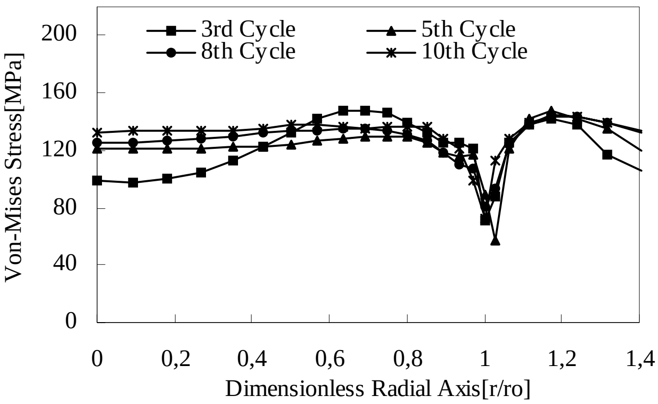

Fig. 13 *Comparison of Von-Mises stress at electrode/sheet interface during welding phase (I = 9.35 kA. and F=270 daN)*

during the welding phase and a significant drop in the Von-Mises stress profile can be seen at the outer rim of the contact as shown in fig. 13. The Von-Mises stress evolutions and the edge separation of the assembly during

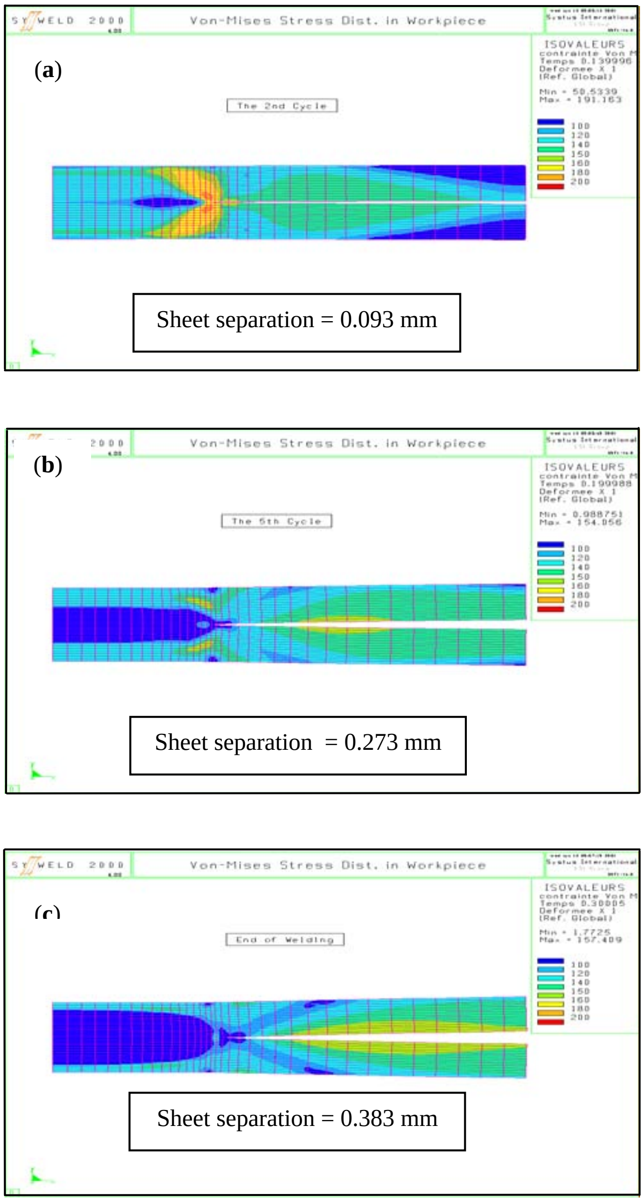

Fig.14 *Von-Mises stress evolutions and assembly deformations during the welding phase (I=9.35 kA. and F=270 daN)*
(a) @ second cycle
(b) @ fifth cycle
(c) @ end of welding

the welding phase are illustrated in fig. 14.

Conclusions and Future Work

The Finite element method with the present of decoupling among electro-thermal and mechanical aspects has been developed and provided a better understanding of the internal phenomena of RSW process including the nugget development, the thermal distributions and variations, as well as the interface stress distributions during the squeezing and the welding phases.

The conclusions for the present study can be drawn as the followings :

1. It was demonstrated that the electro-thermal contact size introduced to the faying surface dominates an important role not only on the final nugget size but also on the thermal history experienced in the workpiece. The first HAZ initiates at the periphery of the faying contact and forms as toroid shape in the early stages of welding due to the current singularity. The HAZ grows rapidly inward and toward the axial axis and it becomes the nugget in the latter stages. This is the case of flat face electrode used. The acceptable nugget diameters found from the practice were employed as the weldability references compared to the simulation results, thus the electro-thermal model can provide the quantitative welding lobe.

2. A contact pressure concentration for the electrode-to-sheet interface always occurs at the interface periphery and increases with the increase of the welding force applied. Contact pressure profiles for both electrode-to-sheet and faying interfaces are not uniformly distributed at the end of squeeze as well as during welding phases.

3. The temperature-dependent properties and characteristics for both electrode and sheet must necessarily be taken into account to the model in order to obtain more accurate simulation results. Therefore, the properties and the characteristics of sheet material will be experimentally investigated and introduced to the electro-thermal and mechanical coupled model, which will consider the RSW process with the applications of both flat and curved tip electrodes producing the spot weld.

4. The coupling among the electro-thermal and mechanical aspects is important in order to construct a model approaching more realistically to the RSW process. In addition, the experimental validations for the on-going work have to be established in order to prove the consistency of the simulation and provide the limitation of the model.

Acknowledgements

The authors would like to express their grateful acknowledgement to Mr. G. RIGAUT, the director of the Metallurgical Development and Research Center of SOLLAC Atlantique, Dunkerque, for his authorisation to prepare these papers as well as tremendous support.

Mr. J. CLAEYS, the head of resistance welding section, and Mr O. DIERAERT, the former head of resistance welding section, are gratefully acknowledged for their support.

References

[**1**] Nied, H.A., *1984*, The finite element modelling of the resistance spot welding process, *Welding journal* 63(4) : pp. 123s to 132s.

[**2**] Dickinson, D.W., Tsai, C.L . and Jammal, O., *Feb.26-Mar2. 1990*, Modelling of RSW nugget growth-application for the automotive industry, *International congress and exposition*, Detroit, Michigan.

[**3**] Tsai, C.L., Dai, W.L., Dickinson, D.W. and Papritan, J.C., *Dec.1991*, Analysis and development of a real-time control methodology in resistance spot welding, *Welding journal* : pp. 339s to 357s.

[**4**] Vogler, M.M., and Sheppard, S.D., *June 1-5 1992*, A study of temperature histories in resistance spot welding, *International trend in welding science and technology*, Proceedings of the 3rd int. conference on trends in welding research, Gatlinburg Tennessee, ASM : pp. 57 to 61.

[**5**] Xu, L. and Khan, J.A., *June 1998*, Finite element modelling of axisymmetric nugget development during resistance spot welding, *Trends in welding research* : pp. 616 to 621.

[**6**] Khan, J.A., Xu, L. and Chao, Y.J., *1999*, Prediction of nugget development during resistance spot welding using coupled thermal-electrical-mechanical model, *Sciences and technology of welding and joining*, Vol. 4 No.4 : pp. 201 to 207.

[**7**] SYSTUS™ 2000**,** *Analysis reference manuals***,** Vols. 1-4, *Edition 2000*, ESI group.

[**8**] Thiéblemont, E., *1992*, Modèlisation du soudage par points, *Ph.D. dissertation***,** L'Institut National Polytechnique de Lorraine.(in French)

[**9**] Metals handbook (Desk edition) the 8th Edition, *1995*, *American society for metals*

[**10**] Caractérisation de la soudabilité par résistance par point de produits plats revêtus ou non, *Déc. 1994*, *Normalisation française A87-001*.

[**11**] Greenwood, J.A., *1961*, Temperature in spot welding, *British welding journal* : pp. 316 to 322.

[**12**] Murakawa, H., Kimura, F. and Ueda, Y., *the 1st edition 1997*, Weldability analysis of spot welding on aluminium using FEM, *Mathematical modelling of weld phenomena 3* : pp. 944 to 966.

[**13**] Dong, P., Victor Li, M. and Kimchi, M., *1998*, Finite element analysis of electrode wear mechnisms : face extrusion and pitting effects, *Science and technology of welding and joining*, Vol. 3, N° 2. : pp. 59 to 64.

NUMERICAL SIMULATION OF RESISTANCE SPOT WELDING PROCESS USING FEA TECHNIQUE

C. Srikunwong[*,], T. Dupuy[*], and Y. Bienvenu[**]**

ABSTRACT

2-D axisymmetric finite element models incorporating electrical-thermal and thermal-mechanical coupling procedures were developed for resistance spot welding (RSW) process simulation. A commercial finite element code, namely Sysweld™, was utilized for these simulation purposes. The coupling procedures can provide a more realistic and efficient computational approach accounting for the variation of contact size; particularly for the application of curved-face electrodes producing a spot weld. The temperature dependency characteristics and properties of both sheets and electrodes were also taken into account throughout the study. The welding schedules based on practical aspects of similar two- as well as three-sheet assemblies were considered for the entire of process. Not only the utilization of pulsed direct current but also that of pulsed alternating current was utilized in order to efficiently achieve the industrial protocol. The experimental study was centered on nugget formation. The validation for the nugget development was determined in the case of pulsed direct current welding.

The impact of pulsed alternating current welding combining supplementary post-heating pulses on the nugget size as well as on the thermal history was investigated. It was concluded that both heating and cooling rates depend strongly on the position of weld. The results of electrical-thermal analysis were discussed in view of the thermal history during welding, with particular regard for different types of welding current used.

INTRODUCTION

Resistance spot welding (RSW) is widely utilized as a joining technique for automobile structure due to flexibility, robustness and high-speed of process combining with very high quality joints at very low cost. Not only heavy gauge two-sheet assemblies are joined by this technique but also stack-up sheet assemblies can often be encountered in the application. In some cases of heavy gauge two-sheet joining, the use of a common continuous current signal is sometimes not efficient to construct the desired weldability lobe. The pulsed welding approach then becomes an other choice to achieve this purpose. The pulsed welding current based schedule is sometimes recommended for heavy gauge and stack-up assembly cases associated with some welding signal modification in order to improve weldability and mechanical properties of spot weld. The pulse current used can be medium frequency direct or alternating current pulse. Other adapted current signal such as down sloping, quenching or post-heating can be also introduced to a required welding current signal. These modifications become a common convenient technique for the improvement of weld mechanical-metallurgical properties in high strength steel joining (Ref. 1). The use of pulsed welding has many advantages in heavy gauge sheet joining including the stability of nugget development characteristics and the reduction of electrode wear.

* CRDM, Sollac Atlantique, ARCELOR Group, BP 2508, 59381, Dunkirk, France
** Ecole des Mines de Paris, BP 87, Evry Cedex, 91003, France

The recent development in finite element analysis for RSW numerical simulation is well documented in the literature (Refs. 2 and 3) showing that there is a significant change in the contact radii between electrode-to-sheet and sheet-to-sheet interfaces during welding stage. This has significative impacts on thermal history, nugget formation and thermal stresses in the assembly. Therefore, it is vital to implement a coupling procedure between electrical-thermal and thermal-mechanical modules in order to capture this physical interaction and produce a more realistic predictive model.

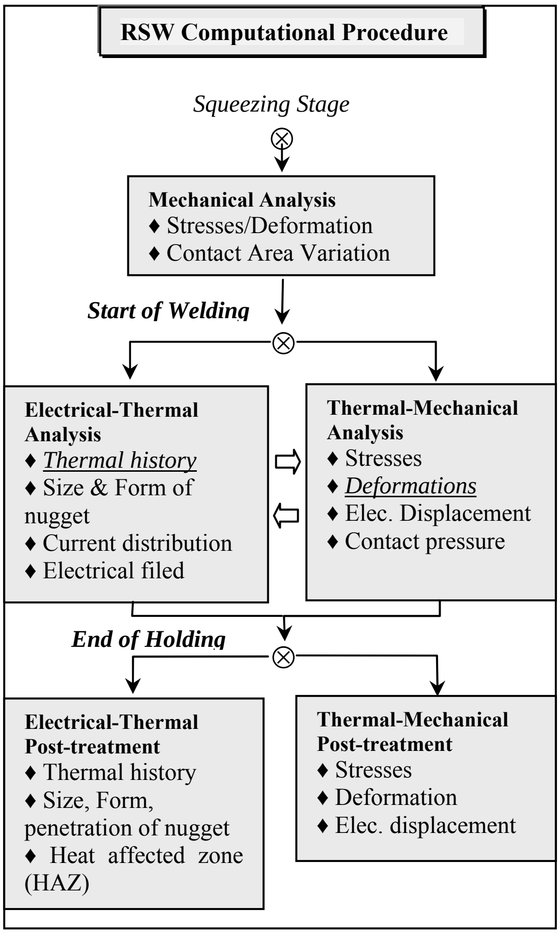

Figure 1: Schematic illustration of computational procedure

The aim of this study is to obtain a better understanding of the influence of process parameters for heavy gauge sheet joining with the use of pulsed welding current. The features of the coupling procedures can be described by loop sequential computational procedures of the nodal temperatures transferred from the electrical-thermal analysis to the thermo-mechanical analysis in order to compute the thermal stresses and assembly distortions. On the other hand, the stress distributions associated with assembly deformation are then transferred back to the next electro-thermal computation step in order to up-date the variation of the contact size and pressure. These successive sequential loops are cumulated until the end of RSW process. The computational procedure employed in this study is illustrated in fig. 1.

FORMULATION FOR MODELING

Structure Modeling

A representative assembly of electrode and sheet utilized for analysis as shown in fig. 2 illustrates a half axisymmetric finite element model for electrode and sheet assembly, which is considered for both electrical-thermal and thermal-mechanical analyses. 2-D axisymmetric models of two- and three-sheet joining incorporated with the curved face electrode of 6mm and 8mm.-diameter are constructed. Both electrical-thermal and mechanical contact elements are specially treated at electrode-to-sheet and sheet-to-sheet interfaces.

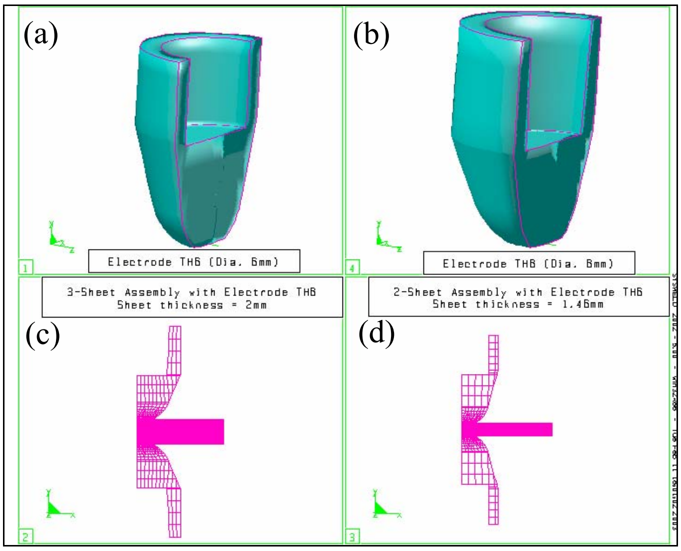

Figure 2: Illustration of structure mesh models used in analysis
Figure 2a: Curved-face electrode of 6mm-dia; Figure 2b: Curved-face electrode of 8mm-dia
Figure 2c: Three-sheet assembly mesh model; Figure 2d: Two-sheet assembly mesh model

Electrical-Thermal Modeling

RSW process is a resistance welding process governed by Joule heating effect with a concentration of the heat generation at the interface between two solid bodies in contact while passing the current. This heat further propagates into these bodies by conduction heat transfer mode associated with the imposed thermal boundary conditions. Electrical-thermal governing system equations are presented in (1) and (2):

$$\rho\frac{\partial H}{\partial t} - div(\lambda.\mathbf{grad}T) - \mathbf{gradV}.\sigma.\mathbf{gradV} - Q = 0 \quad (1)$$

$$div(\sigma.\mathbf{gradV}) = 0 \quad (2)$$

Where T, $\mathbf{V}$ are the temperature and the scalar electrical potential, respectively. ρ, λ and σ represent the density, the thermal conductivity and the electrical conductivity of the medium. The temperature dependency characteristics can be taken into account in these equations. H is the enthalpy also with a temperature dependency. The full coupling between electrical and thermal phenomena can be governed by the term $\mathbf{gradV}.\sigma.\mathbf{gradV}$ in the heat equation. The modeled alternating current signal used in the analysis is shown in fig. 3a.

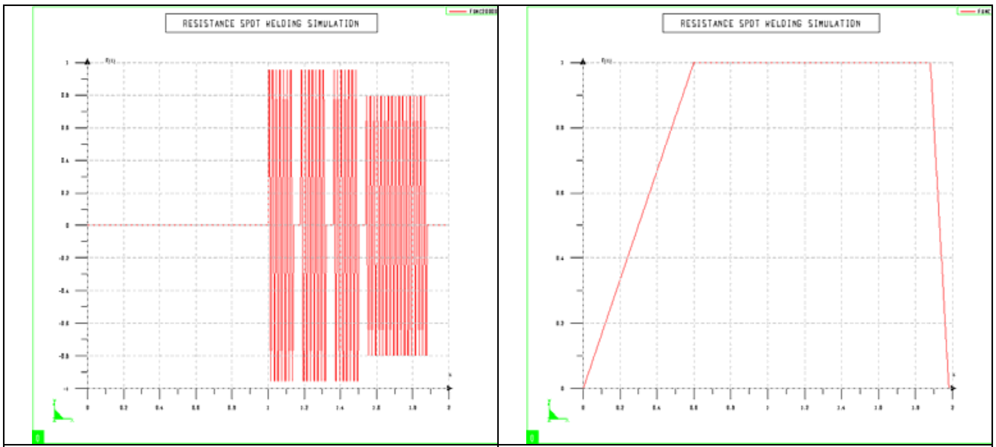

(a) Pulsed welding current: I[t] (b) Welding force: F[t]

Figure 3: Modeled welding signals used in analysis

Thermal-Mechanical Modeling

The electrode force as illustrated in fig. 3b is modeled from the welding force signal. The mechanical boundary conditions (Ref. 4) are the electrode force applied at the top surface of the upper electrode by assuming a uniform pressure distribution across the annular end and the vertical nodal displacement of annular end of the lower electrode, which is constrained similar manner to that of practical weld. The elasto–plastic Von-Mises criterion without deformation rate dependency is defined for sheet characteristics. The non-linearity due to temperature dependency of sheet properties and contact characteristics including transient computational approach are considered for this study. The three governing equations, namely, the compatibility condition, the constitutive relation, and the equilibrium equation in cylindrical co-ordinate are discussed elsewhere (Ref.5).

EXPERIMENTAL PROCEDURE

Two sheet grades of ARCELOR, a Transformation Induced Plasticity (TRIP) grade and a non-coated drawing quality Low Carbon Steel (LCS) sheet are utilized in this study. Properties of both sheets are given in Refs 6 and 7. The metallurgical examination is conducted only for the low carbon steel sheet joining.

Table 1: Welding schedules utilized in the study

Welding conditions		Current: [kA/Cycles] Force
Elec. dia. (mm)	Configuration	
1) 8	2sheets:(LCS) 2mm-thick	11.2-DC/4(6+2) 400 daN
2) 6	2sheets:(LCS) 2mm-thick	8.97-DC/4(6+2) 400 daN
3) 8	3sheets:(LCS) 2mm-thick	10.6-DC/4(6+2) 450 daN
4) 6	2sheets:(TRIP) 1.46mm-thick	7.80-AC/3(7+2)+6.5×17 500 daN

Welding schedules in table 1 indicate the utilization of pulsed welding current. In the case of TRIP steel sheet joining with electrode face diameter of 6mm., alternating current with a magnitude of 7,80 kA is applied for 3 pulses, each pulse has 7 cycles of welding plus 2 cycles of current shut-off. Furthermore, the post-heating current is then applied for 17 cycles with a magnitude of 6.5 kA. The aim of post-heating current application is to achieve the good quality of residual metallurgical phases and minimize the weld fracture of HSS sheet joining. The as-received sheets are cut to 50×50-mm coupons. Electrode conditioning prior to welding is performed for 50 welding points with bare sheet. The trial welding tests are then conducted in order to determine the expulsion limit. These trial welding conditions are based on the French Industrial Standard (Ref.8), which is considered as welding schedule guideline. The welding schedules, just below the expulsion limit, are used for three welding coupons and for each pulse in order to examine the formation of nugget relating to configurations. The no-expulsion welding of each pulse can be verified from the force and the displacement signal monitoring on the LABVIEW® window. The effective current magnitude is obtained from the MIYASHI® current signal recorder. Nugget development kinetics can be further examined by sectioning the spot after each interrupted pulse. The polished axial sections of spot welded samples are etched with picric acid to determine the fusion line or the nugget contour. This etchant is suitable for the examination of the fusion zone of low carbon steel spot welds. Quantitative macro-photographic measurements are made for the nugget size.

EXPERIMENTAL RESULTS AND DISCUSSION

Influence of Process Characteristics on Nugget Formation

Nugget development kinetics for two and three LCS sheet joining of 2mm-thick at the end of each pulse is shown in fig. 4. As expected, both the height and the diameter of the nugget increase at the end of the first two pulses. During the third and the fourth pulse, the nugget expands more in diameter than in height. The indentation on the sheet surfaces and the sheet separation can also be observed. The influence of electrode face diameter on nugget formation is demonstrated by comparing case 1 and 2. It is revealed that the increase of electrode diameter face leads to the increase in magnitude of welding current by around 2.2kA if the electrode face diameter of 8 mm is used instead of 6 mm. This is due to the enlargement of contact size reducing the concentration of current flux at faying surface. The utilization of smaller electrode face diameter results in remarkable indentation onto sheet surfaces at the end of welding. Concerning the nugget formation kinetics in the case of two-sheet joining, the occurrence of nugget at faying surface is already observed at the end of the first pulse.

In the case 3, instead of initiating at center of three-sheet assembly, the hot zone originates in superior and inferior regions at the end of the first pulse but the nugget does not start forming yet. For the latter pulses, nugget penetration and development also show a trend similar to that of two-sheet assembly case. The dissymmetry in the upper and the lower nugget diameters can be found before the saturation of nugget diameter at the end of the fourth pulse. However, both symmetrical or dissymmetrical nugget development can be observed for three-sheet joining case. The sheet edge separation between faying surfaces is slightly different. The decrease in current magnitude for the three-sheet assembly comparing to that of two-sheet joining can be explained by the increase of bulk electrical resistance with the increase in number of sheets.

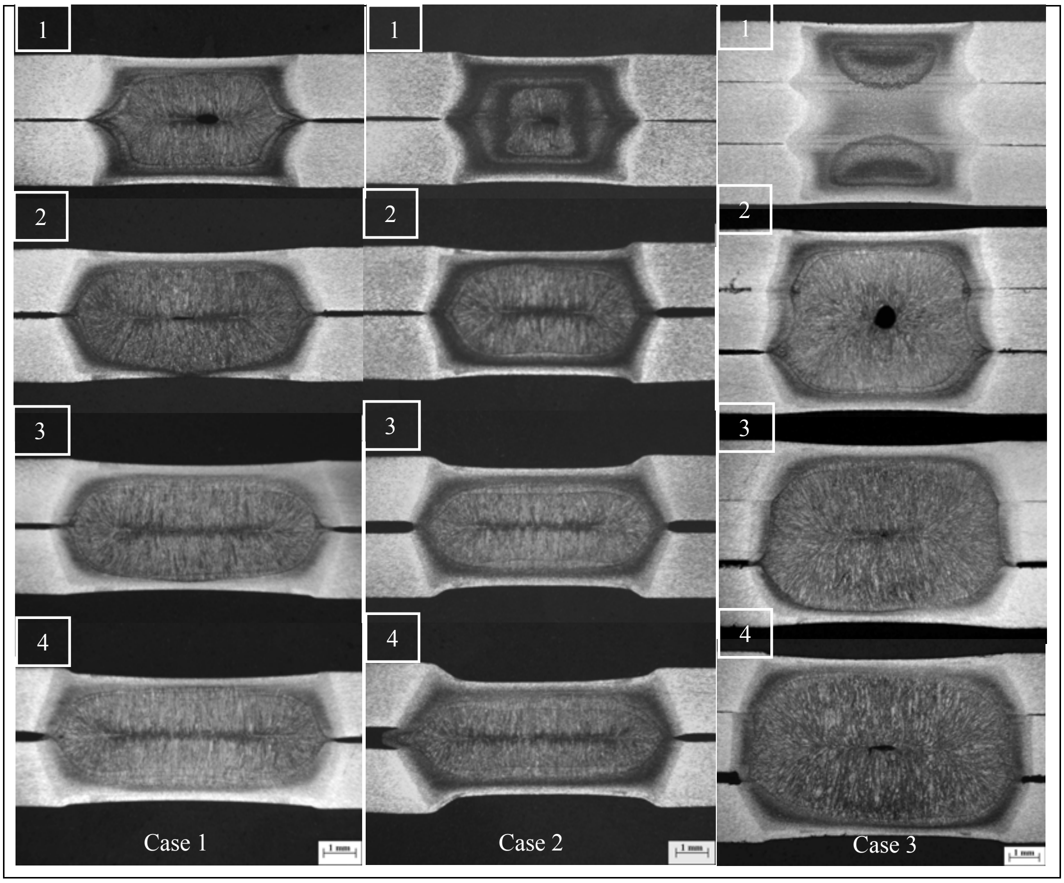

Figure 4: Illustration of nugget formation of two- and three-sheet assembly at the end of each pulse (Number of pulse is indicated on the macro-photograph and see also table 1 for the case study)

COMPUTATIONAL RESULTS AND DISCUSSION

Influence of Process Characteristics on Thermal History

For two-sheet joining case, the temperature history at different positions demonstrates the same dynamic response to the type of welding current used. The drop in temperature during current shut-off can be obviously observed on temperature evolution and markedly seen for the positions located in the nugget region as illustrated in fig.5a. The instantaneous significant increase in heating rate is found during the first pulse, particularly at the beginning. In contrast to the heating rate of weld center for two-sheet joining, there is no significant change in heating rate during the first two pulses for three-sheet joining as shown in fig 5b. An insignificant variation is seen for weld center thermal history during the current shut-off between the first and the second pulses.

For both two- and three-sheet joining cases, There is no variation in thermal history for the positions located far away from the nugget and the HAZ, i.e. r=8mm., during the weld stage. Unfortunately for the sheet joining with RSW technique, it is not easy to attain the same value of the maximum temperature in order to compare the thermal histories. This is due to the difference in the inherent welding parameters and the configuration used.

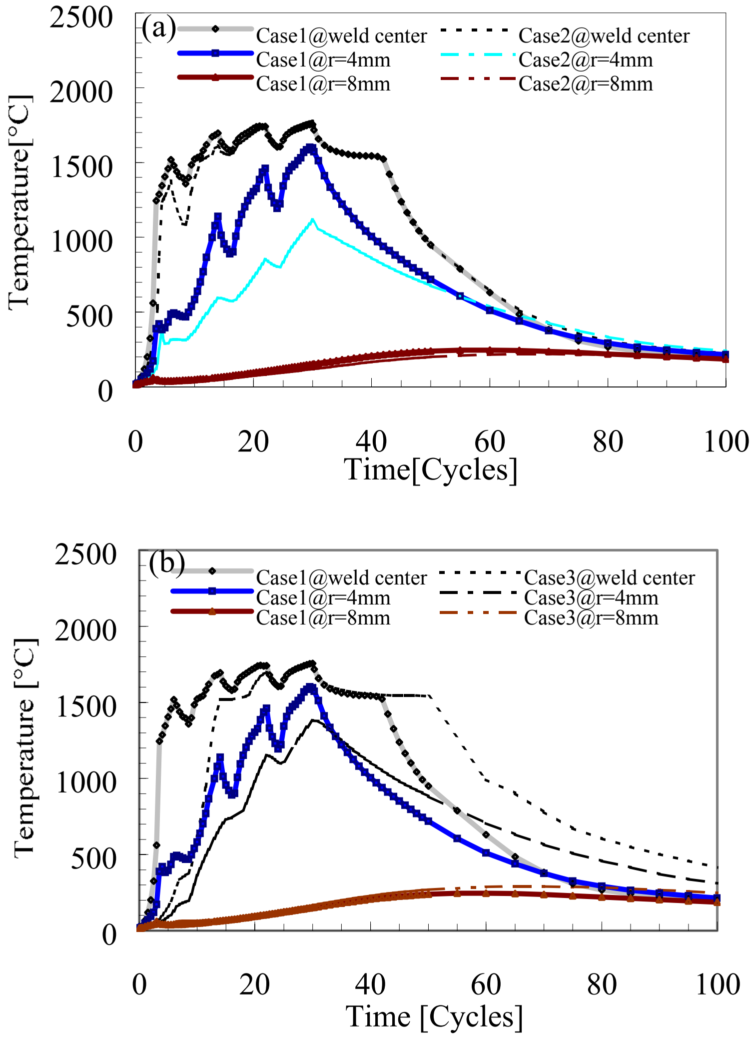

Figure 5: Influence of process characteristics on thermal history considering at the upper limit of weldability lobe

Figure 5a: Influence of electrode face diameter resulting in welding current adaptation and consequently on thermal history

Figure 5b: Thermal history in two- and three-sheet joining cases

Influence of Post-heating Current on Weld Geometries

The nugget geometries and sizes at the end of each pulse in the case of TRIP steel joining are illustrated in fig. 6. It is obvious that the nugget develops until the end of pulsed welding. The peak temperature at the weld center is found at the end of the last or the third pulse. After that, there is no significant evolution of heating rate during the post-heating stage. It is shown that there is no further development in nugget size during the application of post-heating current and this is contrast to metallurgical phase evolution in the HAZ during this supplementary stage. Let us examine a node located inside the nugget and near the fusion line, i.e. node at y=1,168mm as shown in fig. 7b. The maximum temperature of this node is about 1535°C at the end of the welding process.

The temperature drop can be also observed during the current shut-off. The thermal history of this node increases again during the post-heating stage but with a lower heating rate than that experienced in the assembly during welding. The maximum temperature of this node reaches about 1354°C at the end of post-heating stage. This reveals that the simulated nugget size at the end of post-heating will be smaller than that obtained at the end of welding. It is worth noting that the appearance of maximum nugget height and diameter is an irreversible phenomenon and only takes place at the end of welding. Therefore, this discussion can be supported by the occurrence of maximum nugget diameter at the end of welding stage with the examination of thermal history. Fig. 6d shows the simulation result of the smaller size of nugget diameter at the end of post-heating stage than that predicted at the end of welding as illustrated in fig. 6c.

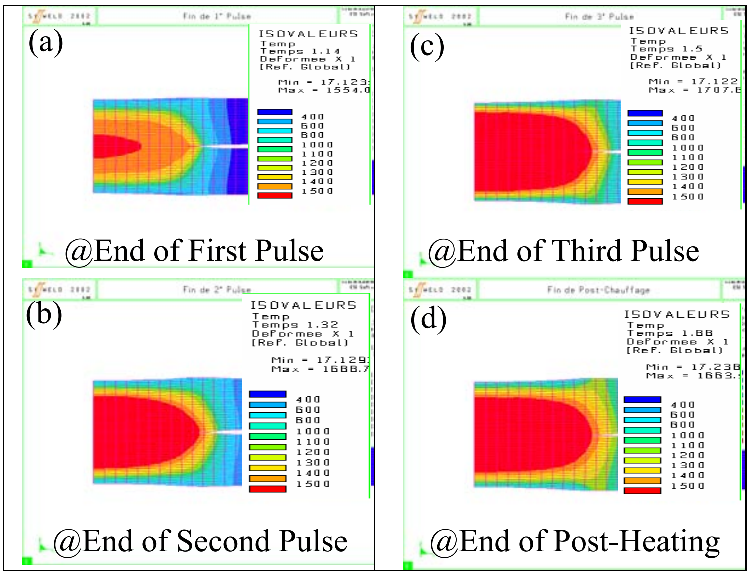

Figure 6: Predicted nugget development kinetics using post-heating current: case4

It is obvious that more important heating rates can be found for the nodes located along the axis than for the nodes located along the radius. However, the temperature history considered at the position located outside and near the HAZ zone, at the position (r = 4,50mm) as shown in fig.7, is increased even during the current shut-off. For the positions located sufficiently far away from the weld center (r=5.10 mm), the drop in their thermal histories cannot be observed and the temperature increases continuously during current shut-off and post-heating stage.

The simulation results reveal that the number of pulses and the magnitude of post-heating current should be prudently selected while practically examining the mechanical and metallurgical properties of weld.

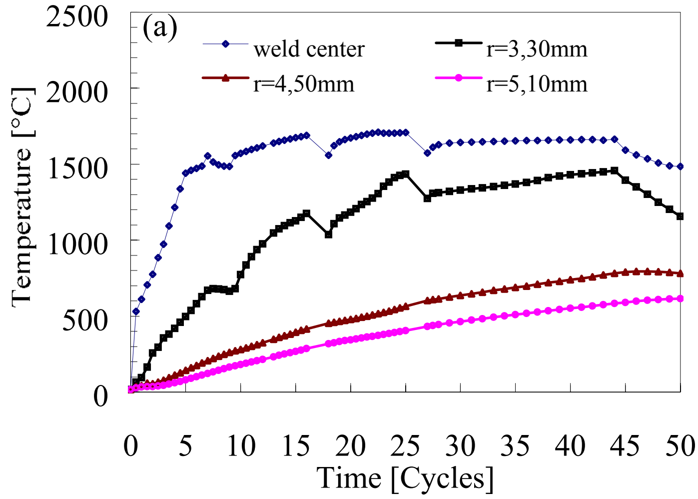

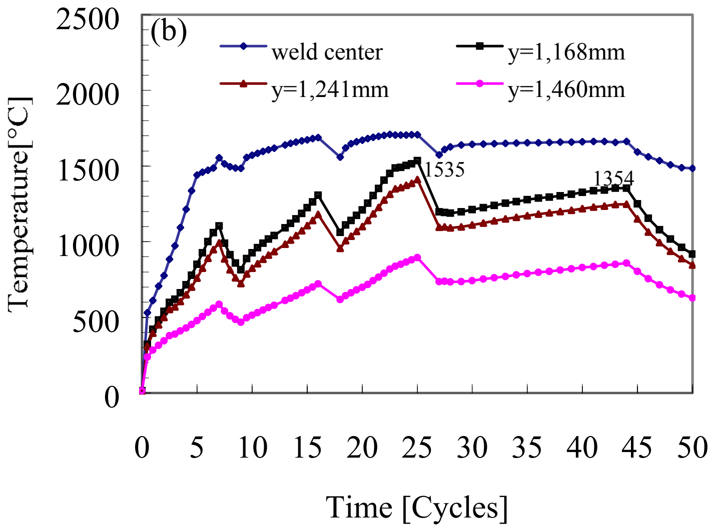

Figure 7: Influence of post-heating current on nugget size at the end of welding: case4
Figure 7a: Average thermal history at different radial position
Figure 7b: Average thermal history at different axial position

Residual Stresses in Assembly

The slide-line mechanical contact element without friction is defined at sheet-to-sheet and electrode-to-sheet interfaces throughout the computation. This contact condition however may not be a very realistic approach for the appearance of nugget at faying surface. In fact, when the nugget starts forming, the faying surface is joined by the molten mold. Therefore, the contact condition associating with the occurrence of nugget should be the sticking contact condition. The novel mechanical contact approach is under development with the modification of mechanical boundary conditions at the different stage of process.
The residual stresses for three-sheet joining case are shown in fig.8.

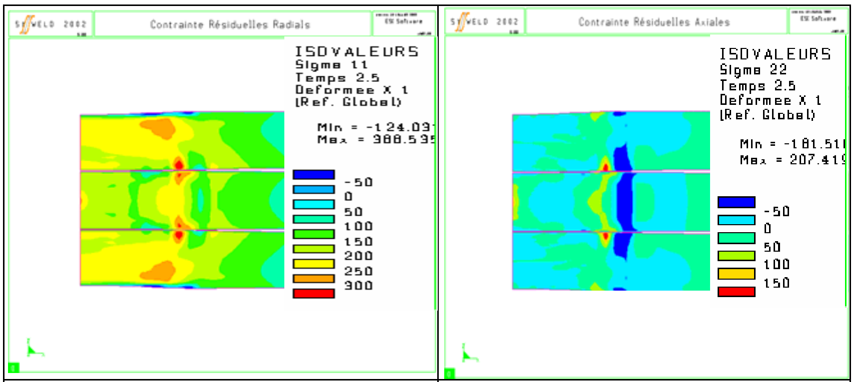

Predicted radial residual stress	Predicted axial residual stress

Figure 8: Predicted residual stresses in assembly at the end of process: case 3

EXPERIMENTAL VALIDATION

For three-sheet joining case, the validation is carried out for the quantitative measurement of nugget diameter appearing at the interfaces between the upper-to-middle and the middle-to-lower sheets, namely $D_{upper@exp}$ and $D_{lower@exp}$ respectively.

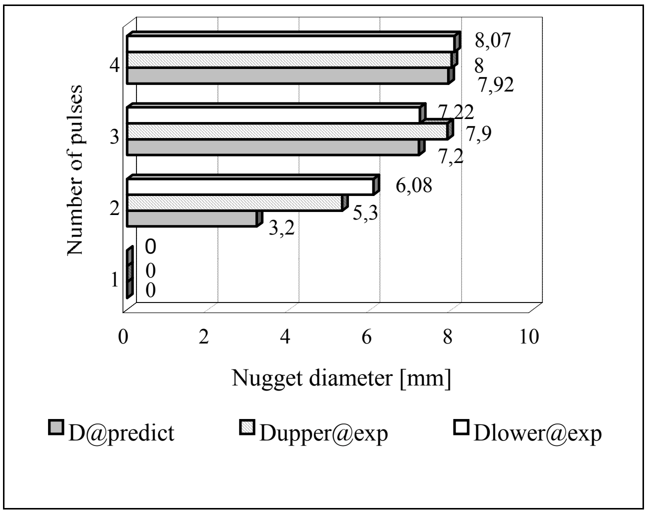

Figure 9: Validation of nugget diameter for three-sheet joining: case 3

Note that the nugget diameters increase significantly during the first two pulses and saturate for the latter stages. Both predicted and measured nugget growth kinetics exhibit similar trend for long welding time. The validation shows a quantitative agreement in nugget diameters at the end of welding, which are of 8mm corresponding to the diameter of electrode face used. However, it is found that there is a discrepancy between the measured and the predicted nugget diameter size, particularly at the end of the second pulse. The measured nugget diameters for the upper-to-middle and the middle-to-lower interfaces are around 5.30 and 6.08mm, respectively. While the simulated nugget diameter sizes are found in an order of 3.2mm and show the effect of planar symmetry as depicted in fig. 9. This discrepancy may be due to the inappropriate electro-thermal contact values at faying surface, particularly for the temperature extending from ambient temperature to 200-400°C. It is understood that the faying surface contact resistance diminishes rapidly with temperature (Ref. 9) and plays a significant role on the nugget development. These electrical contact resistances also depend strongly on the surface condition of sheet, the welding force and the temperature.

CONCLUSIONS

A finite element analysis based predictive model incorporating an electrical-thermal and thermal-mechanical coupling procedure was applied to study the heavy gauge sheet joining by the RSW technique. This model provides a better understanding of the effects of welding parameters on the nugget development kinetics and on the thermal characteristics in the assembly with the use of pulsed welding current schedules.

The main conclusions of this study are:

1) It is experimentally found that the use of the larger electrode diameter leads to an increase in the magnitude of welding current due to a better distribution of current flux and reduces the indentation of electrode face onto the sheets. Concerning three-sheet welding configuration, it well demonstrates the significance of the total bulk electrical resistance of sheet at elevated temperature with the decrease in welding current magnitude. The nugget development exhibits similar trend for long welding time.

2) The simulation results show the difference in thermal history experienced in the assembly between two- and three-sheet joining while respecting the upper limit in the weldability lobe before the occurrence of expulsion. The drop in thermal history due to current shut-off can be seen on the temperature evolution for both cases and more markedly in the two-sheet joining case. The thermal history depends strongly on the position in the assembly. For position located sufficiently far away from the nugget and the HAZ regions, there is no impact of current shut-off on the thermal history.

3) It is demonstrated that the appropriate selection of the magnitude and the number of post-heating pulses has no effect on the final nugget size obtained at the end of welding. However, the temperature history is slightly increased during the post-heating stage for every position in the assembly.

4) The validation result shows a good agreement for the final nugget size at the end of welding in the case of three-sheet joining. But the discrepancy in nugget diameter size development can be observed during the first two pulses before the saturation of nugget. This may be due to the inappropriate values of electrical contact resistances introduced at faying surface. Electrical contact resistance determination will be further conducted in order to evaluate the contact characteristics.

ACKNOWLEDGEMENTS

The authors would like to express their grateful acknowledgement to Messieurs G. RIGAUT, and J. CLAEYS, the director of the Metallurgical Development and Research Center and the head of resistance welding section, respectively, for their input during the paper preparation. Thanks also to J.P. DOUILLY, who performed all spot weld experiments in this study. The authors wish to thank C. DJENKAL and D. MALEWICZ for their educative advice during metallurgical preparation and investigation. The partial financial support of Association Nationale pour la Recherche et la Technologie (CIFRE educational program) is gratefully acknowledged.

REFERENCES

1. Peterson, W. May 15-17 2002. Methods to minimize the occurrence of interfacial fractures in HSS spot welds. Sheet metal welding conference X. Stering Heights, MI.

2. Khan, J.A.; Xu, L.; and Chao, Y.J. 1999. Prediction of nugget development during resistance spot welding using coupled thermal-electrical-mechanical model. Science and technology of welding and joining**.** Vol. 4, No.4: 201 to 207.

3. Sun, X.; and Dong, P. Aug. 2000. Analysis of aluminum resistance spot welding processes using coupled finite element procedures. Welding research supplement: 215-s to 221-s.

4. Srikunwong, C.; Dupuy, T.; and Bienvenu, Y. Nov., 2001. A decoupled electrical-thermal and mechanical model for resistance spot welding. 15th annual conference of mechanical engineering network of Thailand. Bangkok, Thailand. Vol.2: 76 to 84.

5. Murakawa, H.; Kimura, F.; and Ueda, Y. 1997. Weldability analysis of spot welding on aluminium using FEM. Mathematical modeling of weld phenomena 3: 944 to 966.

6. Thiéblemont, E. 1992. Modèlisation du soudage par points. Ph.D. dissertation**.** L'Institut National Polytechnique de Lorraine. (in French)

7. Bobadilla, M.; Niederleander, M.; Nuss, C.; Perrin, G.; and Selaries, J. Juin 1994. Données thermiques pour différentes familles d'acier. Rapport interne IRSID, Groupe Usinor. (in French)

8. Caractérisation de la soudabilité par résistance par point de produits plats revêtus ou non, Déc. 1994, Normalisation française A87-001. (in French)

9. Vogler, M.; and Sheppard, S. June 1993. Electrical contact resistance under high loads and elevated temperatures. Welding research supplement: 231-s to 238-s.

INFLUENCE OF ELECTRICAL-THERMAL PHYSICAL PROPERTIES IN RESISTANCE SPOT WELDING MODELLING

Chainarong SRIKUNWONG[†], Thomas DUPUY[††]
and Yves BIENVENU[†]

[†]*Centre des Matériaux P-M. Fourt, Ecole des Mines de Paris, F-91003, Evry cedex, France*
Phone: 33-160763035 Fax: 33-160763150
E-mail: chainarong.srikunwong@arcelor.com, Yves.Bienvenu@mat.ensmp.fr
[††]*CRDM, Arcelor, F-59381, Dunkerque cedex 1, France*
Phone: 33-328293387 Fax: 33-328296429
E-mail: thomas.dupuy@arcelor.com

ABSTRACT

2-D axisymmetric finite element prediction models incorporating electrical-thermal and thermal-mechanical coupling approach are presented. The aim is to investigate not only the influence of electrical-thermal material properties but also the impact of electrical-thermal contact characteristics on the weld geometry. The commercial finite element code Sysweld™ was utilised for these simulation purposes. The temperature dependency of the properties of both sheets and electrodes were taken into account throughout the simulation process. The implementation of electrical-thermal and thermal-mechanical coupling procedure is an important feature in order to efficiently capture the effect of contact size variation and achieve a more realistic prediction model. The macro-graphic validation of nugget development was carried out for two-sheet as well as three-sheet joining with medium frequency direct current. The thermal history, stresses and deformations experiencing in the assembly were reviewed. The comparison between computed and experimental results showed a quantitative agreement at the end of welding in two-sheet joining case. A validation between predicted thermal history and that measured by the micro-thermocouples embedded in the electrodes was also made.

The comparison between simulation and experimental results was discussed with particular regard to the impact of the electrical-thermal contact characteristics on the weld nugget and the heat-affected zone (HAZ) geometry.

1. INTRODUCTION

Resistance spot welding (RSW) is widely used as a joining technique for automobile structure due to flexibility, robustness and high-speed of process combining with very high quality joints at very low cost. Because of these process advantages and joining performances, a continuous effort in both computational procedure and modelling development for RSW process simulation has being undertaken since the last decades. Both decoupling and coupling procedure techniques have been implemented for RSW modelling. The implementation of the decoupling procedure has the advantages in the reduction of the computation cost as well as the simplification of the computation schemes. However, this computational approach suffers from a limitation to the use of flat-face electrode application since there is an insignificant variation of the contact size during the welding process. The electrical-thermal contact size computed by the mechanical module at the end of squeezing stage can be maintained throughout the simulation and results in a good agreement with the experience for the final nugget and the HAZ geometry.

Considering the process modelling with curved-face electrode application, it is disclosed that there is a significant change in the contact radii between electrode-to-sheet and sheet-to-sheet interfaces during welding stage. As a result, this manifestation has a great impact on thermal history, nugget formation and thermal induced stresses in the assembly. The implementation of the coupling procedure between electrical-thermal and thermal-mechanical modules is therefore vital in order to capture this physical interaction and produce a more realistic predictive model by updating the electrical-thermal contact size from the mechanical computation. The recent development of the coupling procedure not only takes into account the variation of contact size but also suits a larger variety of electrodes used. Examples of these advanced RSW computation techniques can be found in the literature[1-4].

Unlike the metal forming process, the RSW or other welding techniques are commonly performed at elevated temperature beyond the fusion state of material. The necessary thermo-physical database for such welding simulation is limited, when available. Consequently, most of the beginner researchers are firstly confronted by the cumbersome tasks to make a sort of judgment about the simplification degree of the model and the influence of this estimated information on the computation results.

Concerning the investigation of the impact of the thermal parameter inputs on the weld pool modelling, Mundra *et al*[5]. investigated the impact of thermo-physical properties in laser beam spot welding by using a finite difference model. It was revealed that the temperature dependency of the thermal conductivity and the surface tension is very important for a good assessment of the predicted weld pool characteristics. More recently, a systematic validation procedure applied for a case study of CO_2 laser beam weld modelling was proposed by Sudnik *et al.*[6] The impact of the thermo-physical inputs on the weld pool characteristics was also included in this study. It underlined the significance of the thermal physical properties at elevated temperature, especially the influence of the enthalpy on both depth and width of the fusion zone.

Some authors[1-4] have studied and numerically simulated the RSW process with the coupling computational procedure. The material temperature dependency was also taken into account throughout their studies. The contact size variation and pressure, the residual stresses and deformations, and the nugget development kinetics were reported for both flat- and curved-face electrode applications. However, the comprehensive study of the electrical-thermal database influencing on the electrical-thermal behaviour with the coupling approach has not been well addressed, yet.

In the present study, the experimental observation will be firstly discussed with the regard to practical welding schedules. The comparison of the nugget formation kinetics with the use of a single pulse and of multi-pulse welding schedule will be presented. The impact of the variation in electrical-thermal physical properties of material will be then studied and the validation will be centred on the nugget size. A validation of the nugget and the HAZ sizes and geometries with the application of pulsed welding current in the case of heavy gauge sheet joining will be investigated.

A comparison between the thermal history measurement by the embedded micro-thermocouple and the predicted thermal history is presented for a case study of thin gauge sheet joining.

2. EXPERIMENTAL PROCEDURES

In this study, the magnitudes of welding force and time are retained at the upper limit of welding lobe in line with common practice. Two sheet grades of ARCELOR are used; non-coated deep-drawing quality low carbon steel, namely IF and Al-killed (ES) steel grades. The mechanical and electrical/thermal properties and the chemical composition of both grades are given in Refs. 7 and 8. The macro-metallurgical observation is conducted for the kinetics development of the nugget.

According to welding standard, the medium frequency direct current (MF-DC) with ten welding cycles is considered for the welding experiment of thin gauge sheet joining. In the case of the heavy gauge sheet joining, four-pulsed current is applied for the welding operation. Two different types of electrode profile are used for thin gauge sheet joining while respecting the electrode face diameter of 6-mm. The electrode profiles, namely TH6 and TP6 are used. The TH6 is the curved-face of 6-mm diameter electrode corresponding to ISO5821 type G. The TP6 type of CRDM is the cone electrode of 6-mm diameter and flat-face profile.

According to welding standard guidelines with the use of pulsed current for joining stack-up or heavy gauge sheets, an example of the welding schedule $11{,}2kA \times 4(6+2)$ indicates that pulsed current with effective magnitude of 11,2 kA is applied for 4 pulses, each pulse has 6 cycles of welding plus 2 cycles of current shut-off. The use of pulsed welding offers some advantages in heavy gauge sheet joining including the stability of nugget development characteristics and the reduction of electrode wear. However, such welding application leads to longer time of the process. The curved-face electrode with the diameter of 8 mm, namely TH8, is used for joining the heavy gauge and stack-up sheets of 2-mm thickness.

The as-received sheets are cut to 50×50-mm coupons. The electrode conditioning prior to welding is performed for 50 welding points with bare sheet. The trial welding tests are then conducted in order to determine the expulsion limit. These trial welding conditions are based on the French welding standard guideline[9], which allows determining the appropriate welding schedules. The welding schedules, just below the expulsion limit, are performed for three welding coupons and for each two cycles or 0,04 seconds to examine the nugget development. This is the case of welding with ten cycles of a single pulse schedule for thin gauge sheet joining.

To study the nugget formation of the heavy gauge sheet joining with four-pulsed welding current, it is more convenient to interrupt the welding at the end of each pulse for the macrographic observation instead of observing nugget development at the end of each two-cycle welding as in the previous case.

The no-expulsion welding can be verified from the force and the displacement signal monitored with the LABVIEW® window. The effective current magnitude is obtained from the MIYASHI® current signal checker. Nugget development kinetics can be further examined by sectioning the spot after each interrupted cycles or pulses. The polished axial sections of spot welded samples are etched with picric acid to examine the fusion line or the nugget contour. Quantitative macro-photographic measurements are further undertaken for the nugget size.

3. EXPERIMENTAL RESULTS AND DISCUSSION

INFLUENCE OF PROCESS CHARACTERISTICS ON NUGGET FORMATION

Some examples of the nugget development kinetics for 0,8mm-thick IF steel sheet with the different electrode types used are reviewed in Fig. 1. This demonstration is to provide the first global insight for the nugget development in the case of thin gauge sheet joining. As expected, the increase of the welding time results in both nugget size and penetration development. Planar symmetrical nuggets can be observed at the end of welding. The use of different electrode types also manifests differently in nugget formation kinetics, especially at the early stage of welding.

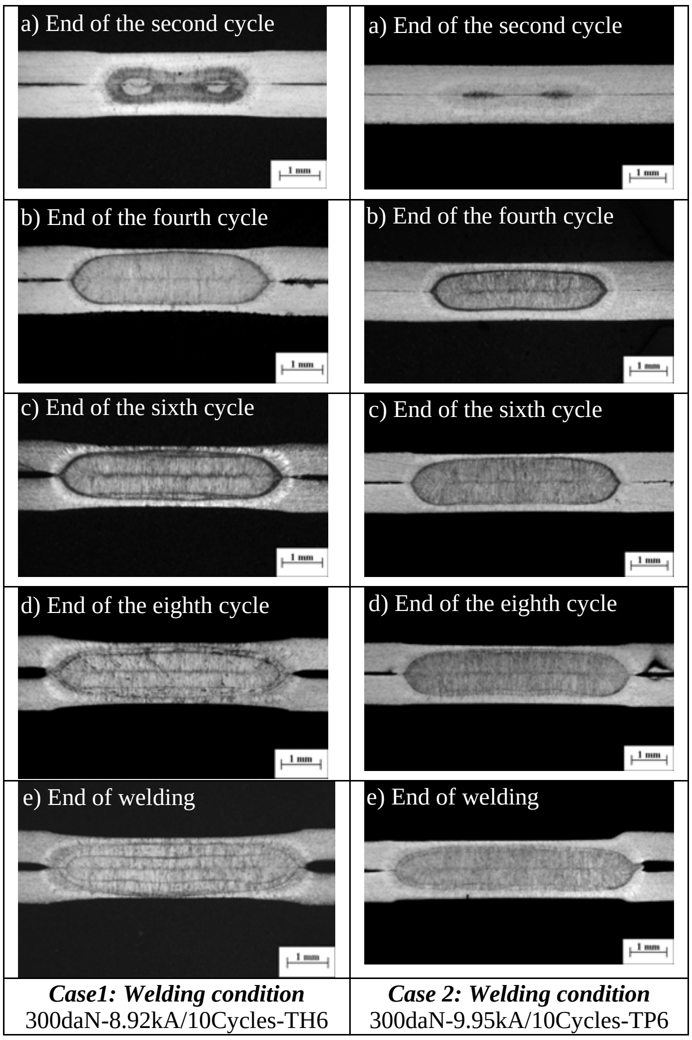

Fig. 1: Comparison of nugget formation kinetics of 0,8-mm thick IF steel interrupted after 2, 4, 6, 8 and 10 cycles with MF-DC welding current

Using flat-face electrode profile shows a trend of increasing the current magnitude. The early toroidal hot zone bonding at the faying surface can be observed at the end of the second cycle as illustrated in the case of the electrode TH6. This early bond is also visible for the electrode TP6 application. It is pointed out here that the electrode tip profile governs the contact size variation between the interfaces and as a result the difference in welding current magnitude. To simulate the influence of the contact size variation mechanism, the coupling computation procedure is vital to be implemented. The selection of electrode type can be considered as a key factor influencing directly the welding lobe determination.

For the heavy gauge sheet joining, the nugget development kinetics at the end of each pulse for two and three 2mm-thick sheet of ES steel grade is shown in Fig. 2. Similarly to the thin gauge sheet joining case, both height and diameter of the nugget develop progressively until the end of welding. The experimental nugget diameter size is 8.75 mm. for the case 3.

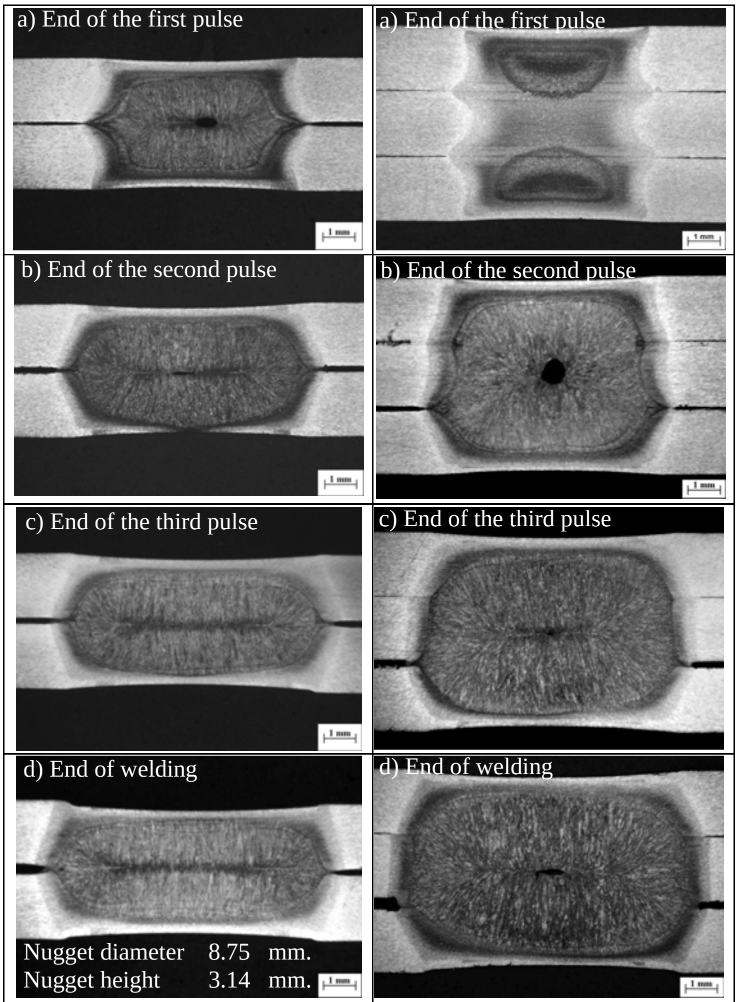

Case 3: Welding condition 400daN-11.2kA/4(6+2)-TH8	***Case 4: Welding condition*** 450daN-10.6kA/4(6+2)-TH8

Fig. 2: Illustration of nugget formation of two- and three-sheet assembly of 2-mm thick ES steel at the end of each pulse

In case 4, instead of initiating at the interfaces of the assembly, the hot zone originates in the superior and inferior regions at the end of the first pulse but the nugget does not start forming yet. For the latter pulses, nugget penetration and development also show a trend similar to that of two-sheet assembly case. The asymmetry in the upper and the lower nugget diameters can be found before the saturation of nugget diameter at the end of the fourth pulse. According to the practical welding, either symmetrical or asymmetrical nugget development can be observed.

In the present study, the impact due to the electrical-thermal property variability on the simulated results is studied for the case 3 (the joining 2mm-thick ES steel sheet with the TH8 electrode).

4. COMPUTATIONAL PROCEDURES

The features of the coupling procedures can be described by loop sequential computational procedures of the nodal temperatures transferred from the electrical-thermal analysis to the thermal-mechanical analysis in order to compute the thermal stresses and assembly distortions. On the other hand, the stress and the assembly deformation distributions are then transferred back to the next time-step of electrical-thermal computation in order to update the variation of the assembly deformation and pressure. The computation scheme is schematised in Fig. 3.

5. FORMULATION FOR MODELLING

5.1 STRUCTURE MODELLING

A representative assembly of electrode and sheet utilised for analysis as shown in Fig. 4 illustrates a half axisymmetric finite element model for electrode and sheet assembly, which is considered for both electrical-thermal and thermal-mechanical analyses. 2-D axisymmetric structural models of two- and three-sheet joining with the application of the curved-face electrode of 6mm and 8mm-dia. are constructed. Both electrical-thermal and mechanical contact elements are defined at electrode-to-sheet and sheet-to-sheet interfaces.

5.2 ELECTRICAL-THERMAL MODELLING

RSW process is a resistance welding process governed by Joule heating effect with a concentration of the heat generation at the interface between two solid bodies in contact during current flow. This heat further propagates into these bodies by conduction mode associated with the imposed thermal boundary conditions. Thermal and electro-kinetic governing system equations are presented in (1) and (2), respectively:

$$\rho\frac{\partial H}{\partial t} - div(K.\mathbf{grad}T) - \mathbf{gradV}.\sigma.\mathbf{gradV} - Q = 0 \tag{1}$$

$$div(\sigma.\mathbf{gradV}) = 0 \tag{2}$$

Where T, V are the temperature and the scalar electrical potential, respectively. $\rho(T), K(T)$ and $\sigma(T)$ represent the density, the thermal conductivity and the electrical conductivity of the medium which are temperature dependency characteristics. $H(T)$ is the enthalpy described as a temperature dependent function.

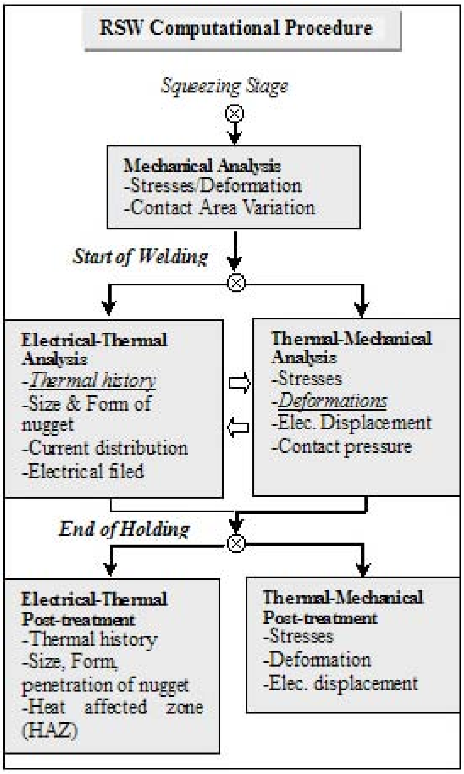

Fig. 3: Schematic illustration of computational procedure

5.3 THERMAL-MECHANICAL MODELLING

The electrode force is modelled from the experimental welding force signal by assuming a uniform pressure distribution across the annular end of the upper electrode. The vertical nodal displacement of the annular end of the lower electrode is constrained corresponding to the welding operation with the pedestal welding machine. Other constrain boundary conditions are imposed at the nodes locating along the y-axis corresponding the axisymmetric model. An elasto-plastic law without deformation rate dependency is defined for the mechanical characteristics of sheet. Temperature dependency of sheet properties, mechanical contact characteristics and the transient computational approach are included in the computation. The sliding contact model without friction is defined for the contact surface. The fundamental mathematic formulation of the axisymetric RSW modelling in cylindrical coordinate system is described elsewhere[10].

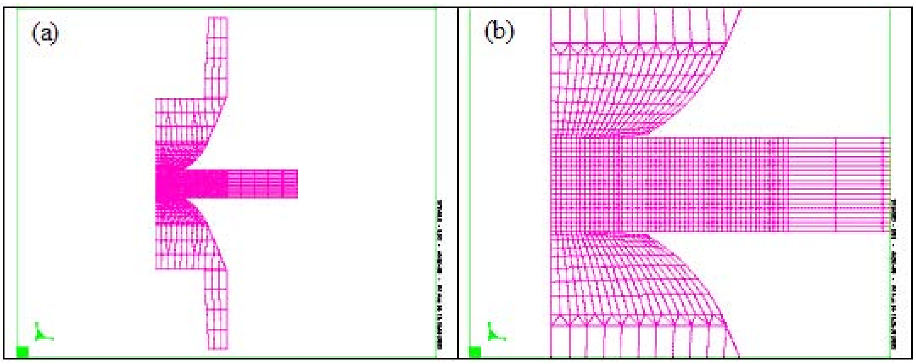

Fig. 4: Illustration of structure mesh models used in FE analysis; (a) mesh construction of two-sheet assembly with the use of curved-face electrode of 8mm-dia. (b) increasing the number of elements in the high thermal, stress and deformation gradient regions

6. STUDY OF ELECTRICAL-THERMAL DATA VARIABILITY

6.1 VARIABILITY OF PHYSICAL PROPERTIES

The variability in electrical/thermal physical properties of the steel material is shown in Fig. 5. Variability in the electrical/thermal material database of $\pm 5\%$ and that of the contact resistance of $\pm 5\%$ and $\pm 20\%$ are considered. The thermal conductivity of steel depends strongly on temperature and decreases gradually with increasing temperature until the Curie temperature (769°C) and increases again with temperature. Two extrapolation techniques representing the linear extrapolation and the increase of the thermal conductivity above melting temperature of the sheet material are investigated. To compensate the convection effect in the nugget, the significant increase of the thermal conductivity above melting state is introduced to the reference model.

The similar estimation technique of the isotropic thermal conductivity characteristic at elevated temperature for the weld modelling can be found in the literature[11-13]. Additionally, Alcini[14] measured the thermal distribution in the weld nugget of AISI1008 steel sheet joining and it was found that the highest temperature at the weld centre is approximately 1650°C. He also reported that the temperature is possibly uniform in the nugget.

The enthalpy of sheet determined from the integration of specific heat of the ThermoCalc® calculation is introduced as the input and the variation of the enthalpy at elevated temperature is linearly extrapolated throughout this study.

For the RSW process simulation, the other significant input is the contact characteristic of both electrode-to-sheet and sheet-to-sheet interfaces. The global dynamic resistance of the assembly can be commonly monitored as a function of time. However, it is not an easy task to decompose this global dynamic resistance of the assembly into individual resistance component including contact resistances and correlate the contact resistances with the corresponding interface temperature. To investigate the impact of the contact uncertainty on the nugget and HAZ development, the variation of $\pm 20\%$ is considered as the extreme or bounded uncertainty values. The contact resistances introduced to the finite element model are user's defined functions which are pressure/temperature dependent.

The measurement of the electrical contact resistance at different conditions of contact pressure and temperature was conducted and reported by Vogler *et al.*[15]. It was found that the contact resistance depends strongly on the contact surface hardness, temperature, and loading pressure. Recently, an empirical mathematical model described as a pressure/temperature dependent function is proposed in the literature[16].

In this study, measured electrical contact resistances[8] are introduced to the electrical-thermal model. To take into account the hysteresis characteristics of the contact resistance due to contact temperature evolution, this temperature-dependent electrical contact function depends on the highest temperature experiencing at the interface.

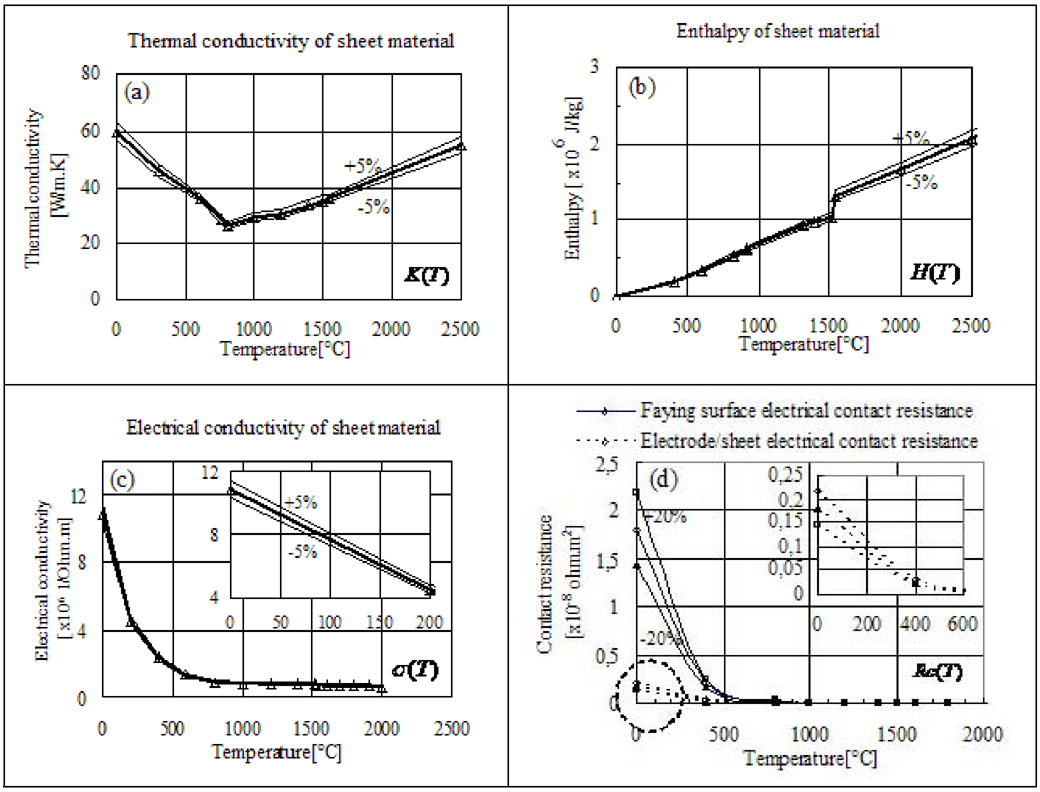

Fig. 5: Variability of electrical-thermal properties of sheet; (a) thermal conductivity extrapolated linearly after the fusion with variation of $\pm 5\%$, (b) enthalpy with variation of $\pm 5\%$, (c) electrical conductivity with variation of $\pm 5\%$, (d) electrical contact resistance with variations of $\pm 5\%$ and $\pm 20\%$ (the variation of $\pm 5\%$ is not displayed in Fig. 5d)

According to literature[8,15,16], it is believed that the contact resistance drops abruptly with the temperature and shows an insignificant change at elevated temperature as shown in Fig. 5d. We consider the degree of variation for contact resistance more significant than other thermal properties because it is widely agreed that it has a strong impact on the nugget and HAZ development. The comparison of the electrical/thermal material property influence will be discussed on the thermal history at weld centre and further centred on the nugget and HAZ size and geometry.

6.2 RESULTS AND DISCUSSION

The comparison of the nugget geometry and thermal history can be seen in Fig. 6. Two extrapolation techniques representing the linear extrapolation and the increase of the thermal conductivity after the fusion state of the sheet material are investigated. It is found that the linear extrapolation method results in higher thermal history evolution. The highest temperature found at the end of welding is 2308°C. However, the predicted highest temperature found at the weld centre seems to be very high and unreasonable.

The significant increase of the thermal conductivity at elevated temperature results in both larger nugget diameter and penetration height. The method used for the thermal conductivity evaluation plays a marked influence on the nugget penetration as demonstrated in Fig. 6a. However, the comparison of the isothermal contours defined for the HAZ in the radial direction displays a slight difference. Generally for the RSW thermal simulation, more important thermal gradient can be observed in the axial direction of the assembly as seen in Fig. 6a. Temperature drop due to current shut-off can be visible on the thermal history curves.

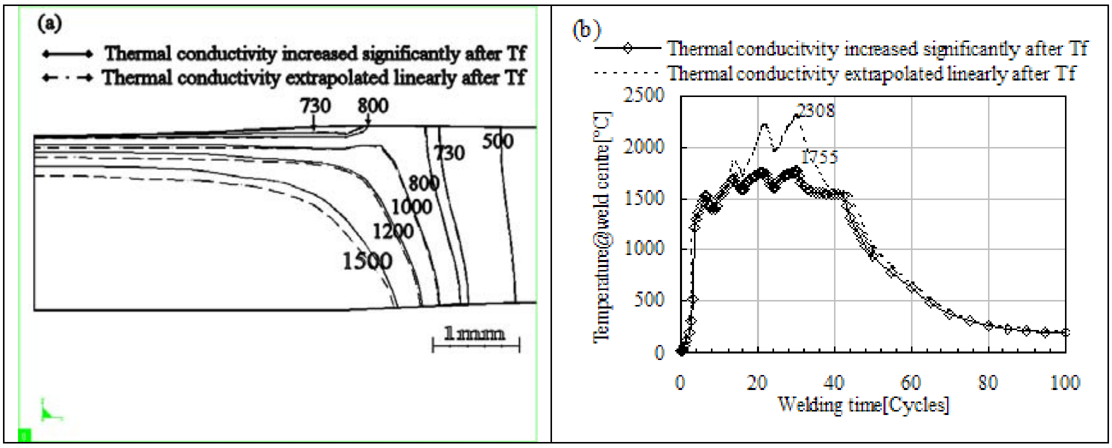

Fig. 6: Comparison of two techniques used for thermal conductivity estimation at elevated temperature; (a) comparison for nugget and HAZ geometry, (b) comparison for thermal history

It is well demonstrated for the impact of the thermal conductivity variation that the decrease of thermal conductivity results in larger both predicted nugget and HAZ geometry at the end of welding and higher the weld centre temperature as seen in Fig. 7.

Generally, the linear extrapolation technique for enthalpy evaluation at elevated temperature is widely used for weld simulation and therefore this technique is employed throughout the input variation impact investigation. Thermal history and nugget geometry resulting from the enthalpy variation show a trend similar to those of thermal conductivity as depicted in Fig. 8. A similar impact of the enthalpy on fusion zone geometry was also reported in Ref.6. Note that the enthalpy variation plays more significant role on the HAZ geometry than that of thermal conductivity as shown in Fig. 8a. To study the effects of electrical/thermal input variation and provide a physical meaning for their impacts on the HAZ geometry, the HAZ diameter is defined by the isothermal contour of 730°C.

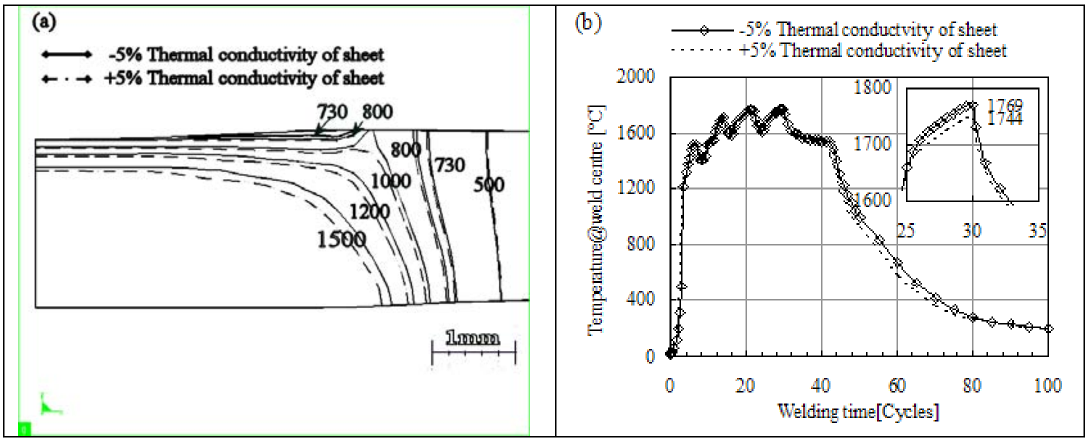

Fig. 7: Comparison of electrical-thermal computation results with $\pm 5\%$ variation in thermal conductivity (Thermal conductivity increased significantly above melting temperature); (a) nugget and HAZ geometry comparison, (b) comparison of thermal history experiencing at weld centre

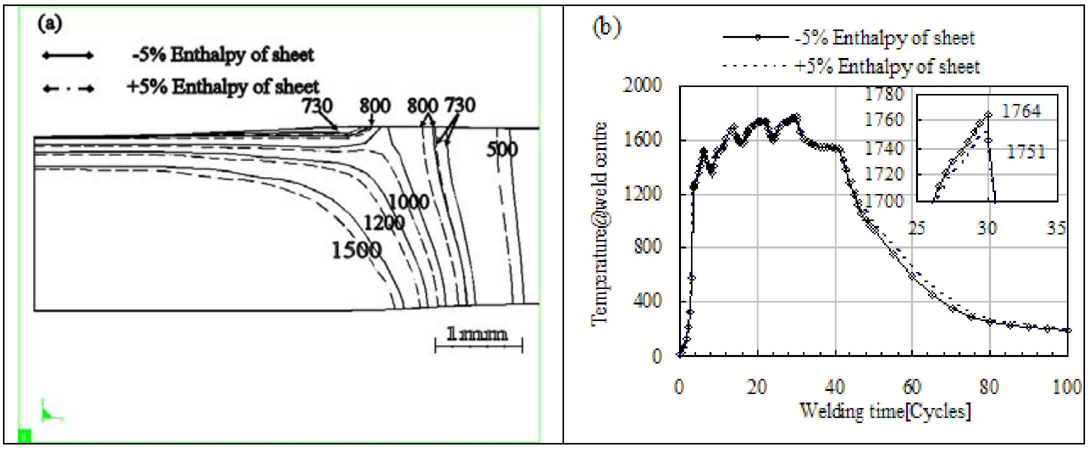

Fig. 8: Impact on the simulation results with $\pm 5\%$ variation of the sheet enthalpy;
(a) comparison of nugget and HAZ geometry, (b) comparison of predicted thermal history of the weld centre.

According to electrical-thermal model of the RSW process, other significant material property is the electrical conductivity of the sheet; the inverse of which represents a contribution to the electrical resistivity of the assembly. This sheet property is generally known as the temperature and carbon content dependency.

As expected, the simulation results reveal larger nugget size and penetration height with the decrease of the sheet electrical conductivity as depicted in Fig. 9. It can be seen that the electrical conductivity of sheet influences strongly not only the nugget but also the HAZ geometry. Decreasing electrical conductivity, or on the other hand increasing bulk resistivity, results in the weld geometry enlargement.

In contrast to the evolution of bulk resistivity with temperature, the contact resistance value is higher at low temperature and pressure. With the increase of temperature in the assembly during welding process, the contact resistance diminishes rapidly. The bulk resistivity thus dominates the nugget development for the latter stages and until the end of welding.

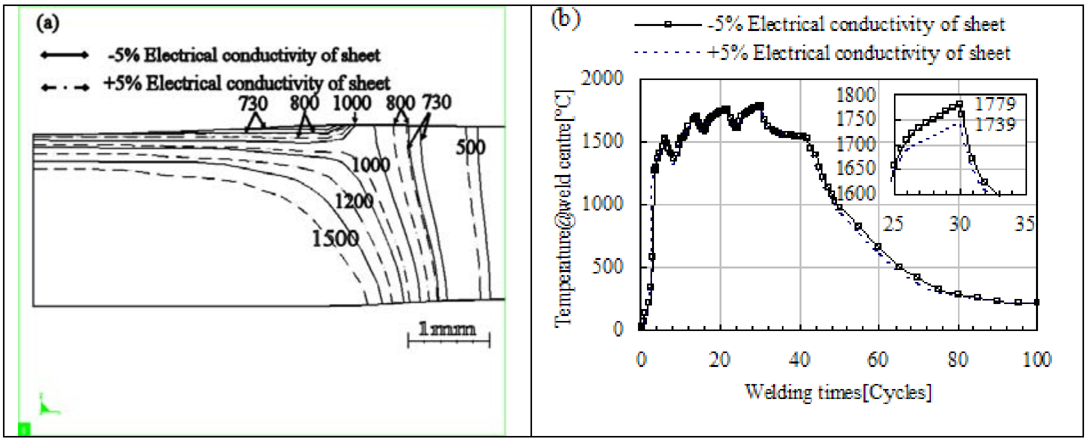

Fig. 9: Effect of $\pm 5\%$ variation of electrical conductivity on simulation results; (a) comparison of nugget and HAZ geometry, (b) comparison of thermal cycles experiencing at weld centre

According to these basic features of the RSW process characteristics, it is necessary to conduct a chronological study for the weld geometry development at each stage. The weld geometry comparison at the end of welding alone cannot be considered as strong evidence to reveal the impact of contact resistance variation. To take into account the contact resistance uncertainty, $\pm 5\%$ and $\pm 20\%$ variation are compared and examined for the influence of faying and electrode-to-sheet contact resistances on weld geometry.

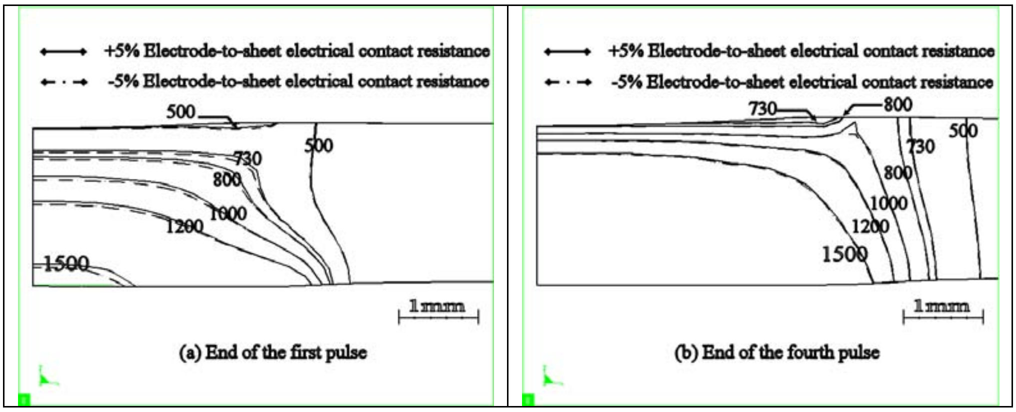

Fig. 10: Effect of ±5% variation of electrode-to-sheet electrical contact resistance;
(a) comparison in nugget and HAZ development at the end of the first pulse, and (b) at the end of welding

The electrode-to-sheet contact resistance with ±5% and ±20% uncertainties influencing weld geometry variation at the end of the first pulse and the end of welding is demonstrated in Figs. 10 and 11, respectively. It is disclosed that there is a slight impact of electrode-to-sheet contact resistance on the final nugget diameter size. With the increase of the contact resistance uncertainty, the impact on the nugget diameter and HAZ size variation becomes more obvious. The effect of the electrode-to-sheet at the early stage of welding can be observed as displayed in Fig. 10a. The comparison of temperature profiles along the electrode face corresponding to the end of each pulse can be seen in Fig. 11b.

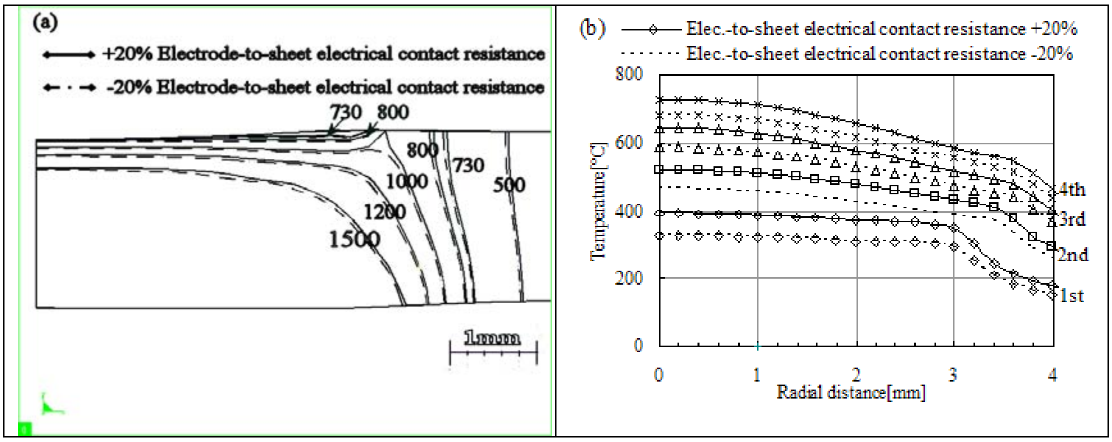

Fig. 11: Impact of ±20% variation of electrode-to-sheet electrical contact resistance on the simulation results; (a) comparison of nugget and HAZ geometry at the end of welding, and (b) thermal cycles along the electrode face at the end of each pulse

The influence of the sheet-to-sheet electrical contact resistance on the nugget and HAZ development can be compared in Figs. 12 and 13 for ±5% and ±20% variation, respectively. It is found that the increase in faying surface contact resistance results in larger nugget diameter and consequently on the HAZ enlargement. No significant penetration variation is observed among these uncertainty contact resistance values.

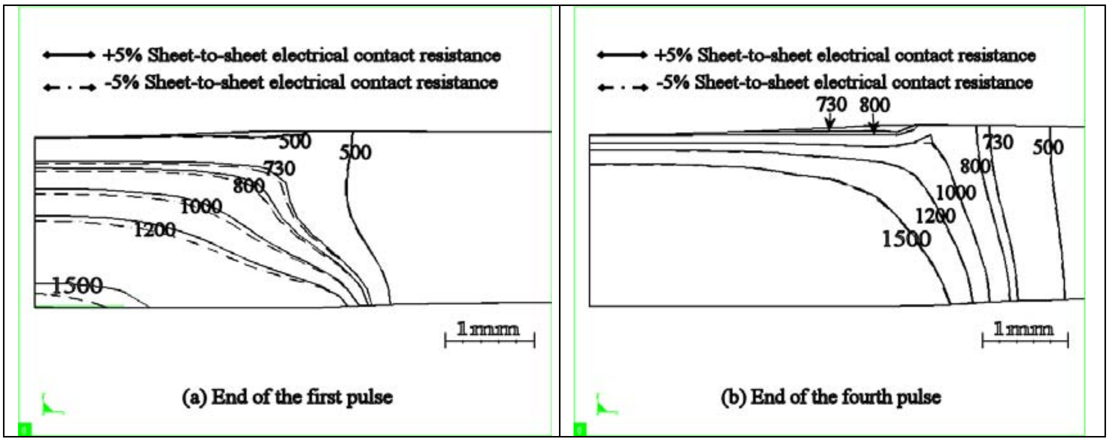

Fig. 12: Impact of $\pm 5\%$ variation of sheet-to-sheet electrical contact resistance on the simulation results; (a) comparison of nugget and HAZ geometry at the end of the first, and (b) at the end of welding

The simulation results reveal the influence of the faying surface contact resistance on nugget development, especially at the early pulse. The dominant role of faying surface contact resistance on weld nugget and the HAZ can be seen in Fig. 13a: the nugget was already appeared at the end of the first pulse with $+20\%$ variation of contact resistance. The comparison of nugget diameter and penetration height shows a similar trend for the latter pulse and there is no significant scattering in nugget diameter size and penetration height at the end of welding. The increase of faying surface contact resistance leads to enlarge both nugget diameter and HAZ size in comparing Figs. 12b and 13d.

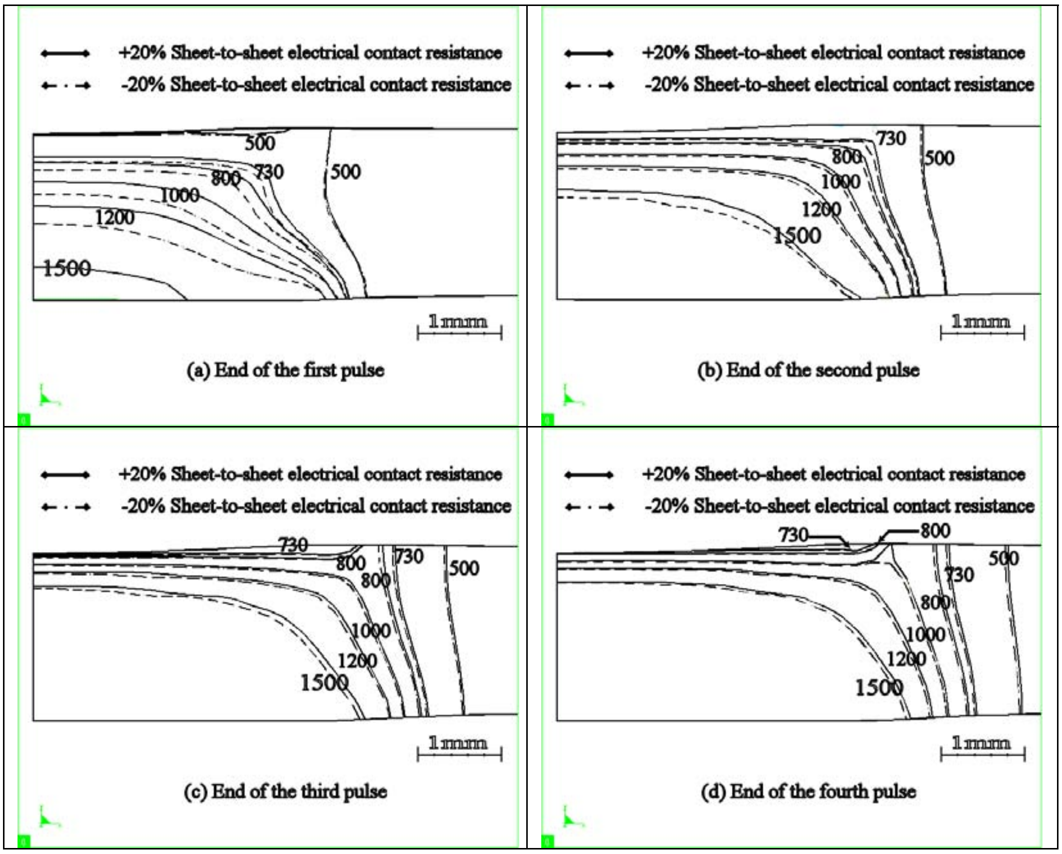

Fig. 13: Nugget formation kinetics comparison for the case of $\pm 20\%$ variation of sheet-to-sheet interface electrical contact resistance; (a) at the end of the first pulse, (b) at the end of the second pulse, (c) at the end of the third pulse, and (d) at the end of welding

The summarised detail of thermal/electrical property variation influencing weld geometry is concluded and shown in Fig. 14. It is disclosed that the sheet electrical conductivity is the most significant input influencing on the weld geometry among other thermal parameters. The decrease in thermal conductivity, enthalpy or electrical conductivity results in the enlargement of the weld geometry. Increasing contact resistance also results in larger final nugget and HAZ geometry, but less significant influence comparing to those of other thermal parameters. The contact resistance with the temperature plays a great role on the weld geometry development as demonstrated in Fig. 13, particularly at the early welding stage.

Additionally, the sensibility of the predicted final nugget and HAZ diameter sizes due to the electrical/thermal property variability shows a similar tendency as shown in Figs. 14a and 14c.

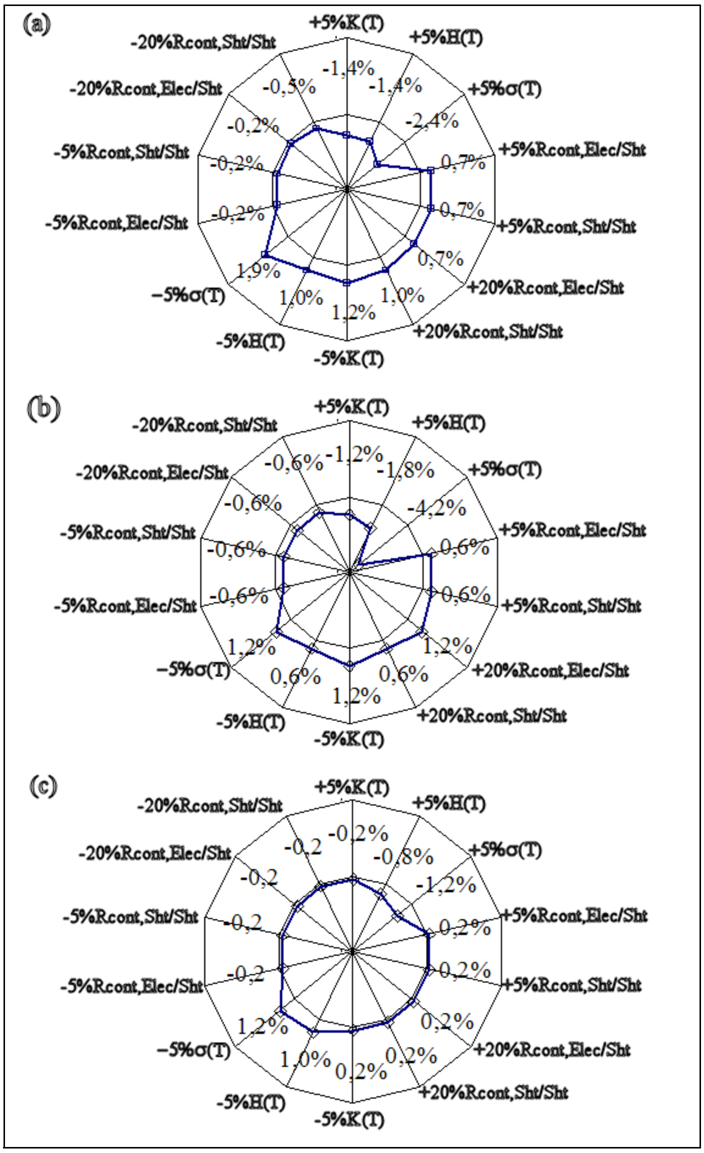

Fig. 14: Comparison of the relative variations in nugget and HAZ geometry at the end of welding due to $\pm 5\%$ variation of thermal-electrical properties; (a) relative final nugget diameter size (b) relative final penetration height, and (c) relative final HAZ diameter measured at the faying surface

7. VALIDATION OF THERMAL RESULTS AND DISCUSSION

7.1 NUGGET FORMATION KINETICS VALIDATION

The nugget development kinetics validation at the end of each pulse can be seen in Fig. 15 for the case of two-sheet joining with TH8 electrode. The comparison of the nugget between prediction and the experimental observation shows a qualitative agreement at the end of welding. The comparison of the final nugget diameter size and penetration height can be seen in Fig. 15d.

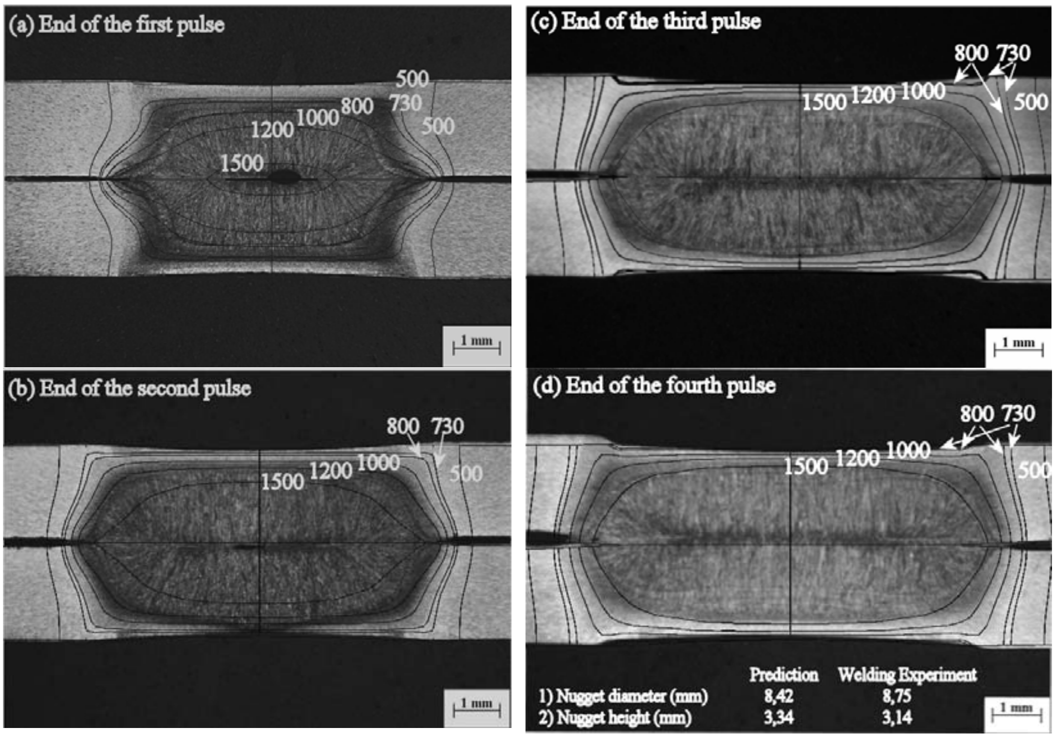

Fig. 15: Validation of nugget formation kinetics at each pulse for two-sheet joining
(Welding schedule 400daN-11.2kA/4(6+2)-TH8; Sheet material@2mm-thick ES grade);
(a) at the end of the first pulse, (b) at the end of the second pulse, (c) at the end of the third pulse, and (d) at the end of welding

However, there is a discrepancy in the nugget size and form at the beginning of welding, particularly at the end of the first and second pulses. This may be due to the variation of the measured electrical contact resistance at low temperature and pressure as early statement. A special attention should be paid to the measurement of electrical contact resistance at low temperature and pressure.

The final nugget size validation of three-sheet joining with TH8 electrode can be found in Fig. 16. In this case, the predicted results are similar to those shown in the case of two-sheet joining; the simulated final nugget size is slightly smaller than that obtained from the welding experiment.

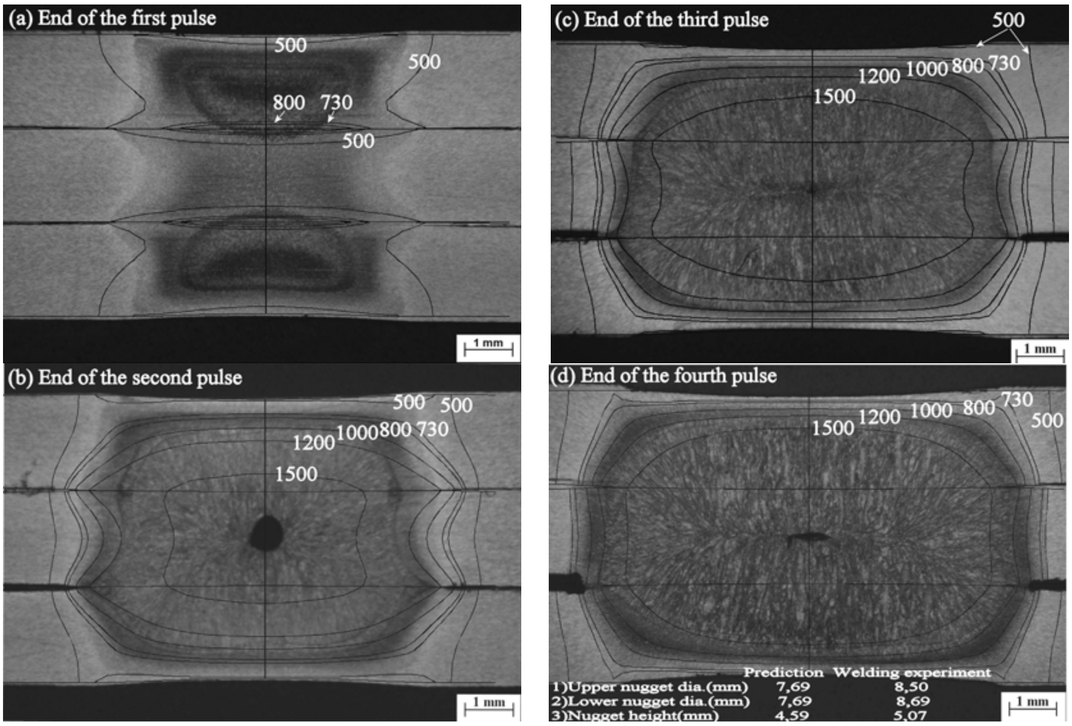

Fig. 16: Validation of the final nugget geometry for three-sheet joining
(Welding schedule 450daN-10.6kA/4(6+2)-TH8; Sheet material@2mm-thick ES grade);
(a) at the end of the first pulse, (b) at the end of the second pulse, (c) at the end of the third pulse, and (d) at the end of welding

7.2 THERMAL HISTORY MEASUREMENT AND VALIDATION

To validate the thermal history of the RSW process, two micro-thermocouples are embedded in the lower electrode. The thermocouple installation positions are 0,398 and 1,403 mm away from the electrode face. The thermal history measurements are carried out for ten welding spots and the measured thermal cycles are then averaged for each local position.

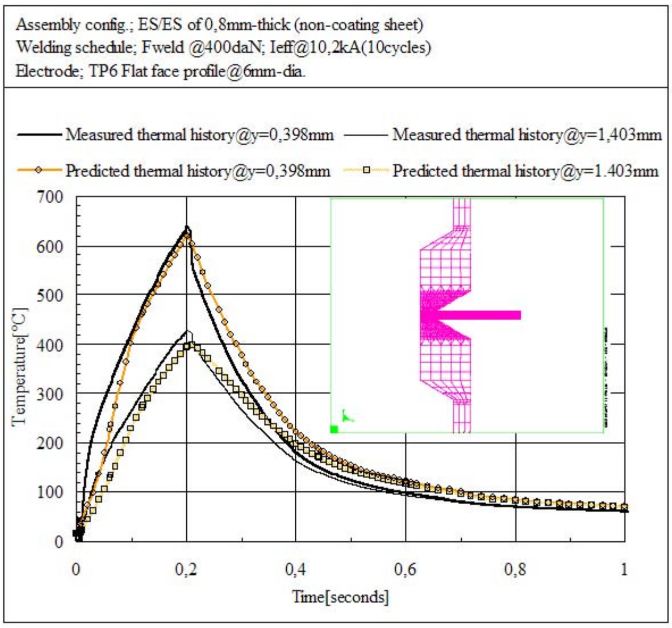

Fig. 17: Validation of thermal history experiencing at different positions in the lower electrode

Several numbers of welding operation and thermal cycle measurements help assuring the reproductive and comparative results. The experimental procedures can be found in Ref. 17. The welding condition and the sheet material used are given in Fig. 17. A single pulse schedule of ten welding cycles is applied for this joining case. The predicted thermal history shows a good qualitative agreement with the experience for both heating and cooling stages of the process. Higher heating rate is found for the position locating near to the electrode face. A slight discrepancy of the heating and cooling rates at the early stage of welding can be observed in the validated results.

7.3 DISCUSSION

The comparison between the predicted and measured results in several cases shows that the model developed usually gives true thermal results at the end of the welding cycle, when the weld reaches its nominal size. However, it turns out that the thermal history at the beginning of the process is not as well modelled: obviously, the temperatures predicted in the first half of the welding process are lower than the temperatures actually reached experimentally. Both thermal history experiencing in electrode, and the nugget size development validation can support this discussion.

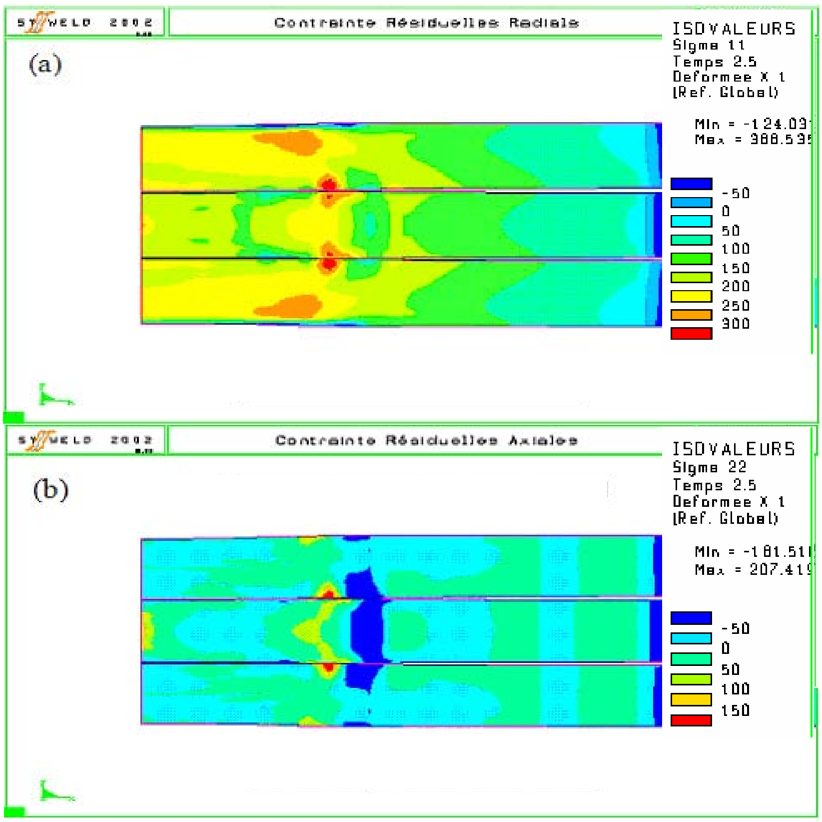

Fig. 18: Predicted stresses in weld assembly in the case of three-sheet joining at 20 cycles after the end of holding; (a) radial stress (σ_{11}), (b) axial stress(σ_{22})

Considering the parametric study in previous sections, one can figure out which input data of the model could be adapted in order to reduce the discrepancy between the model and the experimental results. It is evident that the variation of enthalpy, bulk thermal or electrical conductivity has a significant impact on the weld geometry, but these inputs are relatively well known and documented in the open material property sources. The adaptation of these properties to move the model toward the experience cannot be physically justified. And as a result, the temperatures and nugget size would also be changed at the end of welding if these adapted properties were introduced to the model. A better idea is probably to consider the electric and thermal contact resistances, since their values are much less well known, and the effect of their variation is actually concentrated at the beginning of the process, as shown in Fig. 13. A measurement campaign of these contact resistances will be further launched to check the relevant contact characteristic data used in the model.

The mechanical parameters may play a role on the thermal results. Among them, the contact condition and the high temperature behaviour of the steel material are promising parameters, since they are not well known and they may influence greatly the electro-thermal contact size variation, which is of great importance at the beginning of the process.

8. RESULTS OF THERMAL-MECHANICAL MODELLING

One of the important features of the electrical-thermal and thermal-mechanical coupling models is the residual stress distribution in the weld. The electrode indentation and the assembly deformation, the radial and axial stresses for the case of three sheets joining shown in Fig. 18 are the predicted results obtained at 20 cycles after the end of holding. Stress concentrations can be seen around the notch edges of the nugget. In the case of two-sheet joining with flat face electrode[18], it is also indicated the similar regions where the significant stress distributions are found in the assembly.

9. CONCLUDING REMARKS

A finite element analysis model with an electrical-thermal and thermal-mechanical coupling procedure was applied to study bare steel sheet joining by the RSW technique. The model provides a better understanding of the welding parameters influencing on the nugget development kinetics and the thermal characteristics in the assembly with the use of pulsed welding current schedules. The impact of the electrical-thermal material property variability on the simulated nugget is studied.

The following conclusions can be drawn from these results:

i) It is found that a decrease in one of the three dominant properties such as the thermal conductivity, the enthalpy and the bulk electrical conductivity of sheet results in the enlargement of the simulated nugget size. The estimated thermal conductivity at elevated temperature plays a role on the penetration height as well as the weld centre thermal cycles. The bulk electrical conductivity of sheet can be considered as a key input for both nugget and HAZ size variations.

The faying surface contact resistance evolution has a significant role on the nugget development, particularly at the beginning of welding. The variation in faying surface contact resistance at elevated temperature shows an insignificant impact on the nugget dimension at the latter stages of welding. This conclusion can be supported by the comparison of nugget geometry at the end of each pulse. The influence of electrode-to-sheet contact resistance shows a similar trend to that of faying surface contact resistance on the nugget development.

The extrapolation techniques used for the thermal property evaluation at elevated temperature have an impact on weld modelling. However, it is demonstrated from the present study that the validation of both temperature measurement and the weld geometry will help assuring in the degree of the confidence in the simulation results.

ii) The validation of nugget formation kinetics is carried out for the cases of two-sheet as well as three-sheet joining. The results show a quantitative agreement for the final nugget size at the end of welding in case of two-sheet joining. The discrepancy can be observed at the early stages of welding. This may be due to the electrical contact data uncertainty at low pressure and temperature. The comparison between the predicted and the measured thermal history is in a good accordance for the magnitude of temperature. Only a slight discrepancy in the heating and cooling rates was observed.

ACKNOWLEDGEMENTS

The authors would like to express their grateful acknowledgement to Messieurs G. RIGAUT, and J. CLAEYS, the director of the Metallurgical Development and Research Center and the head of resistance welding section, respectively, for their input during the paper preparation. Thanks also to J.P. DOUILLY, who performed all spot weld experiments in this study. The authors wish to thank C. DJENKAL and D. MALEWICZ for their educative advice during metallurgical preparation and investigation. The partial financial support of Association Nationale pour la Recherche et la Technologie (CIFRE educational program) is gratefully acknowledged.

REFERENCES

[1] J.A. KHAN, L. XU and Y.J. CHAO: "Prediction of Nugget Development during Resistance Spot Welding using Coupled Thermal-Electrical-Mechanical Model", *Science and Technology of Welding and Joining*, 1999, **4**, 201-207.

[2] X. SUN and P. DONG: "Analysis of Aluminum Resistance Spot Welding Processes using Coupled Finite Element Procedures", *Welding Research Supplement*, August 2000, 215s-221s.

[3] C. SRIKUNWONG, T. DUPUY and Y. BIENVENU: "Numerical Simulation of Resistance Spot Welding Process using FEA Technique", *Proceedings of 13th International Conference on Computer Technology in Welding*, T.A. Siewert, ed., June 2003, Orlando, FL.

[4] P. DONG, M.V. LI and M. KIMCHI: "Finite Element Analysis of Electrode Wear Mechanisms: Face Extrusion and Pitting Effects" , *Science and Technology of Welding and Joining*, 1998, **3**, 59-64.

[5] K. MUNDRA, T. DEBROY, T. ZACHARIA and S.A. DAVID: "Role of Thermophysical Properties in Weld Pool Modelling", *Welding Journal*, 1992, **71**, 313s-320s.

[6] W. SUDNIK, D. RADAJ and W. EROFEEW: "Validation of Computerised Simulation of Welding Processes", *Mathematic Modelling of Weld Phenomena IV*, H. Cerjak and H.K.D.H. Bhadeshia, eds., The Institute of Materials London, 1998, 477-493.

[7] M. BOBADILLA, M. NIEDERLEANDER, C. NUSS, G. PERRIN and J. SELARIES: "Données Thermiques pour Différentes Familles d'Acier", *Rapport Interne IRSID*, Groupe Arcelor, June 1994.

[8] E. THIEBLEMONT: "Modélisation du Soudage par Points", PhD. thesis, L'Institut National Polytechnique de Lorraine, 1992.

[9] "Caractérisation de la Soudabilité par Résistance par Points de Produits Plats Revêtus ou Non", *Normalisation Française A87-001*, ISO No. 18278/2.

[10] H. MURAKAWA, F. KIMURA and Y. UEDA: "Weldability Analysis of Spot Welding on Aluminium using FEM", *Mathematic Modelling of Weld Phenomena III*, H. Cerjak and H.K.D.H. Bhadeshia, eds., The Institute of Materials London, 1997, 944-966.

[11] A. FONTES, I. TOSELLO, F. CHARDEL and N. KERROUAULT: "High Thermal Field during Arc Remelting as Input for Hot Cracking Characteristic", *Mathematic Modelling of Weld Phenomena V*, H. Cerjak and H.K.D.H. Bhadeshia, eds., The Institute of Materials London, 2001, 807-834.

[12] Z. FENG, W. CHENG, and Y. CHEN: "Development of New Modelling Procedures for 3D Welding Residual Stress and Distortion Assessment", *Summary Report SR9818*, Cooperative Research Program EWI, November 1998.

[13] M. VOGLER: "Investigation of Resistance Spot Welding Formation", PhD. thesis, Stanford University, December 1992.

[14] W.V. ALCINI: "Experimental Measurement of Liquid Nugget Heat Convection in Spot Welding", *Welding Journal*, May 1990, 177s-180s.

[15] M. VOGLER and S. SHEPPARD: "Electrical Contact Resistance under High Loads and Elevated Temperatures", *Welding Research Supplement*, June 1993, 231s-238s.

[16] S.S. BABU, M.L. SANTELLA, Z. FENG, B.W. RIEMER and J.W. COHON: “Empirical Model of Effects of Pressure and Temperature on Electrical Contact Resistance of Metals”, *Science and Technology of Welding and Joining,* 2001, **6**, 126-132.
[17] G. LE MEUR: “Etude de la Condition de Liaison Thermique à une Interface de Contact Solide-Solide Siège d’une Dissipation par Effet Joule : Application au Soudage par Points”, PhD. thesis, Ecole Polytechnique de l’Université de Nantes, 2002.
[18] H.F. HENRYSSON, F. ABDULWAHAB, B.L. JOSEFSON and M. FERMER: “Residual Stresses in Resistance Spot Welds: Finite Element Simulations, X-Ray Measurements and Influence of Fatigue Behaviour”, *IIW Document*, *IIW-X/XV-RSDP-21-98.*

Influence of Heat Transfer Coefficient of the Contact :

It is believed that the heat transfer coefficient-(HTC) of the contact is a function of temperature,-[Le MUR02]. In our case, HTC of the contact is evaluated from empirical formula-[THI92] and it increases with temperature. Khan *et al.*,-[KHA99], assumed that HTC may be approximated as a constant value for all temperatures in their work for aluminium sheet joining simulation. The variability of HTC is between -1000% and +400%.

However, the HTC depends also on the sheet coating condition with the comparison between HTC of non-coated sheet and that coated sheet,-[Le MUR02]. It is found that HTC determination by using an inversed numerical method is not an easy task, particularly in the case of coated sheet joining. Recently, there is still no available measured HTC data for coated sheet joining in the literature.

The formulation of electro-thermal model used in our analysis can be found in the literature,-[ROB02]. Recently, the influence of interface power dissipated factor with the new contact model formulation is presented by Feulvarch, -[FEUL04], (see §Eqn. 3.17 for the definition of the proportion of power dissipated at the interface, ‘ f^{Si} ’). Basically for the same material in contact, e.g. at the sheet/sheet interface, term effusivity, ‘ $b = \sqrt{K\rho Cp}$ ’ should be equalled and the power partition, ‘ f^{Si} ’, can be defined to ‘0,5’. This suggests that the same amount of heat generated at the interface will transfer to both solid bodies.

However, this is not the case for the heat partition at the electrode/sheet interface. For different metallic material in contact, the heat effusivity is complicated associated with the temperature dependence of materials. Feulvarch proposed a constant value of effusivity, which is ‘75%’ of the heat generation evacuated by the electrode, and ‘25%’ of the heat is transferred to the sheet.

The heat transfer coefficient (HTC) for the perfect contact condition, (case $h < \varepsilon$), reveals the heat transfer coefficient as a temperature dependent function. To understand the influence of HTC, the variability of ‘ $\pm 5\%$ ’, and ‘ $\pm 20\%$ ’ are considered in the study. HTC of the electrode/sheet interface is extrapolated linearly for elevated temperature. It is noted that maximum temperature found experimentally near the electrode face is 700-750°C, [DUP98], in the case of joining coated sheet. In similar manner for faying surface HTC evaluation at elevated temperature, HTC is extrapolated linearly after the fusion temperature of steel.

The results for weld geometry development with ‘ $\pm 5\%$ ’ variability of HTC of electrode/sheet interface are presented in Fig. 3.12. It is found that there is no significant difference in terms of nugget and HAZ comparisons. Only slight difference can be observed at the beginning of welding.

Similar study for ‘ $\pm 5\%$ ’ and ‘ $\pm 20\%$ ’ variability of HTC of sheet/sheet interface are conducted and presented in Figs. 3.13-14. It is found from the weld geometry comparison that HTC at sheet/sheet interface used in the model has no influence on both nugget and HAZ sizes.

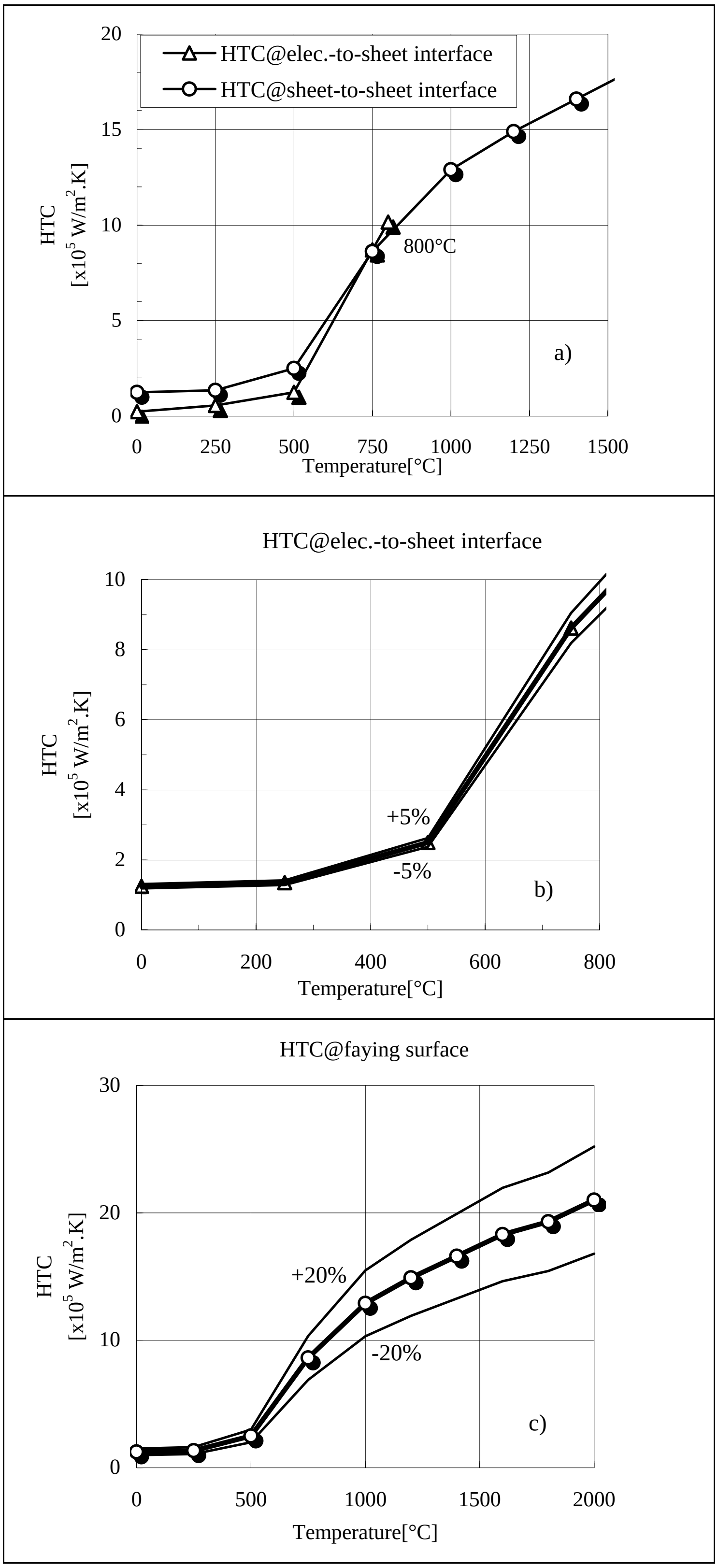

Fig. 3.11: *Variability of interface transfer coefficients as a temperature-dependent function, a) Comparison between HTC of faying surfce and that of electrode-to-sheet interface, b) ±5% variability for heat transfer coefficients of the electrode-to-sheet using a linear extrapolation function, and c) ±20% variability for heat transfer coefficients of the faying surface using a linear extrapolation for value at elevated temperature, (Note that* T_{max} *at the faying surface is 1700/1800°C, and that of electrode-to-sheet is around 700/750°C.* $T_{F,Cu}$*=1085°C)*

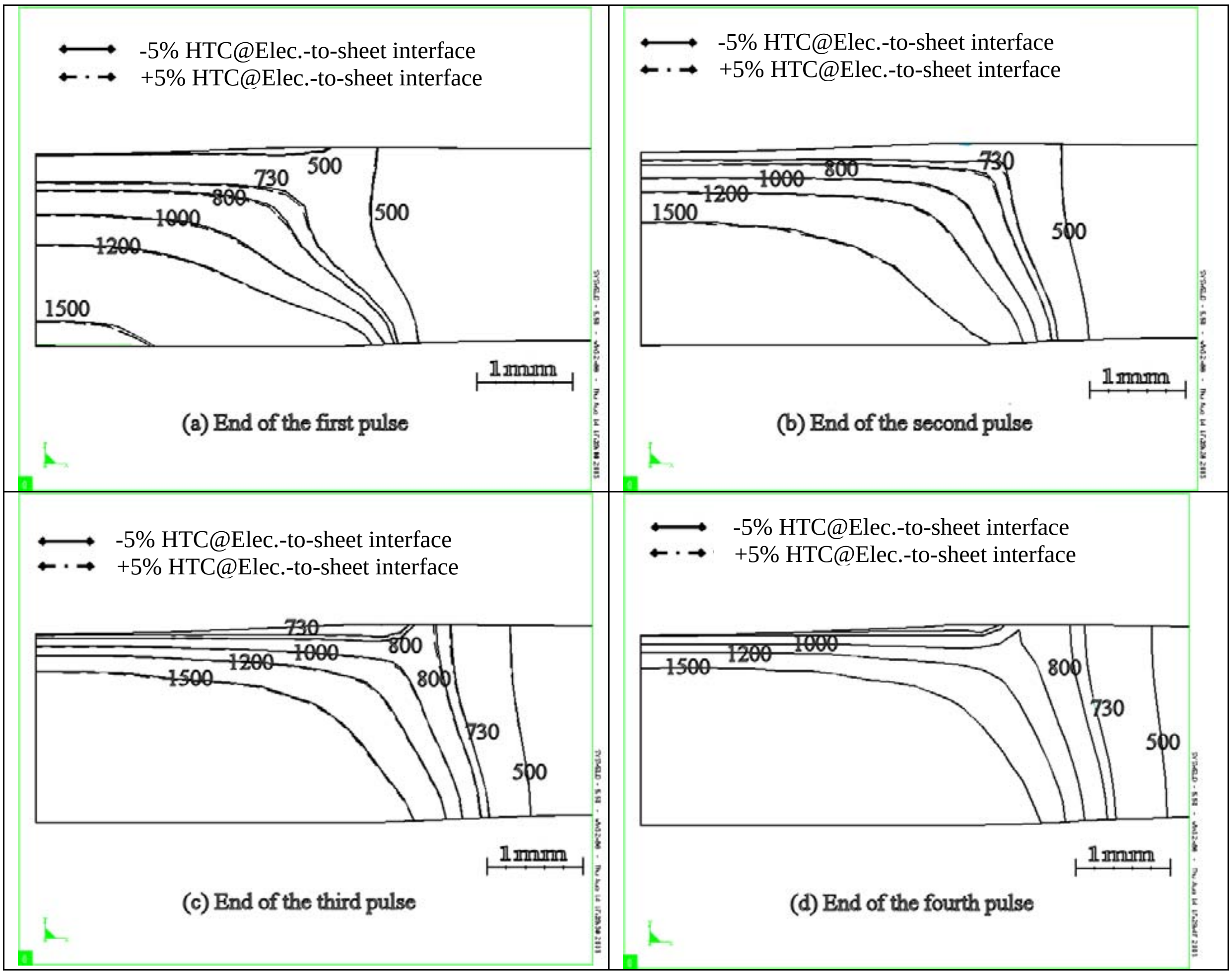

***Fig. 3.12**: Influence of ±5% variability of heat transfer coefficient of electrode/sheet interface on weld geometry development, a) at the end of the first pulse, b) at the end of the second pulse, c) at the end of the third pulse, and d) at the end of welding*

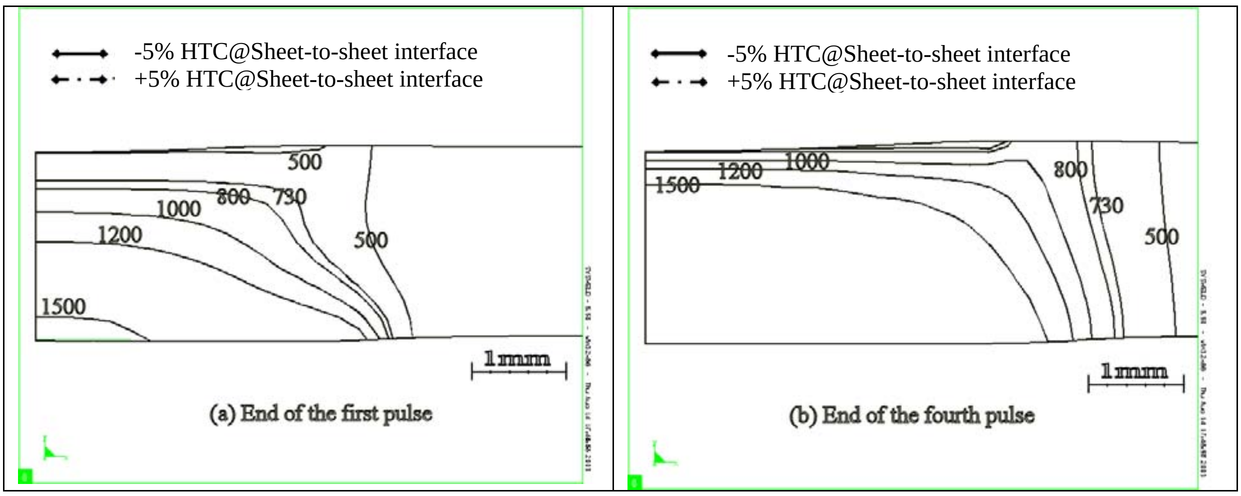

***Fig. 3.13:** Weld geometry development comparison with ±5% variability of heat transfer coefficient at sheet/sheet interface on weld geometry development, a) at the end of the first pulse, and b) at the end of welding*

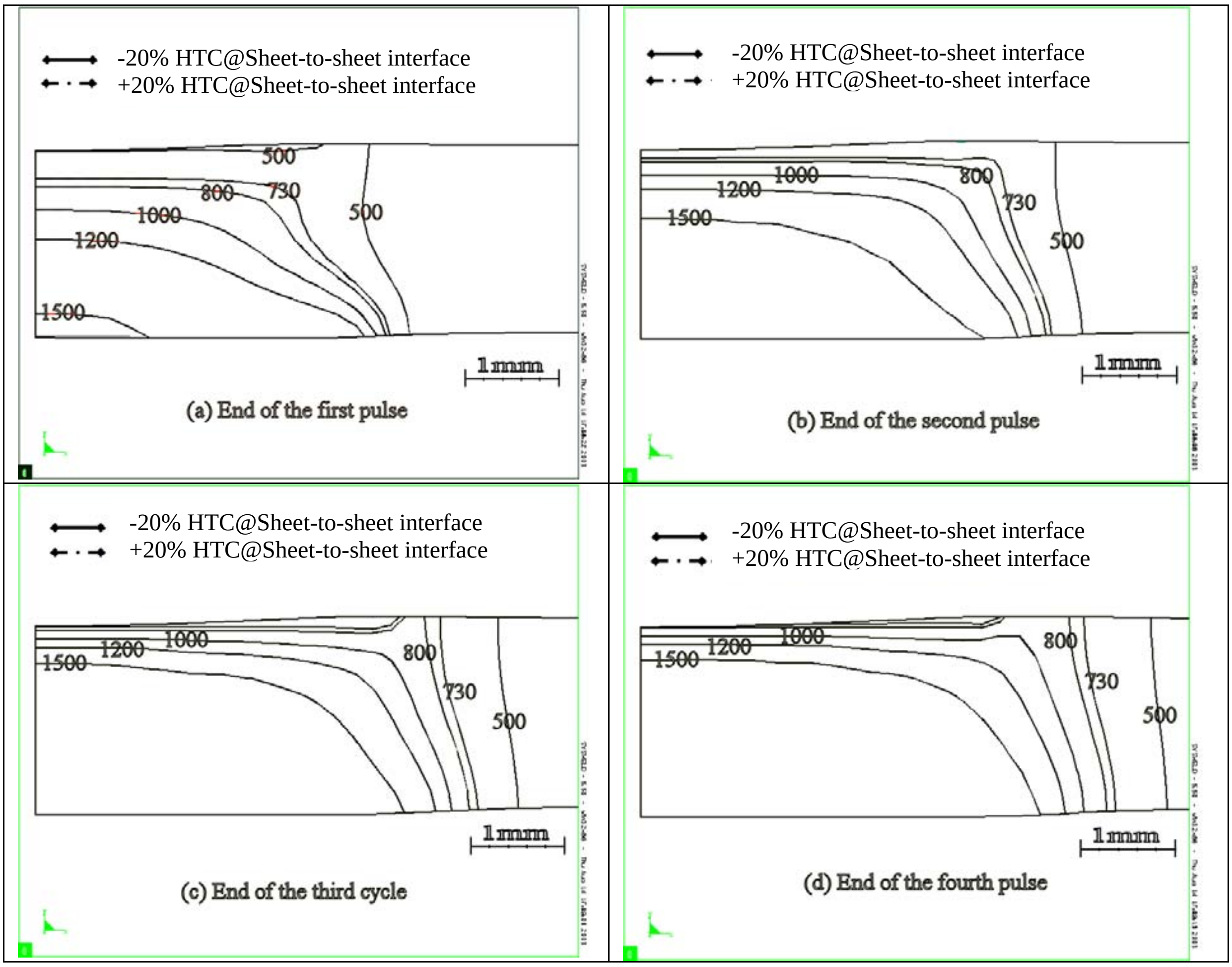

Fig. 3.14: Weld geometry development comparison considering ±20% variability of heat transfer coefficient at sheet/sheet interface on weld geometry development, a) at the end of the first pulse, b) at the end of the second pulse, c) at the end of the third pulse, and d) at the end of welding

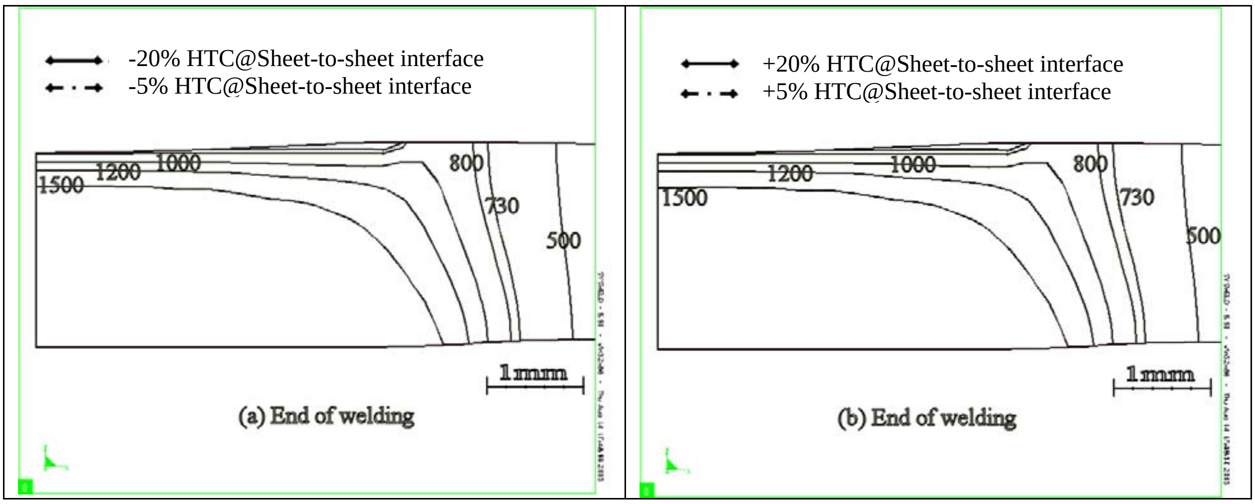

Fig. 3.15*: Final weld geometry comparison for a similar tendency of sheet-to-sheet interface HTC, a) representative final weld geometry comparison between −20% and −5% variability of HTC of sheet-to-sheet interface, and b) Final weld geometry comparison between +20% and +5% variability of HTC of sheet-to-sheet interface*

To verify these results, the comparison between ‘ ±5% ’ and ‘ ±20% ’ variability of HTC is illustrated in Fig. 3.15. The results show no difference for every stage of welding.

The intermediated conclusion can be drawn from these results regarding the degree variability of ‘ ±20% ’ that *HTC at sheet-to-sheet interface has no influence for the weld geometry development and HTC at electrode-to-sheet interface has an only slight influence on weld geometry*, *especially at beginning of welding.* It is also possible to increase the degree of variability as conducted in the literature, [KHA99], for the influence of HTC of contact on thermal history and weld geometry development.

<u>Influence of Interface Threshold Values</u> :

Concerning the electro-thermal contact formulation described in Eqns. 3.9 and 3.10, another significant parameter of this model formulation is a permissible threshold value described for the perfect and non-perfect contact condition. A simple model was constructed to study the influence of this value between two surfaces for the current flux flow in previous paragraph.

After updating the workpiece deformation by the coupled calculation, the electro-thermal module takes into account the separating distance between two sheets and electrode and sheet for next step of electro-thermal computation.

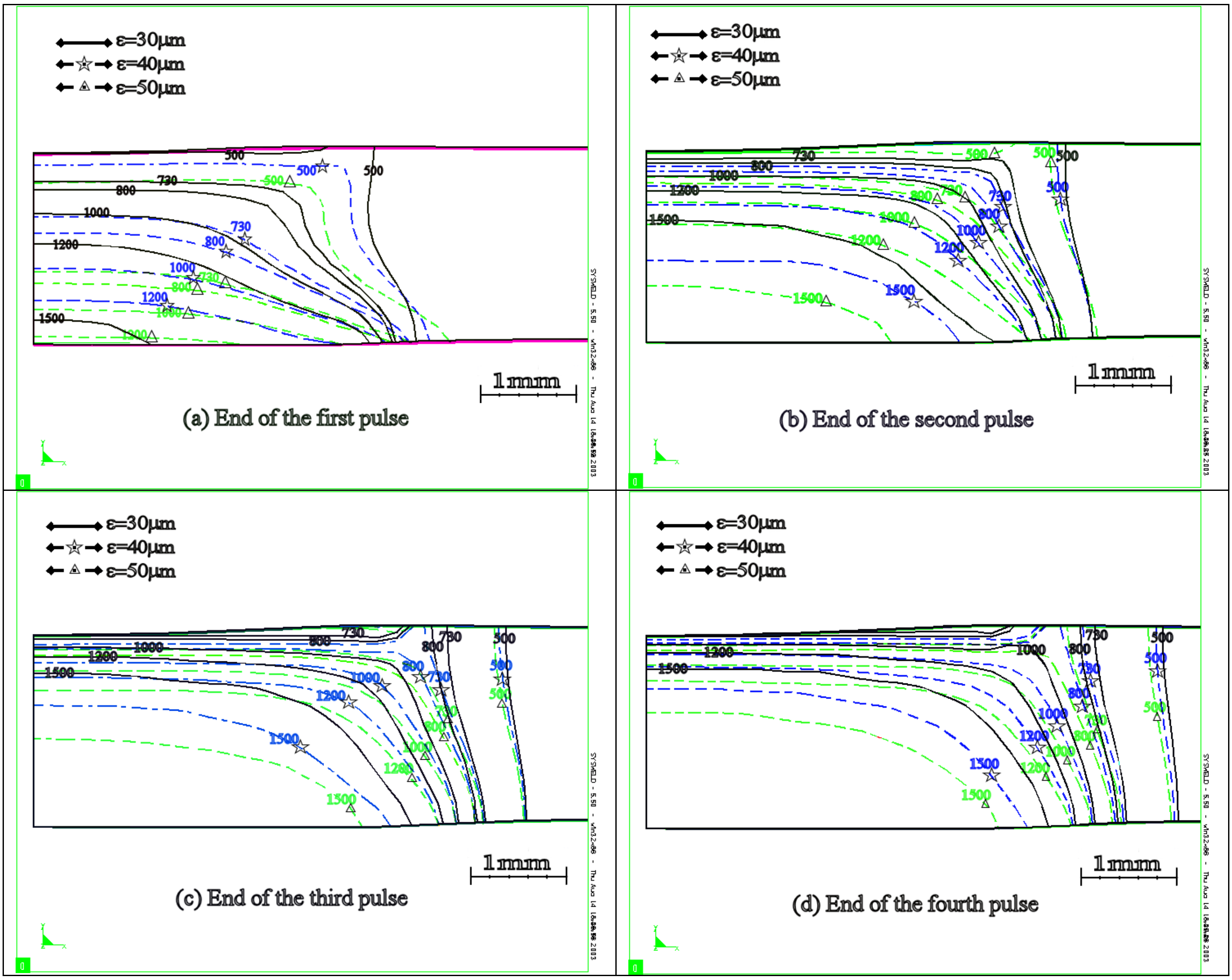

Fig. 3.16*: Final weld geometry comparison corresponding to three possible values of epsilons defined for a permissible current passage, a) at the end of the firth pulse, b) at the end of the second pulse, b) at the end of the third pulse, d) at the end of welding*

In this study, the minimum threshold value is numerically found to be 30 micrometers regarding the possibility to reach the calculation convergence. Actually for the non-coated sheet joining, this value should be kept to the lowest possible value. Prior to using this threshold value, a relative low threshold value of 5 micrometers was tested, but no numerical convergence can be reached, even with both time-step or convergent criterion. This is mainly due to the strong concentration of the current flux, and thus a high temperature gradient at the interface.

The influence of three threshold values at the faying surfaces, which ranges 50, 40, and 30 micrometers are studied. The electrode/sheet interface threshold value is kept constant to 30 micrometers in all cases. The comparison for weld geometry with different threshold values is illustrated in Fig. 3.16. The results reveal a significant influence of the threshold value on the weld geometry.

The conclusion of this section can be summarized that *the larger the threshold value, the smaller the weld size*. These results are clearly observed by a comparison during welding stage. The largest nugget can be obtained in the case of the minimum threshold value of 30 micrometers at the sheet/sheet interface.

In the case of joining non-coated sheet, this permissible value has to be kept as low as possible in order to obtain a good validation with the experiment. However in the case of joining coated sheet, the adaptation of this value may be useful. Because there is the presence of the fused zinc at the periphery of both interfaces, thus the enlargement of both electrical and thermal contact sizes.

Weld Geometry Validation in Lower Domain of Weldability :

The validation of weld geometry is presented in this section for the lower domain of weldability as shown in Fig. 3.17. The validation is conducted only for the end of welding, because there is no weld formation observed during the earlier welding cycles.

Smaller predicted nugget and HAZ size compared with experiment is observed. The nugget diameters are 5.35 and 6.58-mm. resulting from simulation and experiment, respectively. The discrepancy in nugget diameter validation is around 18%. Similarly to the nugget validation, the predicted HAZ size and geometry is relatively smaller than that of experience.

It can be concluded that *a relationship between electrical contact resistance and temperature is not sufficient to obtain the satisfactory validation in the lower and upper domains of weldability*. Because the numerical result shows only a good agreement with that of experiment for the final nugget and HAZ size at the upper limit of weldability lobe, but it is relatively poor for the weld prediction at the lower limit. Bearing in mind that the same material database, electrical contact resistance, and contact permissible values are retained in all cases of the simulation. Using an electrical contact resistance as a function of temperature cannot provide a satisfactory validated results.

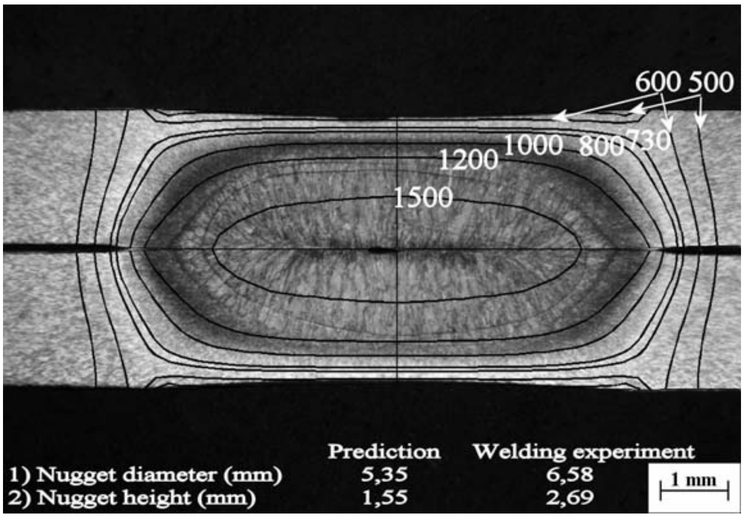

Fig. 3.17: *Final weld geometry validation at the lower domain of weldability (Welding condition: 400daN-8,4kA/4(6+2)-TH8: AKDQ@2mm-thick non-coated sheet)*

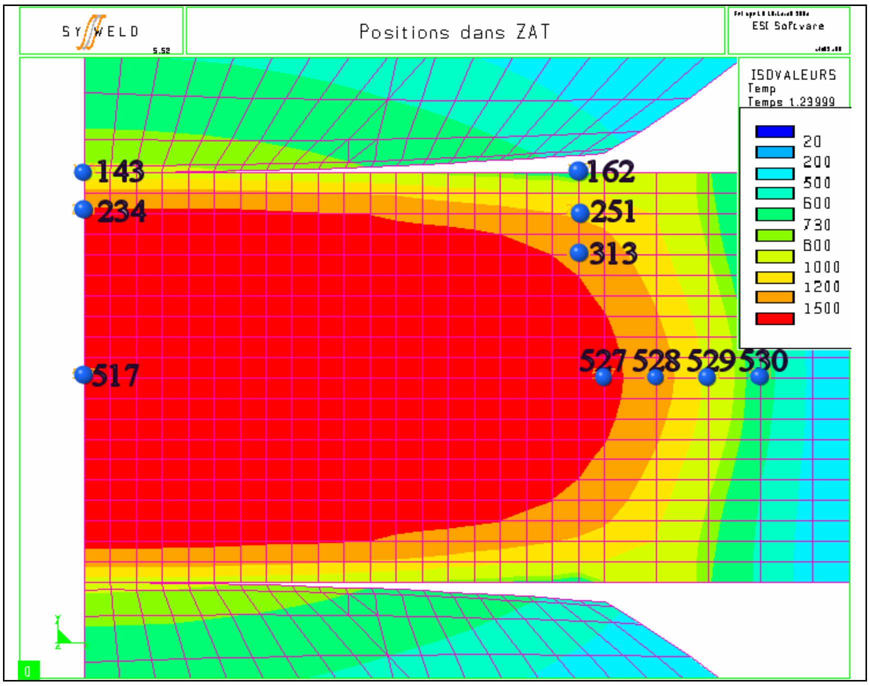

Fig. 3.18: *Different positions in the HAZ and weld regions considered for the heating and cooling rates; (Nomenclature of the node is displayed in the figure)*

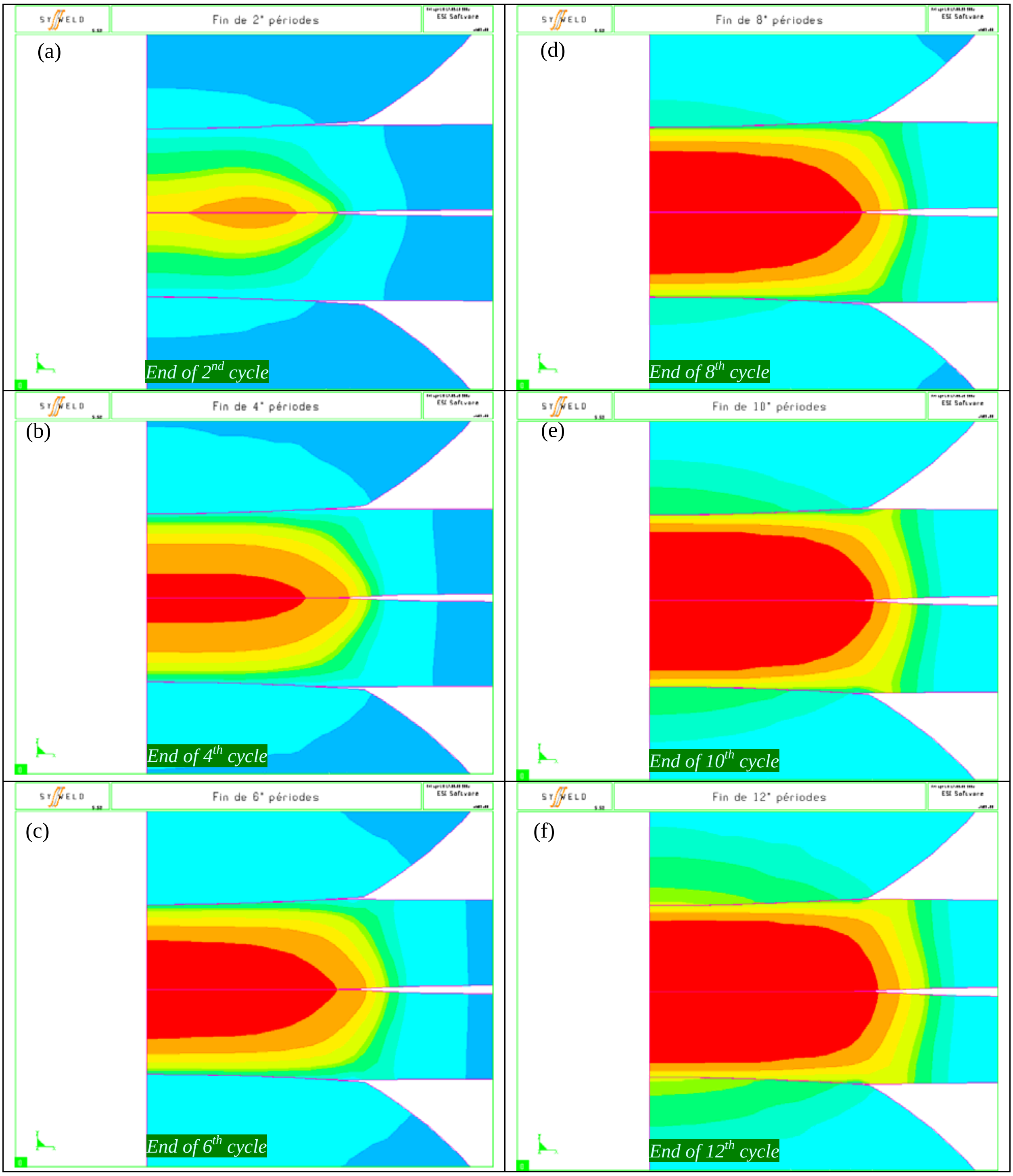

***Fig. 3.19 :** Weld morphology development at the end of each two pulses during welding; a) at the end of second cycle, b) at the end of fourth cycle, c) at the end of sixth cycle, d) at the end of eight cycle, and d) End of welding*

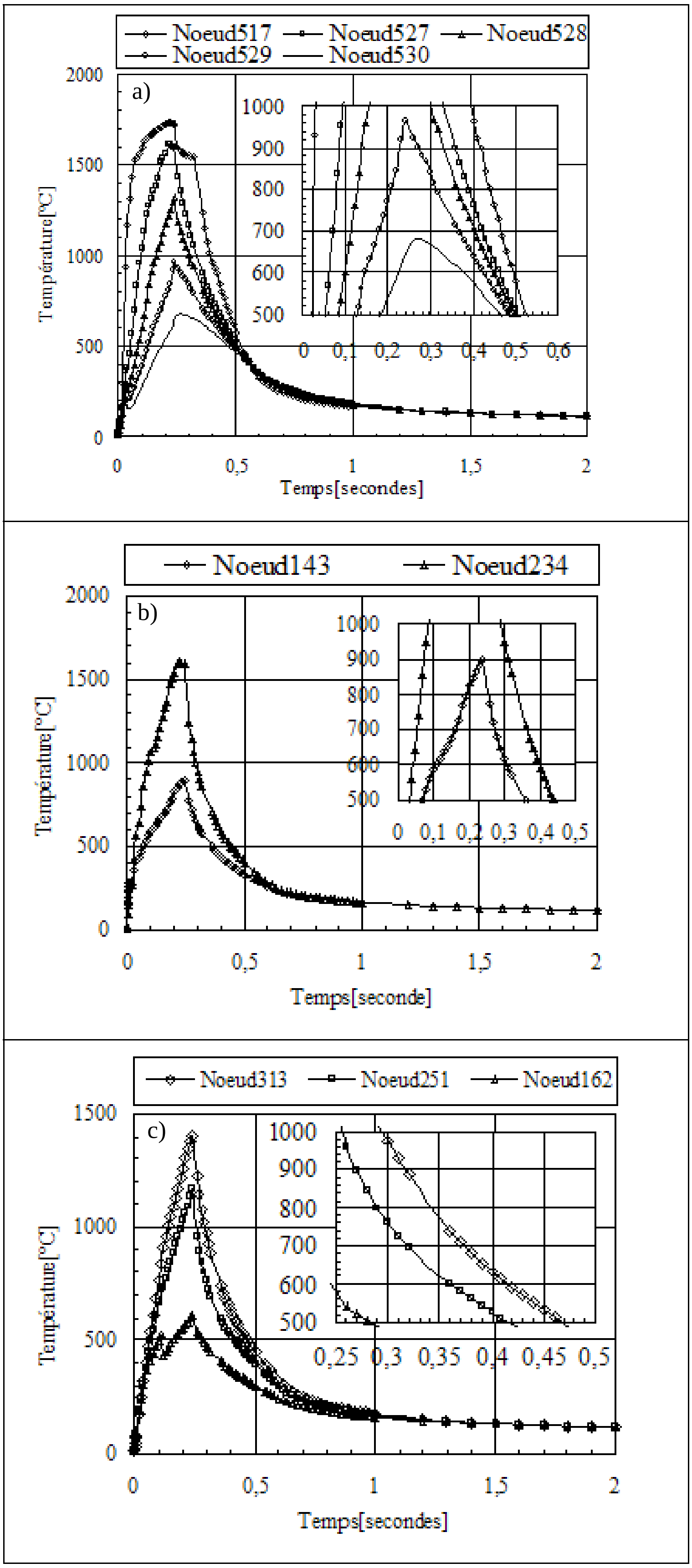

Fig. 3.20: *Nodal heating and cooling rates at different points in the HAZ and weld regions; (Node labels are displayed in the figure, a) Nodal thermal history in radial direction in the weld and HAZ regions, b) Nodal thermal history in the axial direction, and c) Nodal thermal history in the HAZ region*

Heating and cooling rates at the weld center;

Table 3.2.1: Weld center; Node 517@(x=0,y=0)

Time (seconds)	Heating rate (°C/s) / Tmax(°C)
0-0,08	*22879 (At the beginning of welding)*
0,08-0,24	*5935 (At point where slope changes, @0,08sec)*
0,002-0,24	*7039 (Mean value) / 1722°C*
Time (s)	Cooling rate from 800 to 500°C (°C/s)
0,44-0,50	*-3731*

Heating and cooling rates in the radial direction;

Table 3.2.2: Node527@(x=3,y=0)

Time (s)	Heating rate (°C/s) / Tmax (°C)
0-0,24	*7489 / 1601°C*
Time (s)	Cooling rate from 800 to 500°C (°C/s)
0,39-0,50	*-2567*

Table 3.2.3: Node528@(x=3.3, y=0)

Time (s)	Heating rate (°C/s) / Tmax (°C)
0-0,24	*5732 / 1328°C*
Time (s)	Cooling rate from 800 to 500°C (°C/s)
0,37-0,50	*-2158*

Table 3.2.4: Node529@(x=3.6, y=0)

Time (s)	Heating rate (°C/s) / Tmax (°C)
0-0,24	*3764 / 963°C*
Time (s)	Cooling rate from 800 to 500°C (°C/s)
0,32-0,49	*-1702*

Table 3.2.5: Node530@(x=3.9, y=0)

Time (s)	Heating rate (°C/s) / Tmax (°C)
0-0,24	*2532 / 679°C*
Time (s)	Cooling rate from Tmax to 500°C (°C/s)
0,24-0,46	*-820*

Heating and cooling rates in the axial direction;

Table 3.2.6: Node234@(x=0,y=0,96)

Time (s)	Heating rate (°C/s) / Tmax (°C)
0-0,24	*6837 / 1593°C*

Time (s)	Cooling rate from 800 to 500°C (°C/s)
0,36-0,44	*-2604*

Table 3.2.7: Node143@(x=0, y=1,20)

Time (s)	Heating rate (°C/s) / Tmax (°C)
0-0,24	*3030 / 897°C*

Time (s)	Cooling rate from 800 to 500°C (°C/s)
0,26-0,36	*-3200*

Heating and cooling rates in the HAZ;

Table 3.2.8: Node313@(x=2.85, y=0.72)

Time (s)	Heating rate (°C/s) / Tmax (°C)
0-0,24	*6112 / 1406°C*

Time (s)	Cooling rate from 800 to 500°C (°C/s)
0,36-0,46	*-2211*

Table 3.2.9: Node251@(x=2.85, y=0.96)

Time (s)	Heating rate (°C/s) / Tmax (°C)
0-0,24	*4861 / 1168°C*

Time (s)	Cooling rate from 800 to 500°C (°C/s)
0,29-0,41	*-2357*

Table 3.2.10: Node162@(x=2.85, y=1,20)

Time (s)	Heating rate (°C/s) / Tmax (°C)
0-0,24	*2295 / 614°C*

Time (s)	Cooling rate from Tmax to 500°C (°C/s)
0,24-0,28	*-2770*

Heating and Cooling Rates Experiencing in Weld :

The study of the heating and cooling rates of the assembly of AKDQ 1.2-mm thick steel sheet joining is in collaboration with the Université de Valenciennes. The predicted heating and cooling rates can be further used for the HAZ microstructure simulation Welding schedules used is given in Table 3.1 and the nodes, where the thermal history are observed, is shown in Fig. 3.18.

Table 3.1: Welding schedule used for welding operation

Electrode	TH6
Squeezing (Force /Cycles)	300daN/50
Welding (Current/Cycles)	9,2kA/12
Maintaining (Force /Cycles)	300daN/12

The simulated weld morphology development can be seen in Fig. 3.19. Thermal history evolution of the process is presented in Fig.3.20.

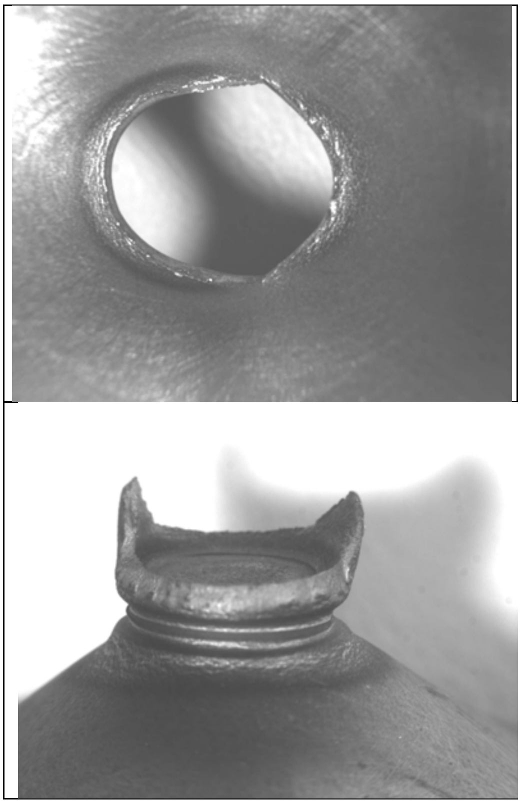

Fig. 3.21: *Typical failure of a cross-tensile specimen of low carbon AKDQ steel. This case is typical perfect failure of the weld plug promoting the maximum tensile strength than other types of weld plug rupture. (See also [FER98-2] for the definition of rupture types and examples of related maximum tensile strength)*

To determine the heating and cooling rates of local points in the weld, the selected nodal thermal history, (§Fig. 3.20) is presented. Nodal thermal characteristics show a similar response to single pulse of current. Maximum heating rate observed at the center of the weld is 23000°C/s during the first four cycles or 0.08 seconds, and the heating rate is decreased for the latter cycles, which is 6000°C/s for this stage. The mean heating rate for welding process is around 7000°C/s. However the advanced thermo-mechanical simulator, namely Gleeble®3500, can perform the simulation with the maximum heating rate of 10000°C/s, therefore such very high heating rate at the beginning of welding is beyond the limit of the machine performance and it is may be not necessary to simulate the microstructures of this steel with such conditions. Key issues in the residual microstructure simulation should be concentrated on the characteristic of the HAZ rather than in the nugget region.

The heating rates of several points located in the radial direction and in the HAZ region are detailed and given in Tables 3.2.1-5. Heating rates ranging from 2500 to 7500°C/s are observed in this zone. For the heating rates of the positions located in the HAZ and in the axial direction shown in Tables 3.2.6-7, the heating rates found are 6800 and 3000°C/s.

For the rupture of a full plug, (§Fig. 3.21), the rupture occurs mostly in the HAZ. To simulate the properties of this zone, the determination of the heating and cooling rates of these regions are important indicating as the nodes 313, 251, and 162, (§Fig. 3.18). The heating rates found are between 2300 and 6100°C/s. and the local cooling rates are 2770, 2360, and 2210°C/s for nodes 313, 251, and 162, respectively. However for low carbon steel, the effect of heating rate on the transformation temperatures, $AC_1$and AC_3, may be less significant than other higher carbon steel grades. It is reported in the literature as in case of mild steel, [FEU54], that the influence of heating rate on transformation temperatures is more significant with the increase of carbon in steel: *The higher the heating rates, the higher the transformation temperatures,* AC_1, and AC_3.

Features for low alloy carbon steel simulation are the local maximum temperatures and the cooling rates from 800 to 500°C. It is noted that numerical results can provide an approximation of the heating and cooling rates for microstructure simulation. However, it may be useful to compare grain sizes and residual transformed phases in the specimen and those of weld microstructures. This is to assure the results obtained from the simulation or for an adaptation of the cooling rates or other simulation parameters in the case of microstructure comparison discrepancy.

Influence of Maintaining Time Length :

Electrode-hold time has an influence on the microstructure and strength of the weld. Optimized electrode-hold time is one of the practical weld quality amelioration techniques used for high strength steel joining, [PET02]. The modeling in this section can be useful for ongoing research and for the study the influence of the cooling rates on the residual stress distribution and microstructures. The influence of such modification is studied using Abaqus® code and reported by Li *et al.*, [LI97-3]. The welding standard normally recommends that the holding time should be equaled to that of welding time in order to promote the sufficient time for the weld solidification.

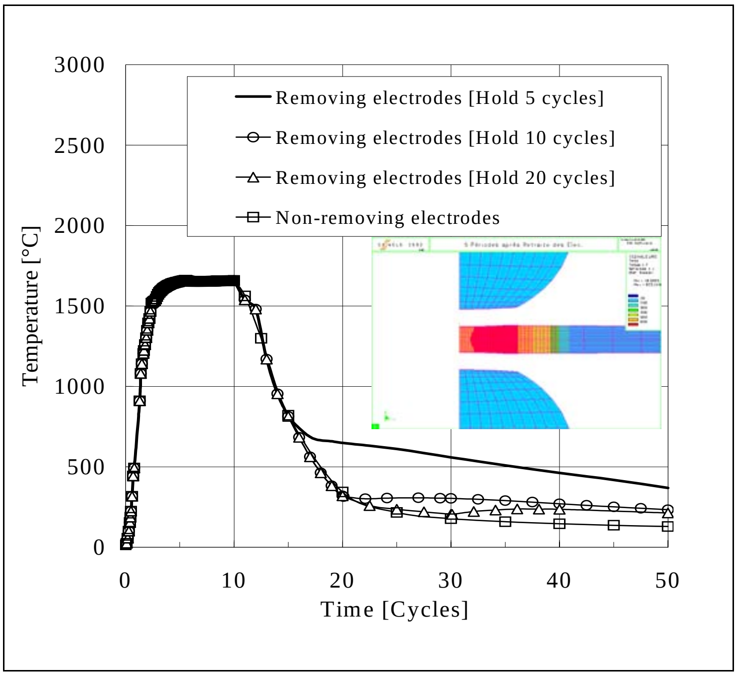

Fig. 3.22*: Influence of the electrode-hold time length on the thermal history of weld center.*

To perform the calculation without the electrode-holding, two stages of the coupling sequences are implemented. The first coupling computation is undertaken automatically until the end of holding. The second coupling procedure is programmed for the electrode removing. The boundary conditions are shown in Fig. 3.7.

The comparison between different hold time lengths shown in Fig. 3.22 reveals that the shorter the electrode-hold time, the slower the cooling rate at the nugget center. The heat dissipation after electrode removing is illustrated in Fig. 3.23a-c.

Simulated stresses results reveals the symmetrical stress occurring in the assembly, (§Fig. 3.24). Radial and axial stress components and their maximum are shown in Figs 3.24a and b, respectively. However, the relative high radial stress is found at the faying surface, where the sticking contact condition is defined for the weld nugget after the end of welding.

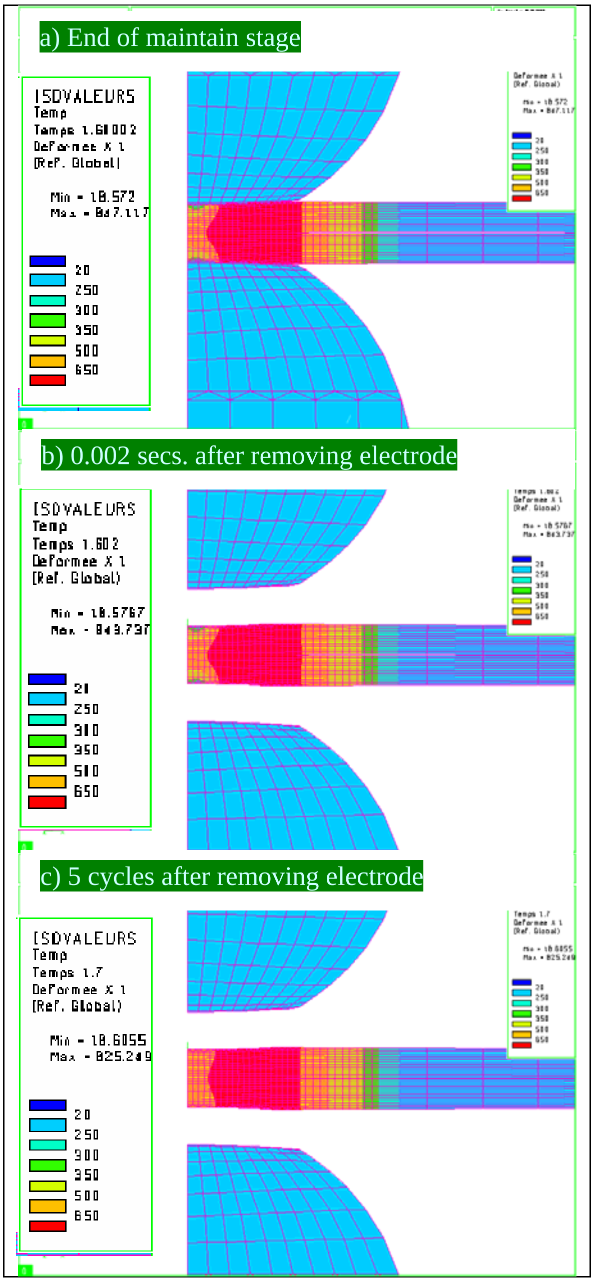

Fig. 3.23*: Simulation of heat dissipation after removing electrodes, a) End of maintain stage, b) just after removing the electrodes, c) 5 cycles after removing electrodes, (Region, where temperature is higher than 650°C, is indicated as the red zone)*

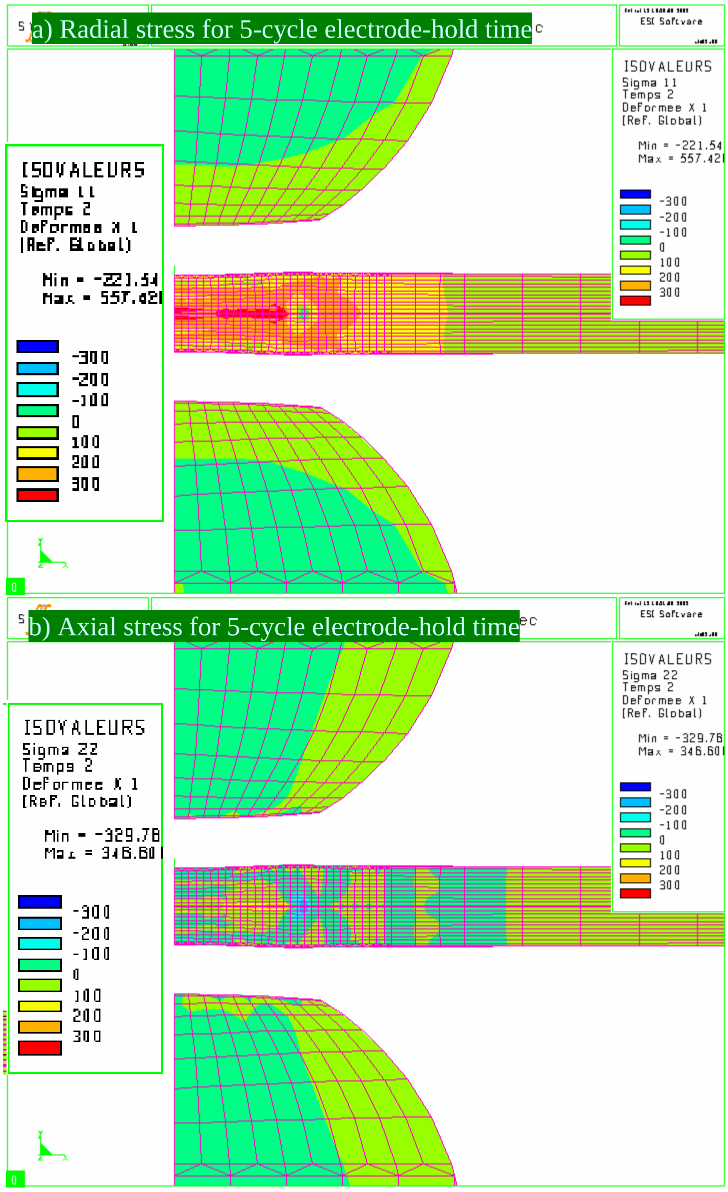

***Fig. 3.24**: Residual stresses in the assembly for electrode-hold time of 5 cycles observed at **100 cycles or 2 seconds after welding**, (a) Radial stress (' σ_{11} '), and (b) Axial stress (' σ_{22} ')*

Model Exploitation :

The exploitation of our numerical model is the thermal history, the heating and the cooling rates in the weld and in the electrode. The experimental measurement of thermal cycles by micro-thermocouple embedded in the electrodes-[Le MUR02] or in the sheets-[ANA87] can be conducted, but such elaborate measurements are time consuming and expensive for the measurement instrumentation. Quantitative measurement in RSW is complicated task due to very short time characteristic of the process and the perturbation of strong electro-magnetic fields generated on the acquisitioned signals. In addition, the welding schedule can be varied significantly from one to another set of welding parameters relating to sheet configurations, thus the difference in thermal cycles occurring in the weld.

The numerical model can be therefore considered as another useful tool to provide an insight into the process characteristics, when the parameters are changed. For instance, the exploitations of thermal history obtained from the model are as follows:

❖ Evaluation the diffusion coefficients or the Cu-alloy phases formed on the electrode face using the simulated thermal cycle, [DUP98].

❖ Comparison the amount of heat generated from Peltier effect and that produced by Joule heating effect in case of joining coated sheet, [DUP00].
❖ Evaluation the heating and cooling rates in the case of high-strength steel joining for the simulation of microstructures in the HAZ using Gleeble® machine, [SRI03-1]
❖ Optimization a secured distance between the weld and the adhesive bonding position in the case of combined weld-bonding process. This is to prevent the adhesive curing or decomposed by heat dissipated from the weld, [DUP04].

Recently, other application of the numerical model of RSW is linked to on-line monitoring and parameter control of the process, [MAT02-2]. The method includes a finite difference model incorporated the input of on-line measured voltage and current to evaluate a global electrical resistance of the assembly. The output of the model is the predicted weld size. The welding parameters may be adapted for the next or even for the ongoing weld by shortening or lengthening welding time. The calculation time of this model must be very fast to response the on-line adapted parameters. Earlier, the control device and methodology using a numerical is proposed by Tsai *et al.*, [TSA91].

3.9 Conclusions :

Numerical study of RSW process is presented with the electro-thermal/thermo-mechanical decoupling and coupling procedure. A case study of the influence of the electrode-hold time on the thermal history is presented. Temperature dependent physical properties of both sheet and electrode are included in all simulations. The conclusion can be drawn as follows:

i) According to the results of decoupling procedure for joining sheet with flat face electrode, it is disclosed that faying surface contact size governs not only thermal distribution, but also weld sizes. It is possible to fix the contact size at the faying surface to obtain a good validation of the final nugget size. In the case of stackup sheet joining, e.g. joining three dissimilar sheets with different thickness, the optimization of the contact size becomes complicated and not evident with the use of decoupling procedure.

ii) Numerical study for the influence of post-heat treatment is studied in the case of the TRIP steel joining. The thermal history associated with the use of post heat treatment and the influence of this process on the HAZ thermal behaviors are presented. It is disclosed that the appropriate selection of both magnitude and number of cycles of post heat treatment has an impact only on the HAZ thermal behaviors, thus on the microstructure quality. On the other hand, the application of post-heat treatment shows no influence on the weld nugget size and geometry.

iii) A comprehensive study on the impact of thermo-physical property variability is reported in comparing the weld nugget development. Based on the enthalpy thermal model, it is found that the sheet thermal conductivity, enthalpy, and bulk electrical conductivity show a dominant role on the final nugget size. Decreasing any one of three properties will result in the enlargement of the nugget and the HAZ sizes.

The electrical contact resistance has an impact on weld geometry development, particularly at the beginning of welding. The electrical resistance shows a slight influence on the final weld size.

In the case of the relatively slight variability of the HTC, the heat transfer coefficient of the contact has no influence on the weld geometry. However the lack of measured HTC, it is not easy to clarify the influence of this input parameter on the model.

Basing on the electrothermal contact model of Sysweld™ code, the threshold value of model has been tested using a simple electrothermal model and further introduced to RSW model. It is found that threshold value has a strong influence on weld geometry development at all stages, not only in the beginning of welding as observed in the case of the influence of electrical contact resistance.

For the non-coating sheet, this value should be kept as the lowest possible in order to obtain a good validation of weld size. The permissible value used in all models is in order of 30 micrometers. However in the case of joining coated sheet, the fused zinc appearing at the periphery of the interface cannot be modeled. Threshold value could be used modeling or taking into account the contact size enlargement in the case of coated sheet joining simulation.

iv) Determination of the heating and cooling rates is presented in the case of two-sheet joining of AKDQ steel. Using the upper limit welding parameters, the averaged heating rate for welding cycles is 7000°C/s. The highest heating rate is found at the weld centre. For an effective HAZ property simulation, the cooling rates or time length down from 800° to 500°C must be considered. Heating and cooling rates found from this study can used for a simulation of HAZ behaviors.

To obtain more understanding about the influence of a modified welding schedule, the influence of the electrode-hold time on the thermal history in the weld is studied by using a model with removing electrodes. It is disclosed that the shorter the electrode-hold time, the slower the cooling rate. The relationship between electrode-hold time and weld strength has to be profoundly studied. However, the electrode-hold time should be sufficiently long to maintain the weld solidification.

v) Possible sources of the discrepancy between experiment and simulation could be :

- First, the lack of appropriate electrical contact resistance values,
- or second, the numerical parameters in electro-thermal contact model formulation, such as a permissible value of the current passage at the interface, « epsilon value », (§Fig. 3.16).